THE ASTROPHYSICAL JOURNAL, 658:680–709, 2007 April 1

PHYSICAL PROPERTIES, BARYON CONTENT, AND EVOLUTION OF THE Lyα FOREST: NEW INSIGHTS FROM HIGH-RESOLUTION OBSERVATIONS AT $z \lesssim 0.4$[1]

N. LEHNER,[2] B. D. SAVAGE,[3] P. RICHTER,[4] K. R. SEMBACH,[5] T. M. TRIPP,[6] AND B. P. WAKKER[3]
Received 2006 November 17; accepted 2006 December 10

ABSTRACT

We present a study of the Lyα forest at $z \lesssim 0.4$, from which we conclude that at least 20% of the total baryons in the universe are located in the highly ionized gas traced by broad Lyα absorbers. The cool photoionized low-z intergalactic medium (IGM) probed by narrow Lyα absorbers contains about 30% of the baryons. We further find that the ratio of broad to narrow Lyα absorbers is higher at $z \lesssim 0.4$ than at $1.5 \lesssim z \lesssim 3.6$, implying that a larger fraction of the low-redshift universe is hotter and/or more kinematically disturbed. We base these conclusions on an analysis of seven QSOs observed with both *FUSE* and the *HST* STIS E140M ultraviolet echelle spectrograph. Our sample has 341 H I absorbers with a total unblocked redshift path of 2.064. The observed absorber population is complete for $\log N_{\rm H\,I} \gtrsim 13.2$, with a column density distribution $f(N_{\rm H\,I}) \propto N_{\rm H\,I}^{-\beta}$. For narrow ($b \leq 40$ km s^{-1}) absorbers, $\beta = 1.76 \pm 0.06$. The distribution of the Doppler parameter b at low redshift implies two populations: narrow ($b \leq 40$ km s^{-1}) and broad ($b > 40$ km s^{-1}) Lyα absorbers (referred to as NLAs and BLAs, respectively). Both the NLAs and some BLAs probe the cool ($T \sim 10^4$ K) photoionized IGM. The BLAs also probe the highly ionized gas of the warm-hot IGM ($T \simeq 10^5$–10^6 K). The distribution of b has a more prominent high-velocity tail at $z \lesssim 0.4$ than at $1.5 \lesssim z \lesssim 3.6$, which results in median and mean b-values that are 15%–30% higher at low z than at high z. The ratio of the number density of BLAs to NLAs at $z \lesssim 0.4$ is a factor of $\sim$3 higher than at $1.5 \lesssim z \lesssim 3.6$.

Subject headings: cosmology: observations — intergalactic medium — quasars: absorption lines

1. INTRODUCTION

Observations of Lyα absorption lines in the spectra of QSOs provide a sensitive probe of the evolution and the distribution of the gas in the universe from high to low redshift. A forest of H I absorption lines occurs at different redshifts, z, along QSO sight lines with $\log N_{\rm H\,I} < 17$. Understanding the evolution of the Lyα forest with redshift is critical to understanding the evolution and formation of structures in the universe. At $z \gtrsim 1.5$, observations of the Lyα forest are obtained from ground-based telescopes at a spectral resolution of 7–8 km s^{-1} using 8–10 m class telescopes (e.g., Hu et al. 1995; Lu et al. 1996; Kirkman & Tytler 1997; Kim et al. 1997, 2002a), but at $z \leq 1.5$ they require UV space-based instruments. Space-based UV astronomy has produced remarkable results, including the discovery itself of the Lyα forest at low redshift (Bahcall et al. 1991; Morris et al. 1991). However, most of the UV studies of the intergalactic medium (IGM) at low z have lacked the spectral resolution and wavelength coverage of the higher redshift studies (Weymann et al. 1998; Impey et al. 1999; Penton et al. 2000, 2004), requiring assumptions for the Doppler parameter to derive the column density. The situation at $z \lesssim 0.5$ has dramatically improved in the last few years with high-quality observations of several low-redshift QSOs obtained with the *Hubble Space Telescope* (*HST*) and its Space Telescope Imaging Spectrograph (STIS). In its E140M echelle mode, STIS provides a spectral resolution of $\sim$7 km s^{-1}, comparable to the resolution of the high-redshift observations of the Lyα forest. The high spectral resolution has allowed the derivation of accurate Doppler parameters, b, and column densities, N, using techniques similar to those used at high redshift. The Doppler parameter is important because it is related to the temperature of the gas via $b^2 = b_{\rm th}^2 + b_{\rm nt}^2$, where $b_{\rm nt}$ is the nonthermal broadening of the absorption line and $b_{\rm th} = (2kT/m)^{1/2} = 0.129T^{1/2}$ is the thermal broadening of the H I absorption line; therefore, the measured b directly provides an upper limit to the temperature of the observed gas.

In parallel, hydrodynamic cosmological simulations of the local universe have quickly evolved in recent years (Davé et al. 1999, 2001; Cen & Ostriker 1999, 2006; Cen & Fang 2006). These models predict that at low redshift, roughly 30%–50% of the baryons are in a hot (10^5–10^7 K) and highly ionized intergalactic medium (IGM) known as the warm-hot intergalactic medium (WHIM); 30%–40% are in a cooler medium ($\lesssim 10^4$ K) photoionized by the UV background; and the remaining baryons are in galaxies. Observationally, Penton et al. (2004) found, with moderate spectral resolution (FWHM $\sim$ 20 km s^{-1}) UV observations, that the cool phase of the IGM may contain 29% of the baryon budget. The observational detection of the WHIM came first from an intensive search of collisionally ionized O VI systems and other highly ionized species, such as Ne VIII, using space-based observatories such as the *Far Ultraviolet Spectroscopic Explorer* (*FUSE*) and *HST* STIS (e.g., Tripp et al. 2000; Danforth & Shull 2005; Savage et al. 2005). The baryon content of the O VI absorbers suggests that $\Omega_{\rm b}({\rm O\,VI}) \gtrsim 0.0022h_{70}^{-1}$ or at least 5% of the total baryon budget (Sembach et al. 2004; Tripp et al. 2006; Danforth & Shull 2005), but this estimate relies critically on the assumed oxygen abundance and the number of collisionally ionized O VI systems versus photoionized O VI systems (Prochaska et al. 2004; Lehner et al. 2006). The O VI systems probe the lower end of the WHIM temperature range ($T < 10^6$ K). Higher temperatures can be traced with more highly ionized oxygen ions (O VII and O VIII) that can be observed, in principle, with X-ray

[1] Based on observations made with the NASA-CNES-CSA *Far Ultraviolet Spectroscopic Explorer. FUSE* is operated for NASA by The Johns Hopkins University under NASA contract NAS5-32985. Based on observations made with the NASA ESA *Hubble Space Telescope*, obtained at the Space Telescope Science Institute, which is operated by the Association of Universities for Research in Astronomy, Inc. under NASA contract No. NAS5-26555.

[2] Department of Physics, University of Notre Dame, Notre Dame, IN.
[3] Department of Astronomy, University of Wisconsin, Madison, WI.
[4] Argelander-Institut für Astronomie, Universität Bonn, Bonn, Germany.
[5] Space Telescope Science Institute, Baltimore, MD.
[6] Department of Astronomy, University of Massachusetts, Amherst, MA.

observatories such as *Chandra* (Nicastro et al. 2005; Fang et al. 2006) and *XMM-Newton*, but the IGM detections of O VII and O VIII are still controversial (Kaastra et al. 2006; Rasmussen et al. 2007) for $z > 0$.

The WHIM can also be detected through broad H I absorption lines. The high temperature of the WHIM will broaden the Lyα absorption line, resulting in a large Doppler parameter ($b >$ 40 km s^{-1}). A very small fraction of H I (typically $<10^{-5}$) is expected to be found in the highly ionized plasma of the WHIM, so that the broader the H I absorption line is, the shallower it should be. Recent observations, both with moderate spectral resolution and with the higher resolution STIS E140M echelle mode, have revealed the presence of broad H I absorption lines that could be modeled by smooth and broad Gaussian components (Tripp et al. 2001; Bowen et al. 2002; Richter et al. 2004; Sembach et al. 2004; Lehner et al. 2006). H I absorbers with $b < 40$ km s^{-1} imply that the temperature of these absorbers must be $T < 10^5$ K. Since the nominal lower temperature of the WHIM is $T \sim 10^5$ K, it is a priori natural to consider two different physical populations of H I absorbers: the narrow Lyα absorbers (NLAs) as H I systems having $b < 40$ km s^{-1} and the broad Lyα absorbers (BLAs) as H I systems having $b \geq 40$ km s^{-1}. We will see that the separation between the NLAs and BLAs is not so evident observationally, with an important overlap between the two populations, particularly in the range $b = 40$–50 km s^{-1}. While it is clear that the NLAs are tracing mostly the cool photoionized IGM, the situation is less clear for the BLAs. There is a fuzziness in the separation of the BLAs from the NLAs because nonthermal broadening can be important, and unresolved components can hide the true structure of the H I absorbers. Recent simulations show that nonthermal broadening could be particularly important for the H I absorbers with $40 \lesssim b \lesssim 60$ km s^{-1} (Richter et al. 2006a). Therefore, BLAs may probe photoionized gas (which can be either cool [$T \lesssim 10^4$ K] or hot [$T \gtrsim 10^5$ K] but with a very low density [$\log n_{\rm H} < -5.3$]) *and* collisionally ionized, hot ($T \gtrsim 10^5$ K) gas. In this paper, we define a BLA as an absorber that can be fitted with a single Gaussian component with $b > 40$ km s^{-1} (a NLA has $b \leq 40$ km s^{-1} and can have multiple components). BLAs probe the IGM that is either hotter ($b_{\rm th} \gg b_{\rm nt}$) or more kinematically disturbed ($b_{\rm nt} \gg b_{\rm th}$) than the IGM probed by the NLAs. Studying the NLA and BLA populations in detail is also important for estimating the baryon density, because an accurate inventory of the baryon distribution must separate the fraction of the baryons that are located in the cool photoionized IGM versus those that are in the substantially hotter shock-heated WHIM phase. The narrow and broad Lyα lines provide a means to discriminate between the cool and shock-heated gas clouds. Therefore, to make a reliable assessment of the baryonic content of the Lyα forest at low z, it is necessary to investigate the frequency and properties of the NLAs and BLAs. The current estimate of the baryon budget residing in the BLAs over a redshift path $\Delta z = 0.928$ yields $\Omega_{\rm b}({\rm BLA}) \gtrsim 0.0027 h_{70}^{-1}$ or at least 6% of the total baryon budget (Richter et al. 2006b), assuming that the observed broadening is mostly thermal and that collisional ionization equilibrium applies.

In this paper, we address these issues using a sample of seven QSO sight lines that have been observed with both STIS E140M and *FUSE* and for which the data have been fully analyzed using similar techniques and are in press or to be submitted soon. While the spectral resolution of *FUSE* is only $\sim$20 km s^{-1}, compared to $\sim$7 km s^{-1} for STIS E140M, *FUSE* gives access to several Lyman series and metal lines, making the line identification more reliable and providing an unprecedented insight of the physical conditions and metallicity. The fundamental parameters of the Lyα forest lines (redshift z, column density N, and Doppler parameter b) were accurately determined using profile fitting of all the observed Lyman series lines. Because b could be derived, this is the first time that the properties of the Lyα forest in the low-redshift universe can be studied as a function of b with a large sample. The main aims of this work are (1) to study the distribution and evolution of the Doppler parameter of the Lyα forest, and (2) to determine the baryon density of the Lyα forest in the NLA and BLA populations. The organization of this paper is as follows: § 2 describes the sample and its completeness; in § 3 we study the distribution of the Doppler parameter b and the Lyα density number as a function of b; in § 4 we study the evolution of b with redshift by comparing the low-z ($z \lesssim 0.4$) Lyα forest with the mid-z ($0.5 \lesssim z \lesssim 1.5$) and high-$z$ ($1.5 \lesssim z \lesssim 3.6$) Ly$\alpha$ forest; in § 5 we estimate the column density distribution; and finally, in § 6 we estimate the baryon content of the cool photoionized IGM probed by the NLAs and the photoionized IGM and the WHIM probed by the BLAs, and we discuss the uncertainties in estimating the baryon budget. We summarize our results in § 7.

TABLE 1
LINE-OF-SIGHT PROPERTIES

Sight Line (1)	S/N (2)	z (3)	Δz (4)	ΔX (5)	References (6)
H1821+643	15–20	0.297	0.238	0.266	1
HE 0226−4110	5–11	0.495	0.401	0.481	2
HS 0624+6907	8–12	0.370	0.329	0.383	3
PG 0953+415	7–11	0.239	0.202	0.222	4
PG 1116+215	10–15	0.176	0.126	0.134	5
PG 1259+593	9–17	0.478	0.355	0.418	6
PKS 0405−123	5–10	0.574	0.413	0.498	7

NOTES.—Col. (2): Range of signal-to-noise ratio (S/N) per resolution element in STIS E140M mode. Col. (3): QSO redshift. Col. (4): Unblocked redshift path for Lyα. Col. (5): Absorption distance (see § 2).

REFERENCES.—(1) K. R. Sembach et al. 2007, in preparation; (2) Lehner et al. 2006; (3) Aracil et al. 2006a, 2006b; (4) T. M. Tripp 2006, private communication; (5) Sembach et al. 2004; (6) Richter et al. 2004; (7) Williger et al. 2006 and the Appendix of this paper.

2. THE LOW-z SAMPLE

2.1. *Description of the Sample and Completeness*

Our low-z sample consists of seven QSO sight lines that were observed with *HST* STIS E140M and *FUSE*: H1821+643 (K. R. Sembach et al. 2007, in preparation; see also Tripp et al. 2000; Oegerle et al. 2000 for the metal-line systems), HE 0226−4110 (Lehner et al. 2006), HS 0624+6907 (Aracil et al. 2006a), PG 0953+415 (T. M. Tripp 2006, private communication; see also Savage et al. 2002 for the metal-line systems), PG 1259+593 (Richter et al. 2004), PG 1116+215 (Sembach et al. 2004), and PKS 0405−123 (Williger et al. 2006; see also Prochaska et al. 2004 for the metal-line systems). Note that for HS 0624+6907, we used the results summarized in the erratum produced by Aracil et al. (2006b). The data handling and analysis are described in detail in the above papers. For PKS 0405−123, we adopt the new measurements and a new line list that we describe in the Appendix. The motivation to revisit Williger et al.'s analysis was first driven by differentiating a real detection from a noise feature for the BLAs, since these authors noted that several of their BLAs could be just noise. This reanalysis also provides an overall coherent data sample that was analyzed following the same methodology. The signal-to-noise ratio (S/N) where Lyα can be observed, redshift (z), unblocked redshift path (Δz), and absorption distance (ΔX) are summarized in Table 1 for each sight line. The absorption

TABLE 2
H I Measurements

z	$\log N_{\rm H\,I}$ (dex)	b (km s^{-1})
H1821+643 (K. R. Sembach et al. 2007, in preparation)		
0.02438	$14.28^{+0.06}_{-0.05}$	26.9 ± 1.7
0.02642	$13.26^{+0.07}_{-0.08}$	48.6 ± 6.0
0.06718	$13.72^{+0.01}_{-0.01}$	20.2 ± 0.6
0.07166	$13.87^{+0.02}_{-0.02}$	34.0 ± 1.0
0.08911	$13.01^{+0.06}_{-0.07}$	23.3 ± 2.8
0.11133	$12.95^{+0.10}_{-0.13}$	88.0 ± 14.0
0.11166	$12.99^{+0.08}_{-0.09}$	28.6 ± 4.4
0.11961	$13.15^{+0.05}_{-0.06}$	36.8 ± 3.4
0.12055	$12.64^{+0.13}_{-0.18}$	22.5 ± 5.9
0.12112	13.93 ± 0.37	$26.0^{+13.0}_{-9.0}$
0.12125	14.04 ± 0.36	$40.0^{+44.0}_{-21.0}$
0.12147	13.78 ± 0.17	$85.0^{+37.0}_{-26.0}$
0.12221	$13.19^{+0.06}_{-0.06}$	41.7 ± 4.4
0.14754	$13.51^{+0.03}_{-0.03}$	44.6 ± 2.5
0.14776	$13.30^{+0.04}_{-0.05}$	19.2 ± 1.6
0.15731	$13.11^{+0.05}_{-0.06}$	22.9 ± 2.1
0.16127	$12.74^{+0.10}_{-0.12}$	21.5 ± 4.0
0.16352	$13.17^{+0.06}_{-0.07}$	52.2 ± 5.9
0.16966	$13.93^{+0.02}_{-0.02}$	35.7 ± 2.0
0.17001	$13.65^{+0.02}_{-0.02}$	...
0.17051	$13.40^{+0.04}_{-0.04}$	21.1 ± 1.4
0.17926	$12.87^{+0.09}_{-0.12}$	18.4 ± 3.4
0.18047	$13.14^{+0.07}_{-0.08}$	50.7 ± 6.6
0.19662	$12.98^{+0.07}_{-0.08}$	21.1 ± 2.7
0.19904	$12.74^{+0.12}_{-0.17}$	22.1 ± 5.4
0.20957	$13.10^{+0.03}_{-0.04}$	16.2 ± 0.9
0.21161	$13.16^{+0.06}_{-0.06}$	22.3 ± 2.3
0.21668	$12.88^{+0.08}_{-0.10}$	19.7 ± 3.0
0.21326	$14.41^{+0.04}_{-0.04}$	43.0 ± 2.4
0.22497	$15.53^{+0.05}_{-0.05}$	25.0 ± 7.0
0.22616	$13.51^{+0.04}_{-0.04}$	54.7 ± 3.8
0.22786	$13.26^{+0.03}_{-0.04}$	35.3 ± 2.0
0.23869	$12.86^{+0.10}_{-0.12}$	20.2 ± 3.8
0.24142	$13.12^{+0.03}_{-0.04}$	23.4 ± 1.4
0.24531	$13.06^{+0.08}_{-0.10}$	34.2 ± 5.1
0.25689	$12.80^{+0.11}_{-0.15}$	22.6 ± 5.1
0.25814	$13.38^{+0.10}_{-0.13}$	60.3 ± 8.8
0.25816	$12.98^{+0.11}_{-0.15}$	14.5 ± 3.4
0.26152	$13.70^{+0.02}_{-0.03}$	37.7 ± 1.5
0.26659	$13.64^{+0.03}_{-0.03}$	44.5 ± 2.1
HE 0226−4110 (Lehner et al. 2006)		
0.01746	13.22 ± 0.06	17.9 ± 4.3
0.02679	13.22 ± 0.08	41.6 ± 11.0
0.04121	12.82 ± 0.14	23.6 ± 18.6
0.04535	12.71 ± 0.13	16.2 ± 12.8
0.04609	13.66 ± 0.03	25.0 ± 2.1
0.06015	13.19 ± 0.06	35.5 ± 7.6
0.06083	14.65 ± 0.02	44.5 ± 1.0
0.07023	13.81 ± 0.11	26.0 ± 12.4
0.08375	13.67 ± 0.05	29.6 ± 4.5
0.08901	13.33 ± 0.05	23.8 ± 3.7
0.08938	12.59 ± 0.22	8.2:
0.08950	12.72 ± 0.20	22.0:
0.09059	13.71 ± 0.03	28.3 ± 2.0
0.09220	12.94 ± 0.11	40.2 ± 18.0
0.10668	13.09 ± 0.08	32.7 ± 9.2
0.11514	12.90 ± 0.09	10.4 ± 4.1
0.11680	13.27 ± 0.05	23.7 ± 3.9
0.11733	12.64 ± 0.15	15.0:
0.12589	13.01 ± 0.09	29.2 ± 10.1
0.13832	13.19 ± 0.06	25.9 ± 5.3

TABLE 2—*Continued*

z	$\log N_{\rm H\,I}$ (dex)	b (km s^{-1})
HE 0226−4110 (Lehner et al. 2006)		
0.15175	13.42 ± 0.05	48.6 ± 6.7
0.15549	13.13 ± 0.08	34.7 ± 9.8
0.16237	13.04 ± 0.08	29.7 ± 8.6
0.16339	14.36 ± 0.04	46.3 ± 1.9
0.16971	13.35 ± 0.05	25.3 ± 3.9
0.18619	13.26 ± 0.08	53.9 ± 16.2
0.18811	13.47 ± 0.05	22.4 ± 3.3
0.18891	13.34 ± 0.07	22.2 ± 4.0
0.19374	13.20 ± 0.06	28.7 ± 6.0
0.19453	12.89 ± 0.12	26.1 ± 14.0
0.19860	14.18 ± 0.04	37.0 ± 2.0
0.20055	13.38 ± 0.05	38.9 ± 6.4
0.20698	13.31 ± 0.34	97.0:
0.20700	15.06 ± 0.04	17.4 ± 1.4
0.20703	14.89 ± 0.05	35.9 ± 1.1
0.22005	14.40 ± 0.04	27.7 ± 1.1
0.22099	12.99 ± 0.12	34.1 ± 18.1
0.23009	13.69 ± 0.04	67.9 ± 7.5
0.23964	13.13 ± 0.08	28.8 ± 8.8
0.24514	14.20 ± 0.03	34.5 ± 1.6
0.25099	13.17 ± 0.08	37.9 ± 11.5
0.27147	13.85 ± 0.07	25.7 ± 4.2
0.27164	13.33 ± 0.28	26.2:
0.27175	12.88 ± 0.38	11.2:
0.27956	13.22 ± 0.14	36.3 ± 24.6
0.28041	13.03 ± 0.11	13.9 ± 6.7
0.29134	13.53 ± 0.07	27.0 ± 6.2
0.29213	13.19 ± 0.12	33.4 ± 17.8
0.30930	14.26 ± 0.03	43.8 ± 2.3
0.34034	13.68 ± 0.06	33.4 ± 4.9
0.35523	13.60 ± 0.07	27.1 ± 6.8
0.37281	13.16 ± 0.12	25.9 ± 13.3
0.38420	13.91 ± 0.04	62.0 ± 7.1
0.38636	13.36 ± 0.09	38.1 ± 12.7
0.39641	13.59 ± 0.10	62.8 ± 22.7
0.39890	13.50 ± 0.16	151.7:
0.40034	13.39 ± 0.11	60.7 ± 26.1
0.40274	14.13 ± 0.04	45.7 ± 4.2
HS 0624+6907 (Aracil et al. 2006b)		
0.01755	12.96 ± 0.05	29.0 ± 4.3
0.03065	13.36 ± 0.03	22.0 ± 1.7
0.04116	13.33 ± 0.03	41.0 ± 3.0
0.05394	13.26 ± 0.04	24.0 ± 2.3
0.05437	13.09 ± 0.11	60.0 ± 19.2:
0.05483	14.50:	35.0:
0.05515	13.68 ± 0.17	84.0 ± 30.7:
0.06188	13.77 ± 0.03	21.0 ± 1.4
0.06201	12.63 ± 0.17	8.0 ± 4.7
0.06215	12.41 ± 0.22	10.0 ± 7.9
0.06234	13.45 ± 0.05	30.0 ± 4.0
0.06265	13.31 ± 0.14	35.0 ± 12.3
0.06276	12.95 ± 0.28	8.0 ± 3.7
0.06285	13.42 ± 0.14	20.0 ± 7.0
0.06304	13.33 ± 0.13	27.0 ± 8.8
0.06346	14.46 ± 0.30	48.0 ± 8.4:
0.06348	15.27 ± 0.13	24.0 ± 5.5
0.06362	14.29 ± 0.38	10.0 ± 5.6
0.06475	13.87 ± 0.04	33.0 ± 3.0
0.06502	13.97 ± 0.04	31.0 ± 2.7
0.07573	14.18 ± 0.03	24.0 ± 0.8
0.09023	13.29 ± 0.08	76.0 ± 13.7
0.13076	13.34 ± 0.04	34.0 ± 3.6

TABLE 2—*Continued*

z	$\log N_{\rm H\,I}$ (dex)	b (km s^{-1})
HS 0624+6907 (Aracil et al. 2006b)		
0.13597	13.33 ± 0.10	57.0 ± 10.7
0.16054	13.08 ± 0.21	34.0 ± 10.3
0.16074	13.66 ± 0.05	30.0 ± 2.4
0.19975	13.24 ± 0.05	17.0 ± 2.0
0.19995	13.17 ± 0.06	26.0 ± 4.6
0.20483	13.72 ± 0.02	24.0 ± 1.0
0.20533	14.12 ± 0.03	25.0 ± 0.8
0.20754	13.48 ± 0.02	27.0 ± 1.5
0.21323	13.22 ± 0.05	45.0 ± 5.6
0.21990	13.39 ± 0.05	60.0 ± 8.6
0.22329	13.86 ± 0.02	25.0 ± 0.9
0.23231	13.33 ± 0.08	44.0 ± 7.7:
0.23255	12.86 ± 0.21	24.0 ± 7.3
0.24060	13.33 ± 0.04	20.0 ± 2.0
0.25225	12.96 ± 0.06	24.0 ± 4.2
0.26856	13.03 ± 0.05	51.0 ± 7.2
0.27224	12.80 ± 0.06	12.0 ± 2.2
0.27977	13.50 ± 0.06	34.0 ± 4.9
0.28017	14.32 ± 0.02	43.0 ± 1.9
0.29531	13.80 ± 0.02	42.0 ± 2.0:
0.29661	13.54 ± 0.02	52.0 ± 2.9
0.30899	13.49 ± 0.03	28.0 ± 1.8
0.30991	13.61 ± 0.10	66.0 ± 12.3:
0.31045	13.43 ± 0.33	62.0 ± 40.3:
0.31088	13.13 ± 0.43	51.0 ± 27.7
0.31280	13.65 ± 0.10	54.0 ± 9.3
0.31303	13.09 ± 0.24	17.0 ± 6.8
0.31326	13.62 ± 0.10	55.0 ± 10.9
0.31790	13.37 ± 0.04	34.0 ± 3.6
0.32089	13.97 ± 0.02	31.0 ± 1.2
0.32724	13.73 ± 0.32	69.0 ± 15.6:
0.32772	13.61 ± 0.43	115.0 ± 62.1:
0.33267	13.55 ± 0.04	38.0 ± 3.4
0.33976	14.45 ± 0.03	42.0 ± 1.3
0.34682	13.59 ± 0.02	39.0 ± 1.9
0.34865	12.78 ± 0.06	18.0 ± 3.0
PG 0953+415 (T. M. Tripp 2006, private communication)		
0.01558	13.19 ± 0.08	$35.0^{+10.0}_{-8.0}$
0.01587	12.86 ± 0.21	$19.0^{+15.0}_{-8.0}$
0.01606	13.54 ± 0.05	32.0 ± 5.0
0.01655	13.51 ± 0.04	26.0 ± 3.0
0.02336	13.21 ± 0.08	$56.0^{+14.0}_{-11.0}$
0.04416	12.72 ± 0.09	15.0 ± 6.0
0.04469	12.77 ± 0.06	12.0 ± 3.0
0.04512	13.42 ± 0.02	38.0 ± 2.0
0.05876	13.82 ± 0.07	25.0 ± 3.0
0.05879	13.41 ± 0.16	$63.0^{+19.0}_{-14.0}$
0.06808	14.47 ± 0.03	21.0 ± 2.0
0.09228	13.08 ± 0.07	27.0 ± 6.0
0.09315	13.66 ± 0.03	39.0 ± 3.0
0.10940	13.68 ± 0.03	23.0 ± 2.0
0.11558	13.47 ± 0.03	24.0 ± 2.0
0.11826	13.68 ± 0.02	30.0 ± 2.0
0.11871	12.81 ± 0.10	16.0 ± 6.0
0.12558	12.77 ± 0.09	$8.0^{+4.0}_{-3.0}$
0.12784	12.83 ± 0.35	$44.0^{+76.0}_{-28.0}$
0.12804	13.27 ± 0.12	21.0 ± 5.0
0.14178	12.68 ± 0.10	$10.0^{+5.0}_{-3.0}$
0.14233	13.58 ± 0.03	28.0 ± 2.0
0.14263	13.45 ± 0.04	31.0 ± 4.0
0.14294	12.63 ± 0.27	$17.0^{+23.0}_{-10.0}$
0.14310	13.05 ± 0.11	$22.0^{+9.0}_{-6.0}$

TABLE 2—*Continued*

z	$\log N_{\rm H\,I}$ (dex)	b (km s^{-1})
PG 0953+415 (T. M. Tripp 2006, private communication)		
0.14333	12.77 ± 0.14	$15.0^{+9.0}_{-6.0}$
0.17985	13.27 ± 0.07	$48.0^{+11.0}_{-9.0}$
0.19072	13.04 ± 0.08	26.0 ± 6.0
0.19126	13.08 ± 0.55	$48.0^{+95.0}_{-32.0}$
0.19147	13.33 ± 0.34	$30.0^{+12.0}_{-9.0}$
0.19210	13.14 ± 0.07	28.0 ± 6.0
0.19241	12.94 ± 0.12	$35.0^{+15.0}_{-11.0}$
0.19361	13.94 ± 0.02	40.0 ± 2.0
0.20007	13.24 ± 0.09	$66.0^{+17.0}_{-14.0}$
0.20104	13.16 ± 0.16	$71.0^{+41.0}_{-26.0}$
0.20136	12.91 ± 0.19	$19.0^{+10.0}_{-7.0}$
0.20895	12.94 ± 0.10	$28.0^{+10.0}_{-7.0}$
0.21514	13.30 ± 0.04	27.0 ± 3.0
0.22526	12.74 ± 0.23	$2.0^{+2.0}_{-1.0}$
0.22527	13.19 ± 0.05	34.0 ± 5.0
PG 1116+215 (Sembach et al. 2004)		
0.00493	$13.36^{+0.07}_{-0.06}$	34.2 ± 3.6
0.01635	13.39 ± 0.06	48.5 ± 5.1
0.02827	13.80 ± 0.02	31.4 ± 1.1
0.03223	$13.33^{+0.06}_{-0.05}$	31.6 ± 2.9
0.04125	$13.25^{+0.11}_{-0.09}$	105.0 ± 18.0
0.04996	$12.72^{+0.10}_{-0.08}$	16.5 ± 3.2
0.05895	13.56 ± 0.05	25.0 ± 5.0
0.05928	$12.41^{+0.18}_{-0.13}$	10.0:
0.06072	$13.28^{+0.06}_{-0.05}$	55.4 ± 5.8
0.06244	$13.18^{+0.07}_{-0.06}$	77.3 ± 9.0
0.07188	$12.79^{+0.08}_{-0.07}$	9.6 ± 2.0
0.08096	$13.45^{+0.03}_{-0.02}$	24.9 ± 1.0
0.08587	$12.90^{+0.19}_{-0.13}$	52.0 ± 14.0
0.08632	$12.66^{+0.32}_{-0.18}$	36.0 ± 15.0
0.09279	$13.39^{+0.09}_{-0.08}$	133.0 ± 17.0
0.10003	$12.73^{+0.07}_{-0.06}$	23.2 ± 2.2
0.11895	$13.44^{+0.04}_{-0.03}$	31.5 ± 1.8
0.13151	13.41 ± 0.03	28.8 ± 1.3
0.13370	$13.27^{+0.08}_{-0.07}$	83.6 ± 10.4
0.13847	$16.20^{+0.05}_{-0.04}$	22.4 ± 0.3
PG 1259+593 (Richter et al. 2004)		
0.00229	13.57 ± 0.10	42.1 ± 4.4
0.00760	14.05 ± 0.05	34.6 ± 2.0
0.01502	13.21 ± 0.06	22.6 ± 4.4
0.02217	13.67 ± 0.04	30.2 ± 2.2
0.03924	12.94 ± 0.05	15.3 ± 2.8
0.04606	15.58 ± 0.21	47.6 ± 12.4
0.05112	13.62 ± 0.07	34.4 ± 2.5
0.05257	12.75 ± 0.06	20.7 ± 3.0
0.05376	13.44 ± 0.04	30.5 ± 1.9
0.06644	13.65 ± 0.05	28.7 ± 3.3
0.08041	12.97 ± 0.10	42.0 ± 4.5
0.08933	14.04 ± 0.03	28.9 ± 1.7
0.09591	12.97 ± 0.03	21.5 ± 2.3
0.12188	13.03 ± 0.07	26.9 ± 4.2
0.12387	13.47 ± 0.06	28.2 ± 3.0
0.14852	13.91 ± 0.06	42.1 ± 2.4
0.15029	13.25 ± 0.11	25.7 ± 4.3
0.15058	13.45 ± 0.13	32.0 ± 5.1
0.15136	13.32 ± 0.09	65.3 ± 5.5
0.15435	13.22 ± 0.04	25.2 ± 1.9
0.17891	13.29 ± 0.10	98.5 ± 9.1
0.18650	13.02 ± 0.03	19.6 ± 1.4
0.19620	13.65 ± 0.05	32.7 ± 3.2

TABLE 2—*Continued*

z	$\log N_{\rm H\,I}$ (dex)	b (km s^{-1})
PG 1259+593 (Richter et al. 2004)		
0.19775	13.33 ± 0.06	23.9 ± 2.8
0.21949	15.08 ± 0.08	32.3 ± 1.4
0.22313	13.92 ± 0.04	34.8 ± 1.1
0.22471	13.59 ± 0.06	28.9 ± 1.7
0.22861	13.47 ± 0.05	40.3 ± 2.9
0.23280	13.50 ± 0.07	37.4 ± 3.2
0.23951	13.40 ± 0.03	16.3 ± 1.3
0.24126	13.41 ± 0.09	89.1 ± 6.9
0.25642	13.74 ± 0.03	25.0 ± 0.9
0.25971	13.84 ± 0.12	40.5 ± 4.9
0.28335	13.59 ± 0.10	37.0 ± 5.2
0.29236	14.65 ± 0.09	24.3 ± 2.8
0.29847	13.09 ± 0.10	33.3 ± 2.9
0.30164	13.26 ± 0.14	31.7 ± 4.7
0.30434	13.76 ± 0.14	64.5 ± 9.6
0.31070	13.40 ± 0.07	22.8 ± 2.9
0.31978	13.98 ± 0.06	74.4 ± 8.7
0.32478	13.24 ± 0.15	46.1 ± 10.2
0.33269	13.88 ± 0.08	25.9 ± 3.2
0.34477	14.02 ± 0.08	34.3 ± 4.4
0.34914	13.36 ± 0.09	31.3 ± 4.8
0.35375	13.41 ± 0.06	16.4 ± 1.8
0.37660	13.45 ± 0.13	36.4 ± 6.2
0.38833	13.02 ± 0.19	14.1 ± 3.8
0.41081	13.57 ± 0.08	32.8 ± 5.0
0.41786	13.25 ± 0.08	50.7 ± 3.9
0.43148	14.10 ± 0.06	20.9 ± 4.3
0.43569	14.22 ± 0.10	44.0 ± 3.9
PKS 0405−123 (this paper)		
See Table 9		

distance was computed assuming a Friedmann cosmology, $\Delta X = 0.5[(1+\Delta z)^2 - 1]$ with $q_0 = 0$. For the lines of sight to QSOs with $z_{\rm QSO} < 0.42$, we have excluded absorption systems within 5000 km s^{-1} of the QSO redshift. Some observations of low-redshift QSOs have provided evidence that "intrinsic" absorption lines can arise in clouds that are spatially close to the QSO and yet, due to the cloud kinematics, are substantially offset in redshift from the QSO (e.g., Yuan et al. 2002; Ganguly et al. 2003). To avoid contaminating the sample with these intrinsic absorbers, we do not use systems detected within 5000 km s^{-1} of the QSO. The Voigt profile-fitting method was employed for each line of sight to measure the column densities ($N_{\rm H\,I}$), Doppler parameters (b), and redshifts of the absorbers, and we adopt those results for our analysis. Table 2 lists these parameters. For PG 1259+593 we did not include in our sample the systems marked uncertain (UC) in Table 5 of Richter et al. (2004). A colon in Table 2 indicates that there is uncertainty in the determination of the physical parameters, which are not accounted for in the formal errors produced by the profile fitting. These systems are not taken into account when we use an error cutoff (see below). If we had, it would not have changed the results presented in this paper in a statistically significant manner.

The total sample consists of 341 H I systems, with a total unblocked redshift path $\Sigma\Delta z = 2.064$ and a total absorption distance $\Sigma\Delta X = 2.404$. There are 201 systems at $z \leq 0.2$ and 131 systems at $0.2 < z \leq 0.4$. The remaining 9 systems lie at $0.4 < z < 0.44$. Therefore, our sample mostly probes the universe at $z \leq 0.4$. More absorbers are found at $z < 0.2$ because several lines of sight do not extend out to $z = 0.3$–0.4 and to a lesser extent because the S/N at $\lambda > 1650$ Å decreases rapidly (see below).

The sample is not homogeneous with respect to the achieved S/N in the STIS E140M observations toward the seven sight lines considered. The detection limit depends on the S/N and the breadth over which the spectrum is integrated. The matter is complicated by the S/N not being constant over the full wavelength range from ~1216 to ~1730 Å available with STIS E140M where Lyα can be observed; in particular, it deteriorates rapidly at $\lambda > 1650$ Å. Only lines of sight with $z \gtrsim 0.32$ can reach the last 100 Å of the STIS E140M wavelength coverage. Note that 297 systems with $z \leq 0.32$ are observed at wavelengths $\lambda \lesssim 1650$ Å. For example, in one of the lowest S/N spectra in our sample (HE 0226−4110), we estimate that at ~1700 Å, a 3 σ limit is ~75 mÅ for the profile integrated over $\delta v = [-50, 50]$ km s^{-1} and ~100 mÅ over $\delta v = [-90, 90]$ km s^{-1}. We estimate that our sample is complete for $\log N_{\rm H\,I} \gtrsim 13.20$ (corresponding to a rest frame equivalent width $W_{1215} \simeq 88$ mÅ) at a 3 σ level for $b \lesssim 80$ km s^{-1}. For the high-S/N lines of sight (H1821+643, PG 1259+593, and PG 1116+215), this limit is quite conservative. For systems with $b > 80$ km s^{-1} and $\log N_{\rm H\,I} \gtrsim 13.20$, our sample is incomplete, especially at $z \geq 0.32$ and for the lowest S/N spectra.

Since our sample is not homogeneous with respect to the achieved S/N, it is useful to have a sample in which the cloud parameters are relatively well determined, so that scatter due to noise is reduced. We therefore consider systems with errors on b and $N_{\rm H\,I}$ that are less than 40%. The sample has 270 H I systems with errors on b and $N_{\rm H\,I}$ that are less than 40%. In this case, there are 155 systems at $z \leq 0.2$, 107 systems at $0.2 < z \leq 0.4$, and 8 systems at $0.4 < z < 0.44$. At the completeness level $\log N_{\rm H\,I} \geq 13.20$ and with errors on b and $N_{\rm H\,I}$ less than 40%, there is a total of 202 H I systems, with 109 systems at $z \leq 0.2$, 85 systems at $0.2 < z \leq 0.4$, and 8 systems at $0.4 < z < 0.44$.

2.2. *Overview of the Distributions of $N_{\rm H\,I}$, b, and z*

In Figure 1, we show the distribution of the column density for each line of sight and the total sample (last panel, where we show the completeness limit of the sample) for systems with $N_{\rm H\,I} \leq 10^{14}$ cm^{-2} and $\sigma_b/b, \sigma_N/N \leq 0.4$. About 86% of the absorbers have $N_{\rm H\,I} \leq 10^{14}$ cm^{-2} and ~94% of them have $N_{\rm H\,I} \leq 10^{14.5}$ cm^{-2}. The column density distribution peaks near $N_{\rm H\,I} \sim 2 \times 10^{13}$ cm^{-2} and drops sharply at smaller column densities. Since the peak of the distribution corresponds to about our completeness limit, the observed decrease of the number of systems at $N_{\rm H\,I} \lesssim 1.6 \times 10^{13}$ cm^{-2} can be understood from the reduction in sensitivity. Higher S/N spectra would be needed to further understand the distribution of the smaller column densities.

In Figure 2, we show the distribution of the Doppler parameters for each line of sight and for the entire sample (*last panel*) with $\sigma_b/b, \sigma_N/N \leq 0.4$. For every sight line, the b-distribution peaks between about 20 and 30 km s^{-1}. Yet, it is apparent that the distribution is not Gaussian around these values, and, in particular, there are many systems with $b \gtrsim 40$–50 km s^{-1} that produce a tail in the b distribution. This is clearly observed in the histogram of the combined sample, where b peaks around 20–30 km s^{-1} and there is an excess of systems with $b > 40$ km s^{-1}, compared to the number of systems with small b. This preview already shows clearly that a mean b-value does not provide an adequate description of the Lyα forest.

In Figure 3, we show the distribution of the redshift for each line of sight with a redshift bin of 0.0033 (corresponding to 1000 km s^{-1} intervals). There is no striking difference between

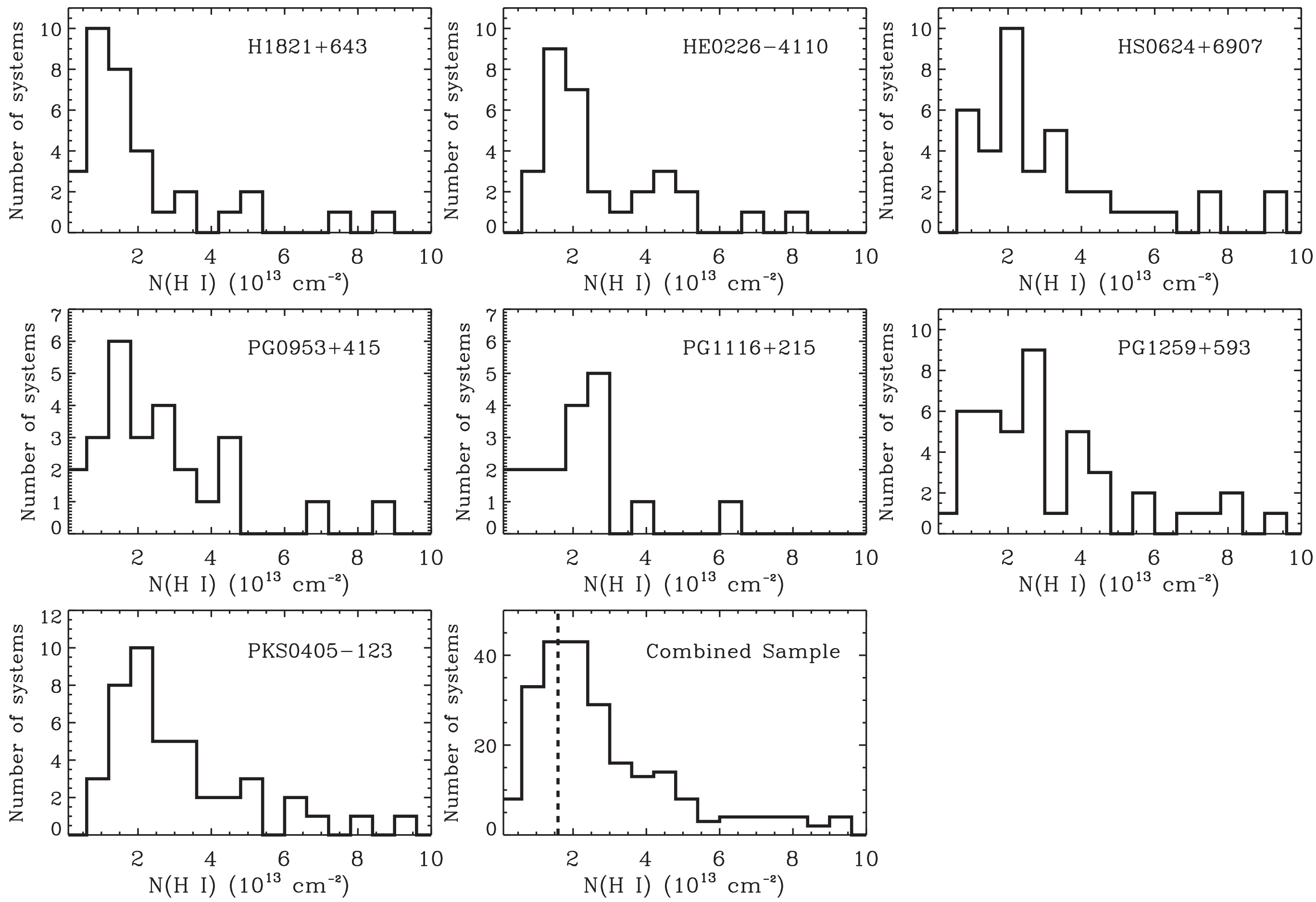

FIG. 1.—Distribution of the column density of H I for each sight line and the combined sample with a column density interval of 6×10^{12} cm^{-2}. Only data with $N_{\rm H\,I} \leq 10^{14}$ cm^{-2} and less than 40% errors in b and $N_{\rm H\,I}$ are considered. The vertical dashed line on the complete sample marks the completeness limit of $N_{\rm H\,I} = 1.6 \times 10^{13}$ cm^{-2}.

the different lines of sight, but there are clearly voids and clustering in the distribution, consistent with the Lyα forest tracing filaments of matter in the universe. An example of clustering of absorbers is found near the system at $z = 0.06352$ toward HS 0624+6907, where at least 8 absorbers are found in a single bin and 17 absorbers are only separated by about 3000 km s^{-1}. Aracil et al. (2006a) attribute this clustering to the absorption of intragroup gas, possibly from a filament viewed along its long axis.

3. DISTRIBUTION OF b

Earlier low-redshift UV studies of the H I forest have low or moderate spectral resolutions and smaller wavelength coverage, and they did not allow access to several Lyman series transitions. Therefore, the Doppler parameter b generally had to be assumed, and a study of the evolution and distribution of b was not possible (see, e.g., the studies of Weymann et al. 1998; Penton et al. 2000, 2004). With STIS E140M observations (spectral resolution of 6.5 km s^{-1}), b can be derived from a profile-fitting analysis. Furthermore, combining STIS E140M and *FUSE* observations allows further constraints on b by using several Lyman series lines and reducing possible misidentifications. Here, we review the frequency and properties of the narrow Lyα absorbers (NLAs, $b \leq 40$ km s^{-1}) and the broad Lyα absorbers (BLAs, $b > 40$ km s^{-1}).

3.1. *Distribution of b and Other Low-z Studies*

The median b-value of 31 km s^{-1} for our combined sample is larger than the medians found in the low-redshift IGM studies by Davé & Tripp (2001) and Shull et al. (2000). Davé & Tripp (2001) used automated software to derive b and N, but their criteria did not allow a search for broad components. Shull et al. (2000) only went after the Lyβ absorption lines in the *FUSE* wavelength range in order to combine them with known Lyα absorption lines observed with the Goddard High Resolution Spectrograph (GHRS) and were therefore less likely to find the broad H I absorbers. Davé & Tripp (2001) found median and mean b-values of 22 and 25 km s^{-1}, respectively. We find that the distribution of b is not Gaussian, making the mean and dispersion less useful quantities. If we restrict our sample to data with $b \leq 40$ km s^{-1}, the median and mean (with 1 σ dispersion) are 27 and 27 ± 7 km s^{-1}. If only data with $\log N_{\rm H\,I} \gtrsim 13.2$ are considered, we obtain 29 and 28 ± 6 km s^{-1}. If we set the cutoff at $b \leq 50$ km s^{-1}, the median and the mean increase by 2 km s^{-1}. The median, mean, and dispersion of b in our sample (with $b \leq 40$ or 50 km s^{-1}) compare well to those derived by Shull et al. (2000): 28 and 31 ± 7 km s^{-1} for the median and mean, respectively.

In Figure 4, we show the distribution of b for samples with various $N_{\rm H\,I}$ cutoffs. For any $N_{\rm H\,I}$ cutoff, the maximum of the distribution always peaks near 25–30 km s^{-1}, and in all cases there is clearly an asymmetry in the distribution, with the presence of a tail in the distribution that develops at $b > 40$–60 km s^{-1}. For the BLAs, the number of systems with H I column between 13.0 and 13.2 dex is the largest, although this could be in part an observational bias, since weaker column density absorbers with $b > 40$ km s^{-1} would require higher S/N to be detected. Although the effects of line blending can contaminate

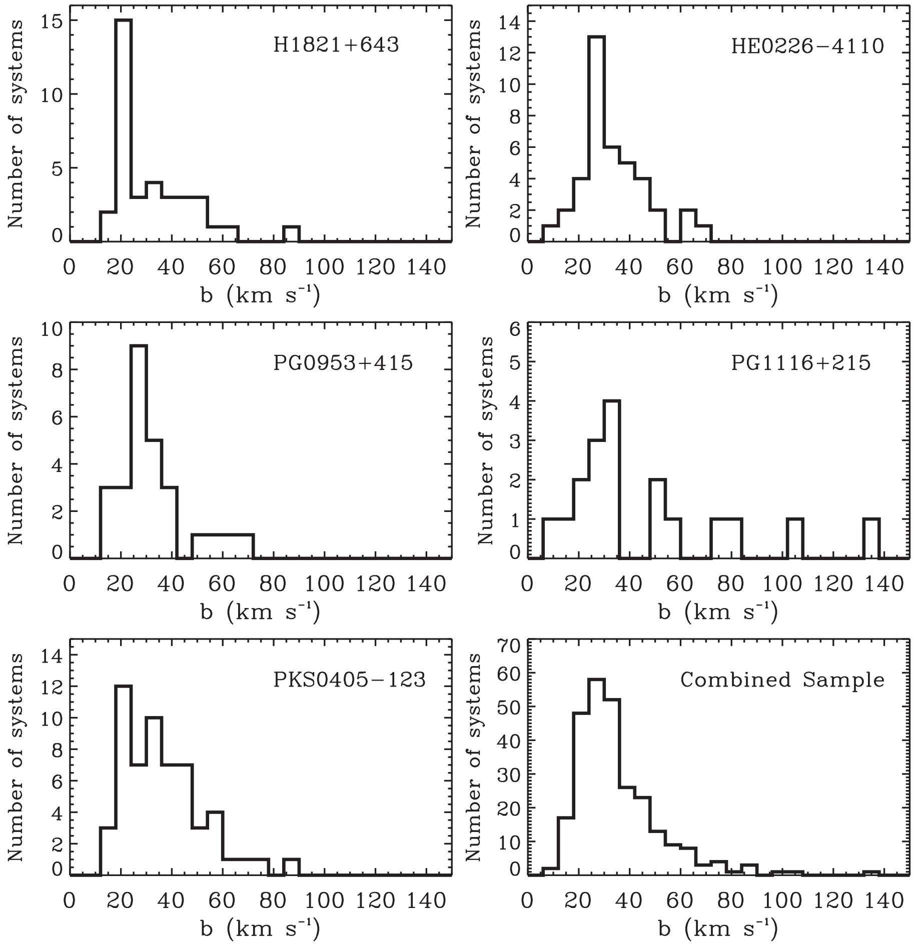

FIG. 2.—Distribution of the Doppler parameter of H I for each sight line and the combined sample. The observations are plotted in 6 km s^{-1} bins. Only data with less than 40% errors in b and $N_{\rm H\,I}$ are considered.

the measurements of the observed tails, the various papers describing the data (see also Richter et al. 2006b) show that a large fraction of these broad absorbers can be described with a single Gaussian within the S/N. For the stronger of these absorbers, several Lyman series lines were also used to derive the physical parameters.

3.2. *The b-$N_{\rm H\,I}$ Distribution*

The b-$N_{\rm H\,I}$ distribution of the low-redshift sample is shown in Figure 5. The solid gray line shows the threshold detection of H I absorbers. This curve is the relationship between b and $N_{\rm H\,I}$ for a Gaussian line profile with 10% central optical depth; absorption lines to the left of this line are not detectable. The lack of data with low b and $\log N_{\rm H\,I} \lesssim 12.7$ is most likely because our sample is not complete at these low column densities. When absorbers with $\log N_{\rm H\,I} \gtrsim 13.2$ and $b > 0$ km s^{-1} are considered, the b-$N_{\rm H\,I}$ plot reveals mostly a scatter diagram. Most of the absorbers are present in the column density range 13.2–14 dex. In Table 3, we list the median, mean, and dispersion of b for the entire sample, NLAs, and BLAs. For the entire sample, as expected from Figure 5, it is not clear whether b increases or decreases as $N_{\rm H\,I}$ increases. A Spearman rank-order correlation test on the entire sample with $\log N_{\rm H\,I} \geq 13.2$ shows a very marginal negative correlation between b and $N_{\rm H\,I}$, with a rank-order correlation coefficient $r = -0.08$ and a statistical significance $t = 0.25$. We note that when systems with $\log N_{\rm H\,I} \lesssim 13.2$ are considered, it creates an apparent correlation ($r = 0.21$ and $t = 4.7 \times 10^{-4}$) between $N_{\rm H\,I}$ and b, which can be understood in terms of measurement biases, since weak broad systems are more difficult to detect than weak narrow absorbers. There is no clear separation between the NLAs and BLAs in this figure, although we note that most BLAs are found at $\log N_{\rm H\,I} \lesssim 14.0$ and no BLAs with $b > 50$ km s^{-1} have $\log N_{\rm H\,I} \gtrsim 14.0$ (see below). This scatter and absence of clear separation between NLAs and BLAs are expected if the H I lines trace systems with different temperatures *and* turbulent velocities.

For NLAs with $b \leq 40$ km s^{-1} and $\log N_{\rm H\,I} \geq 13.2$, we show in Figure 5 the median, mean, and dispersion of b (*red curves and symbols*) derived in six intervals of $N_{\rm H\,I}$. These estimates are summarized in Table 3. This shows evidence of an increase of b with increasing $N_{\rm H\,I}$ for the NLAs, at least for the weak absorbers with $\log N_{\rm H\,I} \lesssim 14.1$. The Spearman rank-order correlation test for the NLA sample shows a weak correlation between b and $N_{\rm H\,I}$, with $r = 0.12$ and $t = 0.15$. Since the sample is complete for the NLAs, the increase of b with increasing $N_{\rm H\,I}$ must be real. The large scatter is again expected if the H I lines are broadened as a result of different temperatures and turbulent velocities.

In Figure 6, we present the b-$N_{\rm H\,I}$ distribution for only the BLAs (*left panel*), which shows that b appears to decrease with increasing $N_{\rm H\,I}$: for $13.1 \lesssim \log N_{\rm H\,I} \lesssim 13.5$ (this range is highlighted in Fig. 6 by the vertical dotted lines), b is distributed between about 40 and 130 km s^{-1}; for $13.5 \lesssim \log N_{\rm H\,I} \lesssim 14.0$, b is mostly distributed between about 40 and 80 km s^{-1}; and for $\log N_{\rm H\,I} \gtrsim 14.0$, b is always lower than 50 km s^{-1}. This trend is also confirmed in the last two columns of Table 3 (note that in the [13.8, 14.1] interval there are only six systems, with three of them

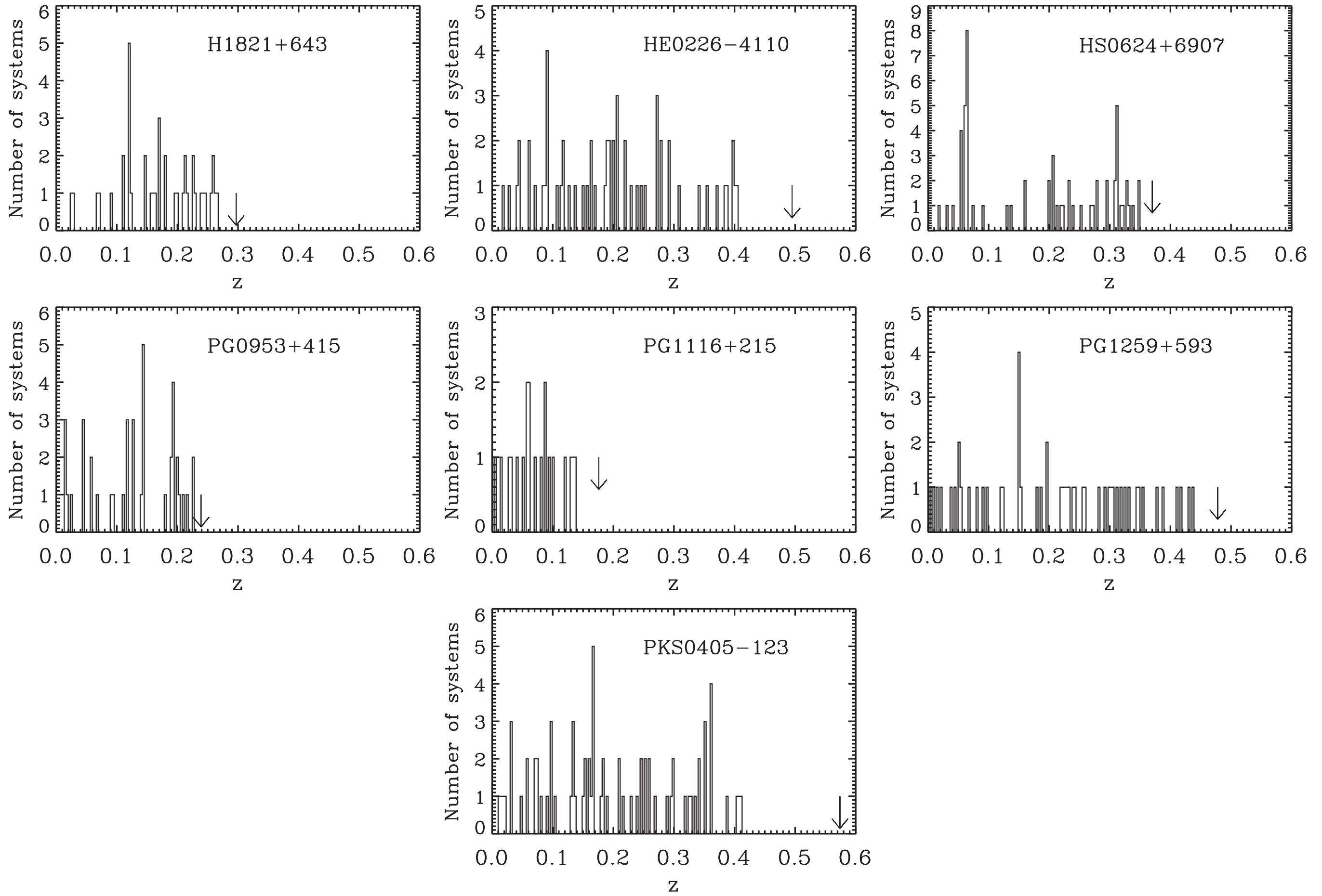

FIG. 3.—Distribution of the redshift of H I for each sight line with a redshift interval of $\Delta z = 0.0033$. The arrows show the redshifts of the QSOs. The wavelength coverage of the E140M mode of STIS limits Lyα measurements to $z \lesssim 0.42$.

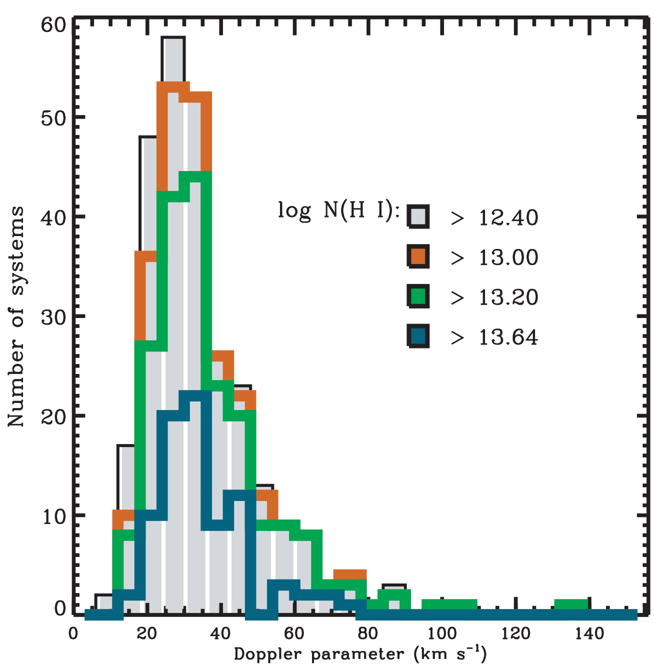

FIG. 4.—Distribution of the Doppler parameter of H I for a series of minimum log $N_{\rm H\,I}$ for $z \lesssim 0.4$ for the seven sight lines. Only data with less than 40% errors in b and $N_{\rm H\,I}$ are considered.

having $b > 60$ km s^{-1} and the other three having $b \sim 40$ km s^{-1}). The Spearman rank-order correlation for the BLA sample with log $N_{\rm H\,I} \geq 13.2$ confirms a negative correlation between b and $N_{\rm H\,I}$ ($r = -0.30$ and $t = 0.016$).

In the right panel of Figure 6, we show the recent simulation of BLAs undertaken by Richter et al. (2006a), in which artificial spectra were generated from the hydrodynamical simulation. Their numerical model was part of an earlier investigation of the O VI absorption arising in WHIM filaments (Fang & Bryan 2001), and they include collisional ionization and photoionization processes. The simulated sample presented in Figure 6 corresponds to their high-quality sample, which includes 321 BLAs with almost perfect Gaussian profiles (note that 58% of the sample has log $N_{\rm H\,I} \lesssim 13.2$). Since our observations are complete only to log $N_{\rm H\,I} \gtrsim 13.2$, it is not surprising that we are missing absorbers below this limit. It is, however, interesting to note that the simulation and observations have a similar trend: (1) most of the broadest absorbers are found at log $N_{\rm H\,I} \lesssim 13.5$, and (2) most of the strong absorbers (log $N_{\rm H\,I} \gtrsim 14$) have $b \lesssim 50$ km s^{-1} (although we note that in the simulation a few systems have b up to 65 km s^{-1}, and the simulation does not produce BLAs with log $N_{\rm H\,I} \gtrsim 14.4$). This is also in general agreement with the simulation of the WHIM produced by Davé et al. (2001), in which they show the WHIM fraction peaks for an overdensity $\rho/\bar{\rho}$ of $\sim$5–30. If equation (2) (see below) applies for the BLAs, the H I column density range 13.2–14.0 dex corresponds to $\rho/\bar{\rho} \sim$ 5–17, in general agreement with the hydrodynamical simulations of Davé et al. (2001), if the BLAs trace mostly the WHIM.

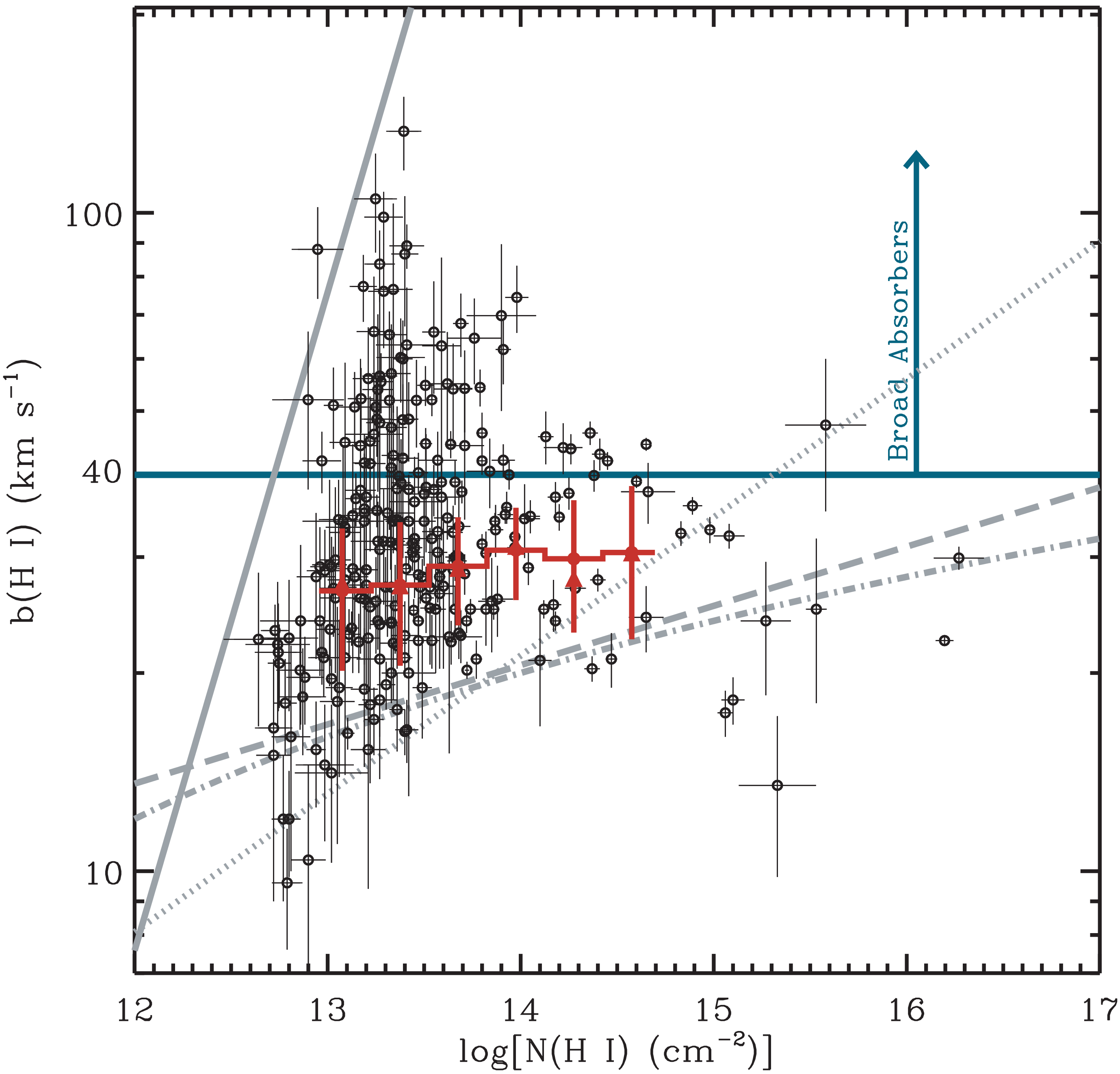

Fig. 5.—Line width vs. H I column density for the Lyα absorbers along the seven sight lines. Only data with less than 40% errors in b and $N_{\rm H\,I}$ are considered. The solid gray line shows b vs. $N_{\rm H\,I}$ for a Gaussian line shape with 10% central optical depth; absorption lines to the left of this line are not detectable. The dotted gray line shows the predicted minimum b-value from hydrodynamic cosmological simulations at low redshift (Davé et al. 1999). The dot-dashed and long-dashed lines show the fits to lower cutoff in the b-distribution of high-redshift systems (Kirkman & Tytler 1997; Kim et al. 2002b; see § 3.2 for more details). The red histogram and red symbols show the median b (*triangles*), the mean (*circles*), and the dispersion of b (*vertical bars*) in six bins of $N_{\rm H\,I}$ *only* for data with $b \leq 40$ km s^{-1} (see Table 3).

TABLE 3

Median, Mean, Dispersion of b at Low z in a Given Column Density Interval for the 7 QSO Sample

	$b > 0$ km s^{-1}		$b \leq 40$ km s^{-1}		$b > 40$ km s^{-1}	
Column Density Interval	Median	Mean $\pm\sigma$	Median	Mean $\pm\sigma$	Median	Mean $\pm\sigma$
[12.9, 13.2]	28.7	31.5 ± 13.9	27.2	26.7 ± 6.5	50.7	54.7 ± 16.6
[13.2, 13.5]	34.0	39.9 ± 21.7	27.0	27.2 ± 6.7	55.4	61.5 ± 21.1
[13.5, 13.8]	32.0	36.3 ± 12.9	28.7	29.1 ± 5.4	54.1	53.2 ± 8.4
[13.8, 14.1]	34.0	36.9 ± 14.1	31.0	30.7 ± 4.9	62.0	57.8 ± 15.7
[14.1, 14.4]	37.0	34.1 ± 9.1	27.7	29.8 ± 6.8	45.7	45.0 ± 1.2
[14.4, 14.7]	39.1	35.2 ± 8.9	30.3	30.5 ± 8.0	43.0	43.2 ± 1.3

Note.—Only data with $\sigma_b/b, \sigma_N/N \leq 0.4$ are included in the various samples.

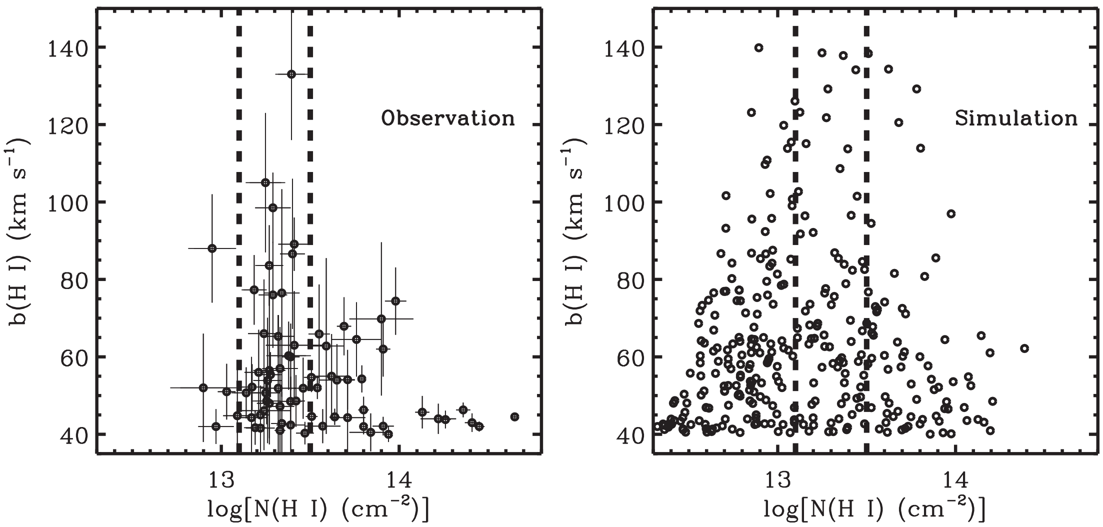

FIG. 6.—*Left*: Line width vs. H I column density for the BLAs ($b > 40$ km s^{-1}) along the seven sight lines. Only data with less than 40% errors in b and $N_{\rm H\,I}$ are considered. *Right*: Line width vs. H I column density for the high-quality sample of BLAs simulated by Richter et al. (2006a). The dashed vertical lines highlight the column density range [13.1, 13.5] dex where the broadest absorbers with $b > 80$ km s^{-1} are detected in the observational sample.

We note that the simulation of Richter et al. (2006a) generally produces larger b than currently observed; for systems with $\log N_{\rm H\,I} \gtrsim 13.2$, the median, mean, and standard deviation are 59, 69, and 31 km s^{-1} for the simulation, while they are 52, 57, and 18 km s^{-1} for the observations. The current S/N of the observed data limits the detection of the broader absorbers with $b > 80$ km s^{-1}, as discussed in § 2. We also note that the broader systems ($b > 80$ km s^{-1}) are likely to be more uncertain, especially since they are detected in the lowest column density range ($\log N_{\rm H\,I} \lesssim 13.4$).

Schaye et al. (1999) and others demonstrated that the temperature-density relation, which is well described by a power law $T = T_0(\rho/\bar{\rho})^{\gamma-1}$ (where $\bar{\rho}$ is the average density, $\rho/\bar{\rho}$ is the overdensity of the IGM), implies a lower envelope to the b-$N_{\rm H\,I}$ distribution. This lower envelope is not clearly observed in Figure 5. We further explore this by considering the numerical cosmological simulations of the low-redshift Lyα forest that predict that the temperature $T_4 = T/(10^4$ K) is a power law of the overdensity $\rho/\bar{\rho}$, with

$$T_4 \approx 0.5(\rho/\bar{\rho})^{0.6}, \tag{1}$$

for the coolest systems at any given density. The overdensity is connected to the H I column density through (Davé et al. 1999),

$$\frac{\rho}{\bar{\rho}} \approx 20\left(\frac{N_{\rm H\,I}}{10^{14}\ {\rm cm}^{-2}}\right)^{0.7} 10^{-0.4z}. \tag{2}$$

If we combine these two equations, we have

$$T_4 \approx 3\left(\frac{N_{\rm H\,I}}{10^{14}\ {\rm cm}^{-2}}\right)^{0.42} 10^{-0.24z}. \tag{3}$$

The pure thermal Doppler broadening for H is $b_{\rm th} = 0.129\sqrt{T}$, so for photoionized hydrogen absorbers we can write

$$b_{\rm th} \approx 22\left(\frac{N_{\rm H\,I}}{10^{14}\ {\rm cm}^{-2}}\right)^{0.21} 10^{-0.12z}\ {\rm km\ s}^{-1}. \tag{4}$$

This latter relation is shown in Figure 5 with the dotted line, where we set $z = 0.2$, which is about the mean and median z in our sample. Since the ρ-T fit to photoionized absorbers is for the coolest systems, this relation should provide a lower envelope to the b-$N_{\rm H\,I}$ distribution. The lower envelope to the observed b-$N_{\rm H\,I}$ distribution roughly agrees with the numerical simulations, at least as long as $\log N_{\rm H\,I} \lesssim 14.2$. But the low-redshift sample does not yet provide as sharp a lower envelope to the b-$N_{\rm H\,I}$ distribution as high-redshift samples do (see for example Kirkman & Tytler 1997; Kim et al. 2002a), because there are still too few systems at the completeness level. In Figure 5, we show with the dot-dashed line the relation $b_{\rm min} = 20 + 4\log[N_{\rm H\,I}/(10^{14}\ {\rm cm}^{-2})]$ km s^{-1} found by Kirkman & Tytler (1997) at $\bar{z} = 2.7$ and with the long-dashed line the relation $\log b_{\rm min} = 1.3 + 0.090\log[N_{\rm H\,I}/(10^{14}\ {\rm cm}^{-2})]$ km s^{-1} found by Kim et al. (2002b) at $\bar{z} = 2.1$ (smoothed power-law fit). These power laws provide a good approximation to the observed lower envelope of b at high redshift. At low redshift at $\log N_{\rm H\,I} \gtrsim 13.2$, a few absorbers lie below these fits, especially at $\log N_{\rm H\,I} \gtrsim 15$. For systems with $\log N_{\rm H\,I} \lesssim 15$, it is not clear if the lower b cutoff evolves with redshift.

Finally, following Davé & Tripp (2001), if we compare the median in the various intervals with $b \leq 40$ km s^{-1} (red curve in Fig. 5) and $b_{\rm th}$ defined in equation (4), we find that $b_{\rm th} \sim (0.6$–$0.7)b_{\rm obs}$ for a typical absorber with $\log N_{\rm H\,I} \lesssim 14.2$. Therefore, the contribution from thermal broadening is substantial for the low-redshift NLAs. However, if the some BLAs actually trace cool photoionized gas, the nonthermal broadening will be dominant in these absorbers.

3.3. *Lyα Line Density*

This sample provides the first opportunity to investigate the relative number of systems as a function of the Doppler parameter in the low-z IGM. In Table 4, we summarize $d\mathcal{N}/dz$ for each sight line and for the combined sample where our subsamples have either $b \leq 40$ or $b \leq 150$ km s^{-1}. For both b-samples, we choose three different column density ranges: (a) [13.2, 14.0] dex, (b) [13.2, 16.5] dex, and (c) [13.64, 16.5] dex. The lower limit of samples (a) and (b) corresponds to our threshold of completeness. The largest observed column density in our sample is about $10^{16.5}$ cm^{-2}. Hence, sample (b) corresponds to the combined

TABLE 4
Lyα Line Density

Sight Line	$b \le 40$ km s^{-1} $\mathcal{N}_{\rm H\,I}$	$d\mathcal{N}_{\rm H\,I}/dz$	$b \le 150$ km s^{-1} $\mathcal{N}_{\rm H\,I}$	$d\mathcal{N}_{\rm H\,I}/dz$
(a) $13.2 \le \log N_{\rm H\,I} \le 14.0$				
H1821+643	7	29 ± 11	12	50 ± 15
HE 0226−4110	16	40 ± 10	22	55 ± 12
HS 0624+6907	22	67 ± 14	31	94 ± 17
PG 0953+415	13	64 ± 18	17	84 ± 20
PG 1116+215	7	56 ± 21	12	95 ± 28
PG 1259+593	24	68 ± 14	35	99 ± 17
PKS 0405−123	21	51 ± 11	35	85 ± 14
Mean		54 ± 5 (15)		80 ± 6 (20)
(b) $13.2 \le \log N_{\rm H\,I} \le 16.5$				
H1821+643	9	38 ± 13	15	63 ± 16
HE 0226−4110	21	52 ± 11	31	77 ± 14
HS 0624+6907	25	76 ± 15	35	106 ± 18
PG 0953+415	14	69 ± 19	18	89 ± 21
PG 1116+215	8	64 ± 23	13	103 ± 29
PG 1259+593	30	85 ± 15	43	121 ± 19
PKS 0405−123	33	80 ± 14	47	114 ± 17
Mean		66 ± 6 (17)		96 ± 7 (21)
(c) $13.64 \le \log N_{\rm H\,I} \le 16.5$				
H1821+643	6	25 ± 10	7	29 ± 11
HE 0226−4110	10	25 ± 8	16	40 ± 10
HS 0624+6907	10	30 ± 10	13	40 ± 11
PG 0953+415	6	30 ± 12	6	30 ± 11
PG 1116+215	2	16 ± 11	2	16 ± 11
PG 1259+593	12	34 ± 10	18	51 ± 13
PKS 0405−123	16	39 ± 10	21	51 ± 12
Mean		28 ± 4 (8)		37 ± 4 (13)

Notes.—Only data with $\sigma_b/b, \sigma_N/N \le 0.4$ are included in the various samples. Errors are from Poisson statistics. The number in parentheses in the row showing the mean corresponds to the standard deviation around the mean for the different lines of sight.

sample with $W \gtrsim 90$ mÅ, while sample (a) only covers the weaker Lyα lines, which may evolve differently than the stronger lines, since the weaker lines may arise from tenuous gas in the IGM, while the stronger lines may mostly trace the gas in the outskirts of galaxies. The threshold of sample (c) was chosen to be comparable to the equivalent width threshold of 0.24 Å from the *HST* QSO absorption-line key project (Weymann et al. 1998). The last rows of the subtables in Table 7, below, show the mean $d\mathcal{N}/dz$ for the seven sight lines. We considered only absorbers with $\sigma_b/b, \sigma_N/N \le 0.4$. Note that the average values would have increased only by ~5% if we did not apply this cutoff.

The average value of $d\mathcal{N}/dz$ in sample (c) ($W \gtrsim 0.24$ Å) of 28 ± 4 for $b \le 40$ km s^{-1} is slightly smaller than the estimates of Weymann et al. (1998) at $\log(1+z) < 0.15$ and Impey et al. (1999) at $0 < z < 0.22$, because the broader absorbers and uncertain absorbers are not included in our sample. Indeed, the estimates of Weymann et al. (1998) and Impey et al. (1999) appear intermediate between our two b samples. Penton et al. (2004) found $d\mathcal{N}/dz = 25 \pm (4, 5)$ for a sample with $z < 0.069$, which overlaps with our estimate within the 1 σ dispersion, which implies little or no evolution of $d\mathcal{N}/dz$ at $z \lesssim 0.4$ for the strong H I absorbers. For $b \le 150$ km s^{-1}, the value of $d\mathcal{N}/dz$ is about 1.3 times larger than for the NLAs. We find that the broad Lyα lines with $40 < b \le 150$ km s^{-1} have $d\mathcal{N}({\rm BLA})/dz \approx 9$, implying that for the stronger lines of the Lyα forest, the number of BLAs per unit redshift may be important.

Comparison of samples (a) and (b) shows that the weak systems are far more frequent than the strong systems. For these samples, we note that $d\mathcal{N}/dz$ is systematically smaller toward H1821+643 and HE 0226−4110 than toward the other sight lines, for both b subsamples.Along the PG 1116+215 and PKS 0405−123 sight lines, $d\mathcal{N}/dz$ is intermediate for the NLAs. The three other lines of sight have similar $d\mathcal{N}/dz$. These trends do not appear related to the S/N of the data, since the S/N is the highest toward H1821+643 and comparatively low for HE 0226−4110. The redshift paths do not seem to explain all the differences. For example, while the redshift paths are comparable between HE 0226−4110 and PG 1259+593, Δz is significantly smaller toward PG 1116+215. Toward the sight lines that cover small and large redshift paths, $d\mathcal{N}/dz$ is very similar for either column density range, implying no redshift evolution of $d\mathcal{N}/dz$ between $z > 0$ and $z \lesssim 0.4$. Therefore, some of the observed variation in $d\mathcal{N}/dz$ must be cosmic variance between sight lines.

We explore the effect of the S/N on the $d\mathcal{N}({\rm BLA})/dz$ estimate in Table 5 by considering data with $\sigma_b/b, \sigma_N/N \le 0.4$, 0.3, and 0.2. As expected, the spectra with the highest S/N are less affected by these cutoffs than the spectra with the lowest S/N. Decreasing the error thresholds has an effect mostly on the weak systems ($\log N_{\rm H\,I} \lesssim 13.40$). Toward PG 0953+415, the four BLAs have $13.2 < \log N_{\rm H\,I} \le 13.40$ and $0.23 \le \sigma_b/b \le 0.30$, which explains why there is no BLA at the threshold $\sigma_b/b \le 0.2$. Although the HS 0624+6207 spectrum has several weak BLAs,

TABLE 5
Effect of the Signal-to-Noise Ratio on the Broad Lyα Density Estimate

Sight Line	S/N	$d\mathcal{N}_{\rm H\,I}/dz$ $\sigma_b/b, \sigma_N/N \le 0.4$	$\sigma_b/b, \sigma_N/N \le 0.3$	$\sigma_b/b, \sigma_N/N \le 0.2$
H1821+643	15–20	25 ± 10	25 ± 10	25 ± 10
HE 0226−4110	5–11	25 ± 8	20 ± 7	18 ± 7
HS 0624+6907	8–12	30 ± 10	30 ± 10	30 ± 10
PG 0953+415	7–11	20 ± 10	15 ± 9	0
PG 1116+215	10–15	40 ± 18	40 ± 18	32 ± 16
PG 1259+593	9–17	37 ± 10	34 ± 10	25 ± 9
PKS 0405−123	5–10	34 ± 9	24 ± 8	14 ± 6
Mean		30 ± 4(7)	27 ± 4(8)	21 ± 3(11)

Notes.—S/N is measured per resolution element. Sample with $40 < b \le 150$ km s^{-1} and $13.2 \le \log N_{\rm H\,I} \le 16.5$. Errors are from Poisson statistics. The number in parentheses in the row showing the mean corresponds to the standard deviation around the mean for the different lines of sight.

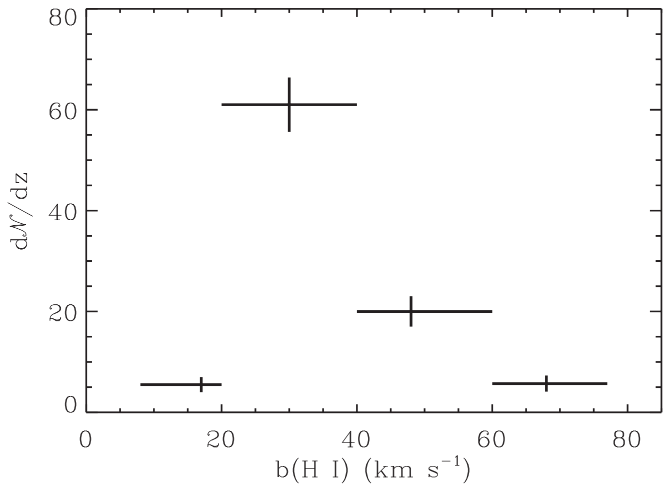

FIG. 7.—Mean number density per unit redshift with Poissonian errors (*vertical bars*) in four intervals of b ([0, 20], [20, 40], [40, 60], and [60, 80] km s^{-1}) using data with $\sigma_b/b, \sigma_N/N \leq 0.4$ and $\log N_{\rm H\,I} \geq 13.2$. The mean number density is shown at the mean b-value of each b-interval sample. The horizontal bars show the b-intervals delimited by the minimum and maximum b-values of each b-interval sample.

only if $\sigma_b/b, \sigma_N/N < 0.15$ is applied do we observe a significant drop in $d\mathcal{N}(\mathrm{BLA})/dz$, by a factor 2.5. On average, there is a decrease in $d\mathcal{N}(\mathrm{BLA})/dz$ by a factor ∼1.4 between the cutoff at 0.4 and 0.2. If only BLAs with $40 < b \leq 100$ km s^{-1} are considered, $d\mathcal{N}(\mathrm{BLA})/dz = 28$, 25, and 20 for $\sigma_b/b, \sigma_N/N \leq 0.4$, 0.3, and 0.2, respectively. These estimates are in agreement with those of Richter et al. (2006b; see also § 4.2). The BLA density is about 2 times smaller than $d\mathcal{N}(\mathrm{NLA})/dz$ for samples (a) and (b).

Finally, we summarize in Figure 7 the frequency of the Lyα absorbers with various b-values in the low-redshift universe. In this figure, $d\mathcal{N}/dz$ represents the mean of the number density of H I absorbers obtained toward each line of sight in four intervals of b ([0, 20], [20, 40], [40, 60], and [60, 80] km s^{-1}), using data with $\sigma_b/b, \sigma_N/N \leq 0.4$ and $\log N_{\rm H\,I} \geq 13.2$. The vertical error bars assume Poissonian errors. The mean $d\mathcal{N}/dz$ is shown at the mean b-value of each b-interval sample. The horizontal bars show the b-intervals delimited by the minimum and maximum b-values of each b-interval sample. The NLAs are mostly found between 20 and 40 km s^{-1}. Very narrow Lyα absorbers with $b < 20$ km s^{-1} are rare, and we note that in the [0, 20] km s^{-1} interval, most of the absorbers have $b \gtrsim 15$ km s^{-1}. The paucity of very narrow absorbers with $\log N_{\rm H\,I} \geq 13.2$ is real since the resolution of STIS E140M ($b_{\rm inst} \sim 4$ km s^{-1}) allows us to fully resolve absorbers with $b \gtrsim 5$ km s^{-1}. The broad absorbers are more frequent in the $b = [40, 60]$ km s^{-1} range; there are about 3.5 times more absorbers in [40, 60] km s^{-1} interval than in the $b = [60, 80]$ km s^{-1} interval. Lyα absorbers are therefore more frequent for low column densities [$\log N_{\rm H\,I} \lesssim 14$] and for b-values between 20 and 40 km s^{-1}.

4. EVOLUTION OF b

4.1. *Higher Redshift Samples*

Recently, the analysis of the Lyα absorbers in the redshift range $0.5 < z < 2.0$ from Janknecht et al. (2006) has become available at the Centre de Données de Strasbourg (CDS). Their data that sample the mid-z IGM at $0.5 < z \lesssim 1.5$ were obtained with *HST* STIS E230M: PG 1634+706 ($z = 0.534$–1.295), PKS 0232−04 ($z = 0.876$–1.419), PG 1630+377 ($z = 0.875$–1.451), PG 0117+213 ($z = 0.875$–1.475), HE 0515−4414 ($z = 0.874$–1.475), and HS 0747+4259 ($z = 0.760$–1.443). The redshifts in parentheses indicate the redshift interval probed by the observations. The spectral resolution of E230M data ($R \sim 30{,}000$) is lower than that of the low-z sample obtained with the E140M grating ($R \sim 44{,}000$). The S/N of the mid-z sample is comparable to the lowest S/N of the low-z sample, except for PG 1634+706, which has a S/N per resolution element of 5–40. The high-redshift sample ($z > 1.5$) consists of data obtained with the Very Large Telescope (VLT) Ultraviolet Visual Echelle Spectrograph (UVES; $R \sim 40{,}000$): HE 0515−4414 ($z = 1.515$–1.682), HE 0141−3932 ($z = 1.518$–1.784), HE 2225−2258 ($z = 1.515$–1.861), and HE 0429−4901 ($z = 1.662$–1.910). The S/N is typically higher than 30–40, except for HE 0429−4901, which is about 15. The spectrum of HS 0747+4259 ($z = 1.562$–1.866) was also obtained with the Keck High Resolution Echelle Spectrometer (HIRES; $R \sim 50{,}000$) with a S/N in the range of 6–24.

For the high-redshift sample, we also consider the spectra of QSOs at $z > 1.5$ presented by Kim et al. (2002a). Their profile-fitting results are available at the CDS. These data were obtained with the VLT UVES at resolution of $R \sim 45{,}000$ and typical S/N $\simeq$ 40–50. The QSOs considered are HE 0515−4414 ($z =$ 1.53–1.69), Q1101−264 ($z = 1.66$–2.08), J2233−606 ($z = 1.80$–2.20), HE 1122−1648 ($z = 1.88$–2.37), HE 2217−2818 ($z =$ 1.89–2.37), HE 1347−2457 ($z = 2.09$–2.57), Q0302−003 ($z =$ 2.96–3.24), Q0055−269 ($z = 2.99$–3.60). Note that the HE 0515−4414 VLT spectrum in Janknecht et al. (2006) has a different wavelength coverage and exposure time than the HE 0515−4414 VLT spectrum presented by Kim et al. (2002a). We finally consider the H I parameters measured toward HS 1946+7658 ($z = 2.43$–3.05) by Kirkman & Tytler (1997). The spectrum of HS 1946+7658 was obtained with Keck HIRES. The S/N per resolution element varies from about 30 to 200 and the spectral resolution is similar to UVES. The spectral resolution of the high-redshift sample is similar to the low-redshift sample, but the S/N is generally much higher in the $z > 1.5$ sample than in the low- or mid-z samples.

4.2. *Conditions for Comparing Various Samples*

The definition of a BLA that was followed in recent papers presented by our group is an absorber that can be fitted with a single Gaussian component with $b > 40$ km s^{-1} and for which the reduced χ^2 does not improve statistically by adding more components to the model. Low-S/N data can have, however, treacherous effects that can mask a BLA or confuse narrow multiabsorbers with a BLA (see Fig. 2 in Richter et al. 2006b). To overcome the effects of noise, the sample of BLAs defined by Richter et al. (2006b) has to also satisfy the following rules: (1) the line does not show any asymmetry, (2) the line is not blended, (3) there is no evidence of multiple components in the profile; and (4) the S/N must be high enough (i.e., $\log (N_{\rm H\,I}/b) \gtrsim \log [3 \times 10^{12}/(\mathrm{S/N})] \gtrsim 11.3$, where $N_{\rm H\,I}$ and b are in cm^{-2} and km s^{-1}, respectively). For the low-redshift sample presented here, the BLAs strictly follow criteria (4) when the condition $\sigma_b/b, \sigma_N/N \leq 0.4$ is set. Following these rules, Richter et al. (2006b) found $d\mathcal{N}(\mathrm{BLA})/dz = 22 \pm 5$ for their secure detections (53 for the entire candidate sample). Within 1 σ, our BLA number density estimate overlaps with the result of Richter et al. (2006b) when the cutoff $\sigma_b/b, \sigma_N/N \leq 0.4$ is applied to our sample. Therefore, this shows that by applying an error cutoff without scrutinizing each profile for the conditions listed above, we find a similar average $d\mathcal{N}(\mathrm{BLA})/dz$. This is crucial, because for a comparison with other samples at higher z, we cannot examine each absorber individually. For the sample presented by Janknecht et al. (2006), no spectra or fits are shown. Kim et al. (2002a) and Kirkman & Tytler (1997) present their spectra and fits, but over wavelength ranges that were too broad to study the conditions listed above in detail. Furthermore, as z increases, absorbers are more often blended due to the higher redshift line density, so we cannot reject the blended systems, or we would introduce a strong bias in the comparison. At high, mid, and low redshift, the χ^2 of the profile fit governs the number of components allowed in the model of an absorber; therefore, a similar methodology was applied in each sample, allowing a direct comparison of the various measurements. We apply the same cutoff $\sigma_b/b, \sigma_N/N \leq 0.4$ to the $z > 0.5$ redshift samples to remove the uncertain profile fit results in a similar manner in each sample. Such a cutoff, however, introduces a systematic effect; more BLAs will be rejected in low-S/N spectra (low- and some mid-z data) than in high-S/N spectra (high-z data). But such systematics should underestimate the number of BLAs in low-S/N data, and therefore this should strengthen the differences observed at low z compared to the higher z samples.

For our comparison, we also consider only absorbers with $\log N_{\rm H\,I} \geq 13.2$, the completeness level of the low-redshift sample, which also corresponds to about the completeness of the lowest S/N spectra of the mid-z sample. If the S/N of the high-redshift spectra is solely considered, absorbers with $\log N_{\rm H\,I} \geq 13.2$ would be far above the completeness level of the high-redshift sample, which is $\log N_{\rm H\,I} \gtrsim 12.5$ for the data presented by Kim et al. (2002a) and Kirkman & Tytler (1997). However, line blending and blanketing reduce the completeness threshold, especially at $z \gtrsim 2.5$ (Kirkman & Tytler 1997; Lu et al. 1996). At $z \sim 4$, Lu et al. (1996) show, using simulated spectra, that line blanketing was not important as long as $\log N_{\rm H\,I} \gtrsim 13.5$, while at $z \sim 2.7$, Kirkman & Tytler (1997) show, following a similar methodology, that their sample is likely to be complete at $\log N_{\rm H\,I} \gtrsim 12.8$–13.0. Since broad and shallow absorbers are more uncertain, considering only absorbers with $\log N_{\rm H\,I} \geq 13.2$ also reduces the problem of creating a higher proportion of wide lines than is really present in the intrinsic distribution.

For our comparison, we only consider BLAs with $40 < b \leq 100$ km s^{-1}. The choice of $b \leq 100$ km s^{-1} reduces the incompleteness at the high-b end of the low-redshift sample. Furthermore, at $z \sim 4$ (which is at higher redshift than any absorbers considered here), Lu et al. (1996) argue that absorbers with $b > 100$ km s^{-1} are caused essentially by heavily blended forest lines, since they are systematically found in the high line density region of the spectrum. This effect should diminish greatly as z decreases. At $z \sim 2.7$, Kirkman & Tytler (1997) have produced simulated spectra to better understand the intrinsic properties of their observational data. They observe a tail at high b in both the simulated and observed b-distributions. In the simulated spectra, the tail at $b > 80$ km s^{-1} is only due to line blending, because their simulation did not allow such broad lines. They find more lines at $b > 80$ km s^{-1} in the observed distribution (3.6% compared to 0.5% in the simulated spectra), suggesting that many of these absorbers could be intrinsically broad. Refined simulations, so that simulated observations match exactly the real observations, would be needed to be entirely conclusive on this point (Kirkman & Tytler 1997). Yet, at high z, if BLAs with $b > 80$ km s^{-1} that are in fact blended narrow lines were frequent, this effect should be more important as z increases. We show that this effect, if present, is not statistically significant (see §§ 4.3 and 4.4). By considering only absorbers with $40 < b \leq 100$ km s^{-1}, $\log N_{\rm H\,I} \geq 13.2$, and $\sigma_b/b, \sigma_N/N \leq 0.4$, we significantly reduce the risk of including spurious broad absorbers. We also note that, in any samples considered, the majority of BLAs are actually found in the b-range $40 < b \leq 60$ km s^{-1}, not in the b-range $b > 80$ km s^{-1}.

In Figure 8, we show the b-$N_{\rm H\,I}$ distribution for three redshift intervals, $z < 0.5$ (*top panel*), $0.5 < z < 1.5$ (*middle panel*), and $1.5 < z \lesssim 3.6$ (*bottom panel*). Only absorbers that satisfy the conditions $0 < b \leq 100$ km s^{-1}, $\log N_{\rm H\,I} \geq 13.2$, and $\sigma_b/b, \sigma_N/N \leq 0.4$ are shown in the figure. At $z > 0.5$, there are many weak systems with $b < 40$ km s^{-1}, which darkens part of the middle and bottom panels. At $z < 0.5$, there are very few absorbers with $b \gtrsim 40$ km s^{-1} and $\log N_{\rm H\,I} > 14$, and none of them have $b > 50$ km s^{-1}. This contrasts remarkably with what is observed at higher redshifts: many absorbers at $z > 0.5$ have $b > 40$ km s^{-1} and $\log N_{\rm H\,I} \geq 14.0$. This effect must be due to strong, saturated Lyα lines for which the errors for b and $\log N_{\rm H\,I}$ are far too optimistic. At $z < 0.5$, saturation can be dealt with because higher Lyman series lines are systematically used in the profile fitting, reducing the possibility of nonuniqueness in the profile-fitting solution and of finding unrealistic large b-values for strong lines. At $z > 0.5$, Lyα is generally the only transition available, although we note Kim et al. (2002a) analyzed the Lyβ forest at $z < 2.5$ with a small sample, and their results suggested that line blending and saturation are not an important issue. Yet, Figure 8 shows a system with $b = 97.0 \pm 3.8$ km s^{-1} and $\log N_{\rm H\,I} = 16.44 \pm 0.14$. This absorber is observed in the spectrum of J2233−606 at $z = 1.869$, and the parameters that are presented here were estimated by Kim et al. (2002a). The spectrum of J2233−606 is shown in Cristiani & D'Odorico (2000), and at the wavelength corresponding to this absorber, there is a strong, saturated line that Kim et al. (2002a) model with a single component. D'Odorico & Petitjean (2001) actually found that this absorber has ∼11–16 components using higher Lyman series lines and metal lines. While this example is extreme, most of the absorbers with $\log N_{\rm H\,I} > 14$ and $b > 40$ km s^{-1} are likely to be strong saturated Lyα lines at $z > 0.5$. Figure 1 in Kirkman & Tytler (1997), which shows the whole HS 1946+7658 spectrum with the values of $\log N_{\rm H\,I}$ and b, corroborates this conclusion. The strong, saturated Lyα lines are unlikely to probe a single broad line, but are likely composed of several unresolved components. Therefore, for our comparison, we consider absorbers with $13.2 \leq \log N_{\rm H\,I} \leq 14.0$. This sample is summarized in the right-hand side of Figure 8.

As we have just illustrated, the Voigt profile-fitting method adopted for deriving z, b, and $N_{\rm H\,I}$ may not be unique, especially for highly blended regions, strong lines, and low-S/N spectra. We believe that some of this effect is reduced by considering absorbers with $13.2 \leq \log N_{\rm H\,I} \leq 14.0$, $b < 100$ km s^{-1}, and $\sigma_b/b, \sigma_N/N \leq 0.4$. At low z, line blending and strong lines are not a major issue, because often higher Lyman series lines can be used. Futhermore, several persons analyzed these data independently, and other methods (curve-of-growth and/or optical depth method) were also used for the low-z sample, yielding consistent results (see the references given in Table 1), although the Appendix highlights some differences between various groups. Even in this latter case, there is roughly a 1 σ consistency between the various results for absorbers with $13.2 \leq \log N_{\rm H\,I} \leq 14.0$. At $z \sim 2.7$, Kirkman & Tytler (1997) show that profile fitting may not provide a unique solution even in very high S/N data. Yet, their comparison with simulated spectra show that the intrinsic distribution of b is very similar to the observed b-distribution. Therefore, in a statistical sense, the observed b-distribution at high z can be used for our comparison. We also note that three different research groups have worked on the absorbers at $z \gtrsim 1.5$ presented here, with the spectra obtained from different telescopes with different S/N, and we did not find any major differences between their results, at least within the conditions listed above.

Continuum placement may also be a problem for finding or defining a BLA. At low z, BLAs may be confused with continuum undulations. With our constraints, most of these ill-defined BLAs are rejected (see also Richter et al. 2006b). We believe that

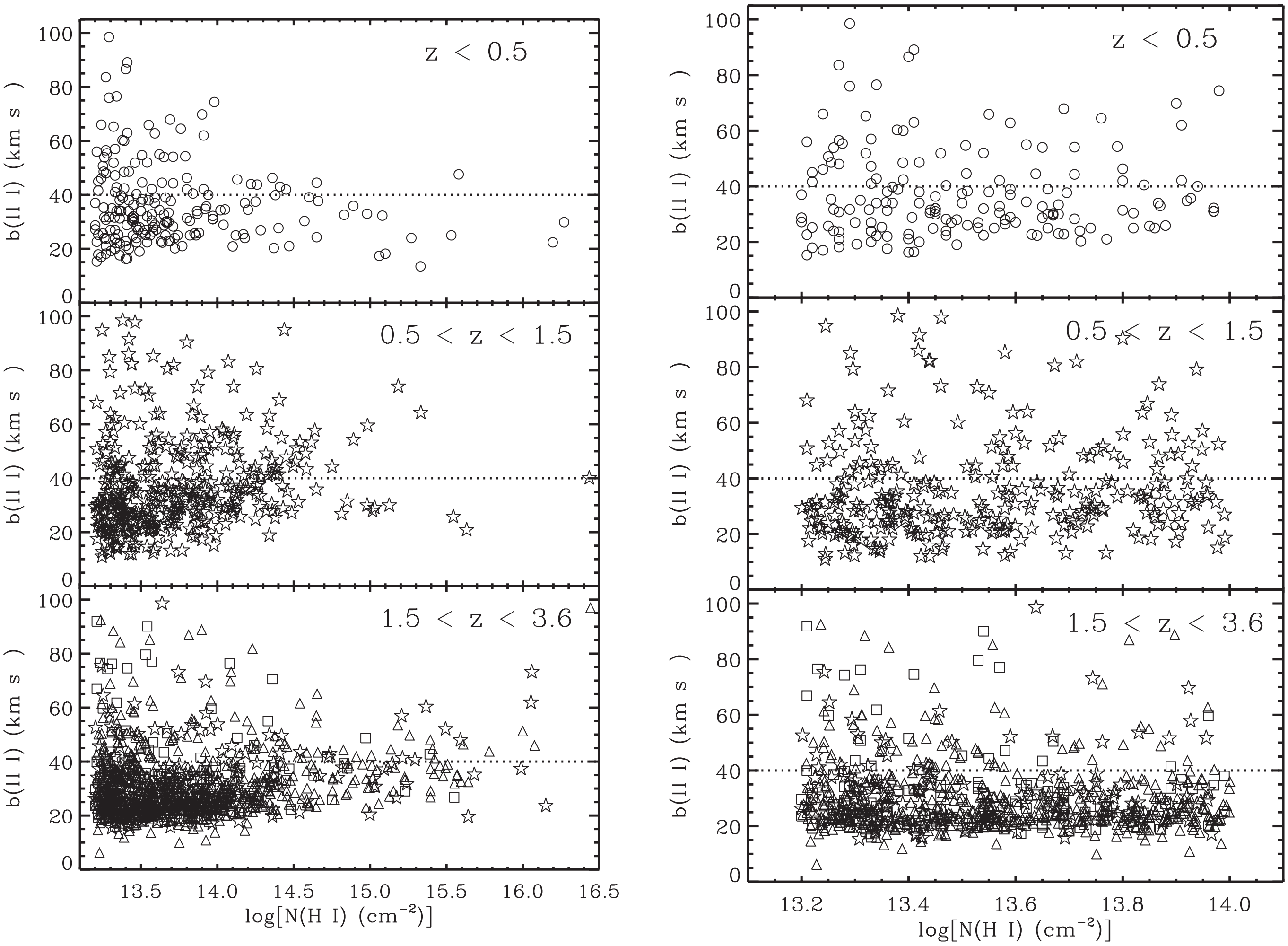

Fig. 8.—*Left panels*: Line width vs. H I column density for the Lyα absorbers for $13.2 \leq \log N_{\rm H\,I} \leq 16.5$ and $0 < b \leq 100$ km s^{-1} in different redshift intervals, indicated in the upper right corner. Only data with less than 40% errors in b and $N_{\rm H\,I}$ are considered. The symbols have the following meaning: circles were estimated from the low-redshift sample (see Table 1 for the references), stars are from the sample of Janknecht et al. (2006), triangles are from the sample of Kim et al. (2002a), and squares are from the sample of Kirkman & Tytler (1997). *Right panel*: Same as the left-hand side, but only for absorbers with $13.2 \leq \log N_{\rm H\,I} \leq 14.0$.

this conclusion should apply to the mid-z sample, but since Janknecht et al. (2006) did not present any of the spectra they analyze, we treat this sample with more caution (see also below). At $z > 1.5$, the continuum is more difficult because each order must be fitted with a high-order Legendre polynomial, and during the Voigt profile-fitting process, the continuum level is often adjusted to give an optimum fit between the data and the calculated Voigt model. Furthermore, as z increases, the continuum placement becomes more difficult because the line density increases, and therefore the line blending and blanketing effects increase. High-order polynomials and adjusted continua can therefore mask broad and shallow BLAs. However, such effects may be counterbalanced by a possible spurious increase of BLAs caused by the same line blending and blanketing effects (see above). The high S/N of the data at high redshifts and considering only the absorbers with $13.2 \leq \log N_{\rm H\,I} \leq 14.0$ and $b \leq 100$ km s^{-1} greatly reduce the risk of losing many BLAs because of the line blending and blanketing at high z. The problem of not finding BLAs is potentially more important in the highest z spectra, but we do not notice significant differences between $z \sim 2$ and $z > 3$. We also note above that simulated spectra show that line blanketing was not important at $\log N_{\rm H\,I} \gtrsim 13.2$. Therefore, for the samples considered here using the limits $\log N_{\rm H\,I} \geq 13.2$ and $b \leq 100$ km s^{-1}, they must almost be complete. Ultimately, one would like to produce simulated spectra of various values of z with realistic inputs to fully consider the impacts of S/N, continuum placement, and line blending and blanketing on finding BLAs and deriving their intrinsic properties.

The redshift range $z = 0.5$–1.5 is more problematic than the other redshift ranges because most of the data have low S/N, all have lower resolution than the higher or lower redshift spectra, and no spectra or fits were presented by Janknecht et al. (2006), making it more difficult to assess some of the issues discussed above. Lyβ lines are only available for about half the wavelength coverage of this redshift range, and lower spectral resolution and S/N of these data further worsen the problems of saturation and nonuniqueness in the profile-fitting results. Setting the conditions $0 < b \leq 100$ km s^{-1}, $13.2 \leq \log N_{\rm H\,I} \leq 14.0$, and $\sigma_b/b, \sigma_N/N \leq 0.4$ make this sample stronger, but we nonetheless treat the results from this sample with caution. We consider two subsamples for the estimate of the redshift density based on the Janknecht et al. (2006) sample (see § 4.4): one with all their data and one with only their highest S/N data (i.e., PG 1634+706, HE 0515−4144, HE 0141−3932, HE 2225−2258). Among the high-S/N data in the mid-z sample are E230M spectra of PG 1634+706 and HE 0515−4144.

For the reasons aforementioned, with the conditions $0 < b \leq 100$ km s^{-1}, $13.2 \leq \log N_{\rm H\,I} \leq 14.0$, and $\sigma_b/b, \sigma_N/N \leq 0.4$, we

TABLE 6
Evolution of b

Parameter	$z < 0.5$ (This paper)	$0.5 < z < 1.0$ (J06)	$1.0 < z < 1.5$ (J06)	$1.5 < z < 2.0$ (J06)	$1.5 < z < 3.6$ (K02)	$2.4 < z < 3.1$ (KT97)
			$0 < b \leq 100$ km s^{-1}			
b median ($m_{\rm tot}$)	30.5 (336)	27.9 (263)	28.3 (588)	28.0 (450)	24.8 (2305)	27.1 (452)
b mean $\pm\sigma$	34.0 ± 16.9	32.9 ± 17.8	31.8 ± 17.0	31.4 ± 14.5	27.2 ± 13.5	31.2 ± 16.2
$m(b > 40)/m_{\rm tot}$	0.277	0.274	0.240	0.204	0.131	0.210
			$0 < b \leq 100$ km s^{-1} and $0 < (\sigma_b/b, \sigma_N/N) \leq 0.4$ and $13.2 \leq \log N_{\rm H\,I} \leq 14.0$			
b median ($m_{\rm tot}$)	32.7 (162)	31.5 (82)	30.8 (209)	28.2 (154)	25.5 (509)	27.1 (123)
b mean $\pm\sigma$	37.4 ± 16.1	36.0 ± 18.3	35.5 ± 17.3	31.7 ± 12.9	29.2 ± 11.9	32.5 ± 16.0
$m(b > 40)/m_{\rm tot}$	0.321	0.317	0.272	0.169	0.132	0.179

Notes.—Median and mean values of b are listed for the different redshift intervals for the entire samples with $0 < b \leq 100$ km s^{-1} and the higher quality samples restricted to absorbers with $13.2 \leq \log N_{\rm H\,I} \leq 14.0$; $m_{\rm tot}$ is the total number of absorbers in the sample; and $m(b > 40)$ is the total number of absorbers with $40 < b \leq 100$ km s^{-1} in the sample. The values of σ listed are the standard deviation around the mean. Source of profile-fitting measurements: J06=Janknecht et al. (2006); K02=Kim et al. (2002a); KT97=Kirkman & Tytler (1997).

greatly reduce some pitfalls in comparing data analyzed by various groups, with different S/N, obtained with various instruments, with different line blending issues. A BLA is therefore defined here as an absorber that is fitted with a single Gaussian for which the χ^2 does not drop significantly by adding more components (this condition was adopted by the various groups who analyzed the data used here) and that has $40 \leq b \leq 100$ km s^{-1}, $13.2 \leq \log N_{\rm H\,I} \leq 14.0$, and $\sigma_b/b, \sigma_N/N \leq 0.4$. We believe that we are statistically comparing the intrinsic properties of the broadening of H I absorbers, although we note that simulated spectra probing various values of z with realistic inputs may be the only way to fully understand some of the effects discussed above and how these effects balance each other at various z.

4.3. *Comparison of the Distributions of b at Low and Higher z*

Table 6 summarizes the b-value median, mean, dispersion, and fraction of BLAs (i.e., systems with $40 < b \leq 100$ km s^{-1}). In this table, we consider two subsamples with $0 < b \leq 100$ km s^{-1}: (1) the entire sample and (2) the higher quality sample with $13.2 \leq \log N_{\rm H\,I} \leq 14.0$ and errors in b and $N_{\rm H\,I}$ less than 40%. We note that the number of systems in each sample is roughly similar, except for the Kim et al. (2002a) sample, which is noticeably larger, and the $0.5 < z < 1.0$ sample, which is somewhat smaller. In sample (1) there appears to be an increase in the median, mean, and the fraction of BLAs as z decreases. The same trend is observed in sample (2), but the differences are better revealed, where the median and mean are always larger by 15%–30% in the low-redshift sample ($z < 0.5$) than in the high-redshift sample ($z > 1.5$). For sample (2), the fraction of BLAs at $z \lesssim 0.4$ is 1.9–2.4 times larger than the fraction of BLAs at $z \gtrsim 1.5$. Therefore, b is larger on average at $z \lesssim 1.0$ than at $z \gtrsim 1.5$, and the fraction of BLAs is larger at $z < 1.5$ than at $z > 1.5$.

In Figures 9–12 we compare the distributions of b(H I). In all comparisons we restrict the observations to the higher quality measurements with less than 40% errors in b and $N_{\rm H\,I}$.

In Figure 9, we compare the normalized number distribution of b(H I) for the low-redshift sample with the normalized number distribution of b(H I) for the Janknecht et al. (2006) sample, which is subdivided into three z subsamples. The distributions peak at about $b \sim 20$–30 km s^{-1}. Each distribution shows a tail at higher b. The tail in the $1.5 < z < 2.0$ distribution is always weaker than in the lower z-interval distributions, especially for $40 < b < 55$ km s^{-1}. The tail in the $0.5 < z < 1.0$ distribution is generally stronger than any other z-interval distribution presented in this figure, which is possibly due to a combination of blending effects, low-S/N spectra, and lower resolution spectra in the redshift range $0.5 < z < 1.0$. We note that data probing the redshift ranges $0.5 < z < 1.0$ and $1.0 < z < 1.5$ were obtained with the STIS E230M grating, but the sensitivity of E230M is lower for Lyα in the redshift range $0.5 \lesssim z \lesssim 0.9$ than $0.9 \lesssim z \lesssim 1.4$. A Kolmogorov-Smirnov test does not reveal a significant difference between the samples $z < 0.5$ and $0.5 < z < 1.5$ (the maximum deviation between the two cumulative distributions is $D = 0.118$ with a level of significance $P = 0.104$), but suggests a difference between the samples with $z < 0.5$ and $1.5 < z < 2.0$. Therefore, BLAs appear more frequent at $z < 1.5$ than at $z > 1.5$.

In Figure 10, we compare the normalized number distribution of b(H I) for the low-redshift sample with the normalized number

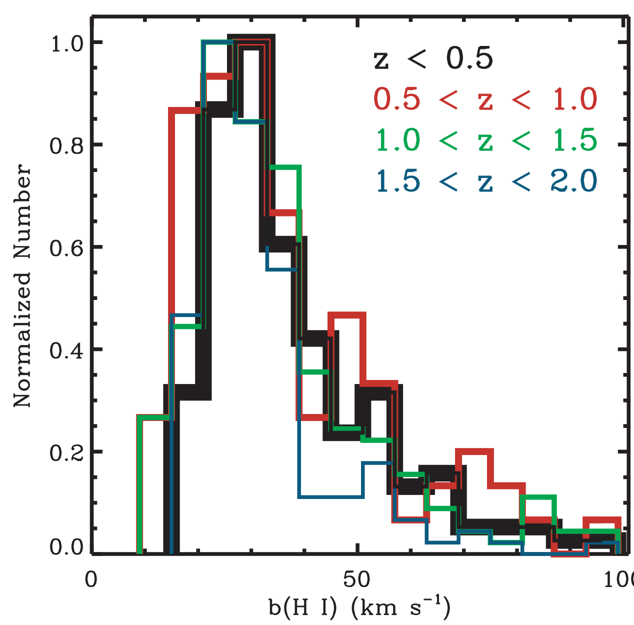

Fig. 9.—Comparison of the normalized distributions of b(H I) for the low-z sample (*black histogram*) and for the higher z sample (*colored histograms*) of Janknecht et al. (2006) for the weak absorbers $13.2 \leq \log N_{\rm H\,I} \leq 14.0$. The sample in the redshift range $z \simeq 0.5$–1.5 has a spectral resolution of about 10 km s^{-1}, while the other samples have about 7–8 km s^{-1}. Only data with less than 40% errors in b and $N_{\rm H\,I}$ are considered.

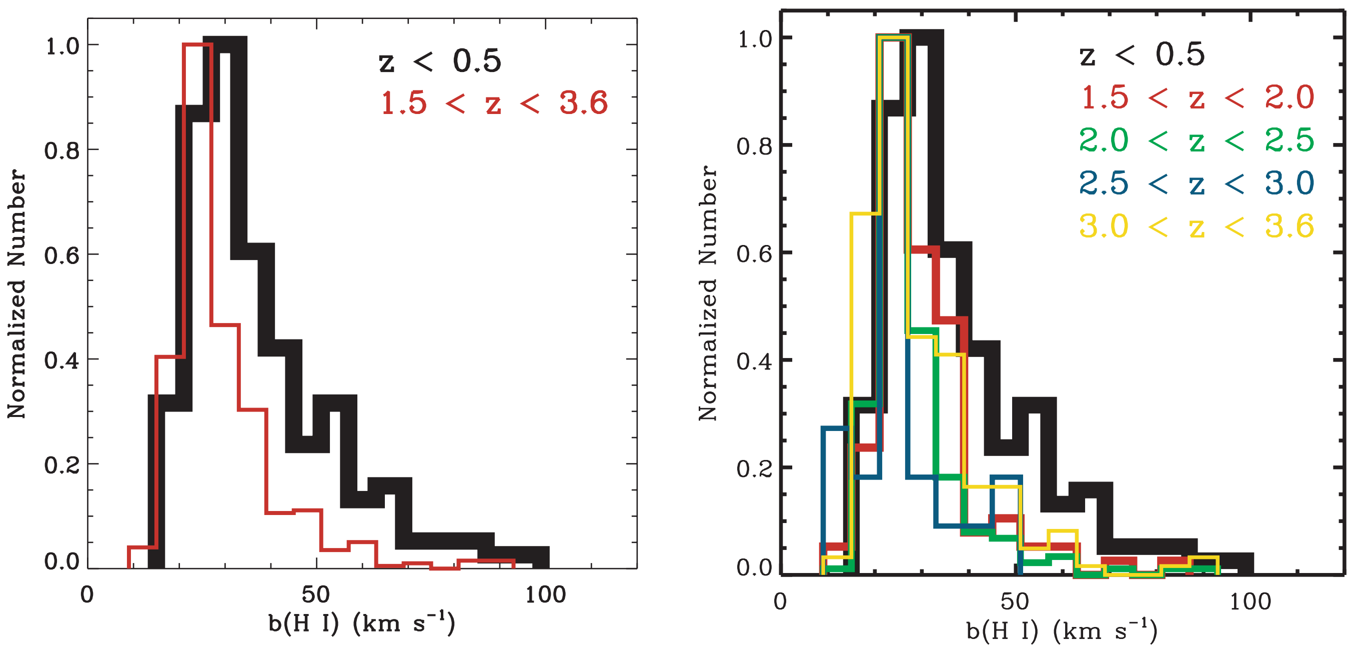

FIG. 10.—*Left*: Comparison of the normalized distributions of b(H I) for the low-z sample of data points (*black histogram*) and for the high-redshift sample (*red histogram*) from Kim et al. (2002a) for the weak absorbers $13.2 \leq \log N_{\rm H\,I} \leq 14.0$. *Right*: Same as the left panel, but the sample of Kim et al. (2002a) is separated in various redshift intervals. Each sample has a similar spectral resolution of about 7–8 km s^{-1}. Only data with less than 40% errors in b and $N_{\rm H\,I}$ are considered for the different samples.

distribution of b(H I) for the high-redshift sample ($1.5 \leq z \leq 3.6$) from Kim et al. (2002a). The left panel shows the entire sample at $1.5 \leq z \leq 3.6$, while the right panel shows the distribution of b in various redshift intervals for the high-z sample. The peak of the high-redshift normalized distribution in Figure 10 is not only shifted by $\sim$−5 km s^{-1} with respect to the peak of the low-redshift distribution, but also the width of the distribution is smaller for the high-redshift sample. Moreover, the low-redshift sample shows a tail of high-b(H I) absorbers that is much weaker in the high-redshift sample, showing that BLAs are more frequent at $z < 0.5$ than at $z > 1.5$. The right-hand side of Figure 10 verifies this conclusion for the various redshift intervals, i.e., BLAs appear more frequent at $z < 0.5$ than for any redshift intervals at $z > 1.5$. There is, however, no major difference between the various redshift intervals at $z > 1.5$. We also note that the b distribution at $z > 1.5$ shows little effect of line blending as z increases since there is scant evidence of a larger of fraction of BLAs at $z \gtrsim 3$ than at $1.5 \lesssim z \lesssim 2$.

We compare in Figure 11 our low-z sample to the high-z absorbers observed toward the QSO HS 1946+7658 (Kirkman & Tytler 1997). The median and mean are somewhat intermediate between our sample and the Kim et al. (2002a) sample (see Table 6). We slightly adjusted the redshift of the low-z sample so that the low- and high-z samples have exactly the same number of systems ($m = 130$); hence, the two distributions can be directly compared. The peak of the high-z distribution in Figure 10 is again shifted by $\sim$−5 km s^{-1} with respect to the peak of the low-z distribution. A higher number of systems with $40 < b \leq 70$ km s^{-1} is found in the low-redshift sample. At $b > 70$ km s^{-1} the high-redshift sample appears to have a larger number of systems. However, we note that the data of Kirkman & Tytler (1997) have S/N up to 200, and, as we discussed in § 2, our sample is not complete for $b > 80$ km s^{-1}. A Kolmogorov-Smirnov test yields a maximum deviation between the two cumulative distributions of the low- and high-redshift samples $D = 0.210$ with a level of significance $P = 0.006$; the null hypothesis of no difference between the two data sets is therefore rejected.

So far, we have ignored the effects of evolution of column density in the absorbers in our comparison. According to the numerical simulation of Davé et al. (1999) the dynamical state of an absorber depends mainly on its overdensity, so that a column density range traces absorbers of progressively higher overdensity as

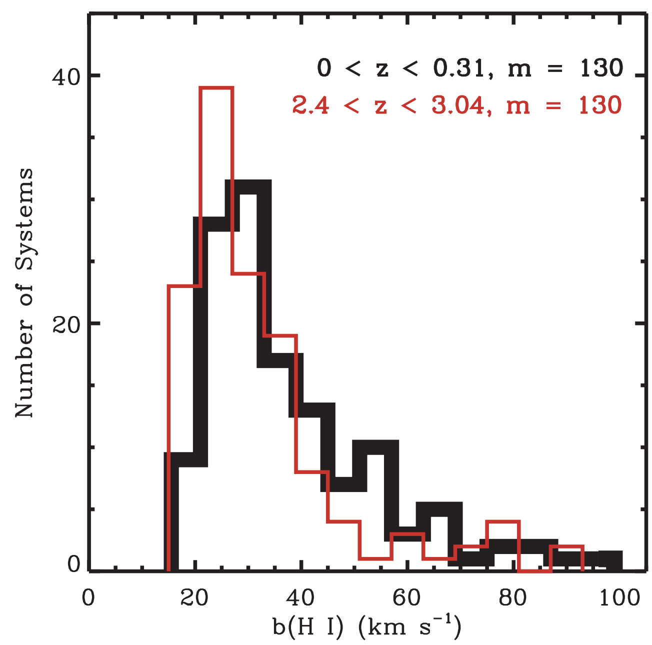

FIG. 11.—Comparison of the distributions of b(H I) for the low-z STIS E140M sample (*black histogram*) and for the high-z Keck sample (*red histogram*) of Kirkman & Tytler (1997) for the weak absorbers $13.2 \leq \log N_{\rm H\,I} \leq 14.0$. The number of absorbers in each sample is the same: $m = 130$. Only data with less than 40% errors in b and $N_{\rm H\,I}$ are considered for both samples.

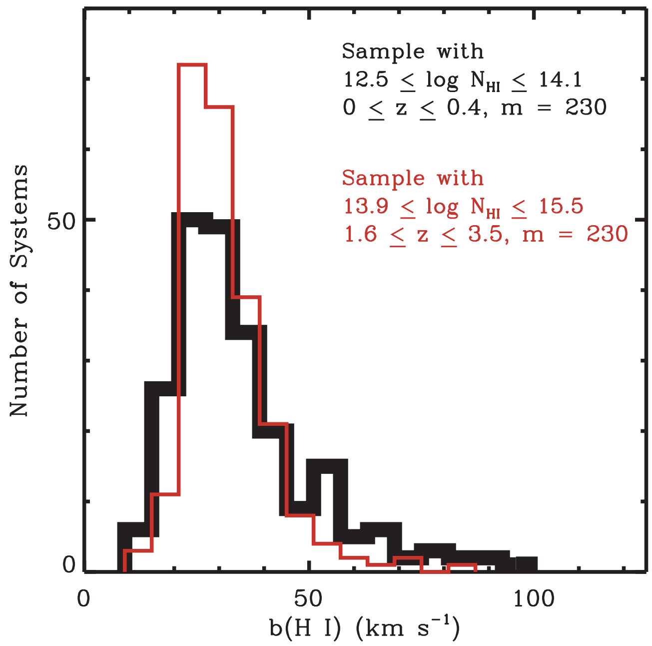

FIG. 12.—Comparison of the distribution of b(H I) for the low-z STIS E140M sample of data points (*black histogram*) and for the high-redshift sample (*red histogram*). The samples cover different ranges in log $N_{\rm H\,I}$. Higher column density systems at high redshift are expected to be physically analogous to the low-density systems at low redshift in an expanding universe. But note that in the high-redshift sample, BLAs are often likely to be blends of narrower lines (see § 4.2). The high-redshift data are from Kim et al. (2002a). The number of absorbers in each sample is the same: $m = 230$. Only data with less than 40% errors in b and $N_{\rm H\,I}$ are considered in both samples.

the universe expands. Therefore, according to equation (2), a low-redshift H I absorber is physically analogous not to a high-redshift H I absorber with the same column density, but to an absorber with column density $10^{0.4(z_{\rm high}-z_{\rm low})/0.7}$ times higher (Davé et al. 1999). With the average redshifts of 2.6 and 0.2 of the high-redshift sample of Kim et al. (2002a) and our sample, this corresponds to a column density roughly 25 times higher, i.e., a sample with $12.5 \leq \log N_{\rm H\,I} \leq 14.1$ at low z is physically analogous to the high-z sample with $13.9 \leq \log N_{\rm H\,I} \leq 15.5$. At such high column density, BLAs are likely to trace, in large part, narrower, strong absorbers that are blended together (see § 4.2). We nonetheless make this comparison in Figure 12, where both samples have the same number of systems. The high-redshift sample has again a larger fraction of systems in the range $b = [20, 40]$ km s^{-1} than the low-redshift sample. The fraction of BLAs at low redshift is again larger than the fraction of BLAs at high redshift with $b > 50$ km s^{-1}. This is remarkable since the low-redshift sample is far from complete for $\log N_{\rm H\,I} \lesssim 13.2$ and the high-redshift sample likely overestimates the number of true BLAs (i.e., BLAs that are not blends of NLAs). We again apply a Kolmogorov-Smirnov test on the two cumulative distributions of the low- and high-redshift samples and find $D = 0.130$ with a level of significance $P = 0.029$; again the null hypothesis of no difference between the two data sets is rejected.

4.4. *Evolution of $d\mathcal{N}/dz$ as a Function of b*

In Figure 13, we show $d\mathcal{N}/dz$ ($0 < b \leq 100$ km s^{-1}), $d\mathcal{N}$(NLA)/dz ($b \leq 40$ km s^{-1}), $d\mathcal{N}$(BLA)/dz ($40 < b \leq 100$ km s^{-1}), and $[d\mathcal{N}({\rm BLA})/dz]/[d\mathcal{N}({\rm NLA})/dz]$ as a function of the redshift. Only systems with $13.2 \leq \log N_{\rm H\,I} \leq 14.0$ and $\sigma_b/b, \sigma_N/N \leq 0.4$ are considered in this figure. We estimated $d\mathcal{N}/dz$ for each sight line over the redshift interval available along a given sight line. The redshift at which $d\mathcal{N}/dz$ is plotted in Figure 13 corresponds to the mean redshift interval in a given sight line. The vertical bars are Poissonian errors, while the horizontal bars represent the standard deviation around the mean of the observed redshifts of the Lyα absorbers. For the sample of Janknecht et al. (2006), several lines of sight have a redshift path larger than 0.6, and we divided those into two redshift intervals. The left diagram in Figure 13 includes all the sight lines available in the various samples, while the right diagram includes all the sight lines available in the low-z sample and high-z samples of Kim et al. (2002a) and Kirkman & Tytler (1997), but only the highest quality data in the Janknecht et al. (2006) sample (see § 4.2).

The top two panels of Figure 13 show the usual number density evolution with little or no evolution between redshifts 0 and ∼1.0–1.6 and an evolution of $d\mathcal{N}/dz$ with z at higher redshift (see for example Kim et al. 2002a). At high redshift, $d\mathcal{N}/dz$ decreases with decreasing z [$d\mathcal{N}/dz \propto (1+z)^\gamma$, $\gamma > 0$] according to the expansion of the universe, which forces any initial baryon overdensity to thin out (e.g., Davé et al. 1999, and references therein). The expansion also results in a decrease of recombinations of the free electrons with the protons and thus in an additional decline in $d\mathcal{N}/dz$. The break in $d\mathcal{N}/dz$ near $z \sim 1.6$ [$\log(1+z) \sim 0.4$] is believed to be primarily caused by the drop in the UV background because of the declining quasar population (Theuns et al. 1998; Davé et al. 1999). In the top panels, the solid line shows $d\mathcal{N}/dz = (d\mathcal{N}/dz)_0(1+z)^\gamma$, where $\gamma = 1.42$ was adopted from Kim et al. (2002a), who find this value for the weak absorbers with $13.1 \leq \log N_{\rm H\,I} \leq 14.0$. The value of $(d\mathcal{N}/dz)_0$ was adjusted to match the data. For the entire sample ($0 < b \leq 100$ km s^{-1}) or the sample restricted to $b < 40$ km s^{-1}, this line represents well the evolution of $d\mathcal{N}/dz$ at $z > 1$, but we note that when the best quality data are considered (*right panels*), the break in the evolution appears to occur at $z \sim 1.6$.

The second row from the bottom in Figure 13 shows that $d\mathcal{N}$(BLA)/dz is generally similar or higher at low and mid redshift than between redshifts 1.6 and 2. At $z \gtrsim 2$, $d\mathcal{N}$(BLA)/dz increases and is larger at $z > 2.5$ than $d\mathcal{N}$(BLA)/dz at $z < 1.5$. The Hubble expansion must be the primary driver in the evolution of these structures at high redshift, and despite the expansion, the BLA number density is comparable to $d\mathcal{N}$(BLA)/dz at high z, which contrasts remarkably with the evolution of $d\mathcal{N}$(NLA)/dz from low to high z. This difference is even more striking when we consider the ratio $\mathcal{R} \equiv [d\mathcal{N}({\rm BLA})/dz]/[d\mathcal{N}({\rm NLA})/dz]$ (*bottom panels*), which is higher in the low-redshift sample than in the high-redshift sample. On the left-hand side of the diagram, at mid redshift there is a very large scatter in the redshift range $0.9 \lesssim z \lesssim 1.2$. This scatter clears up when only the best quality data of the mid-z sample are considered (see right-hand side of the diagram). The distribution of $\mathcal{R}$ between redshifts ∼1.6–3.5 is actually nearly flat, showing that the slope controlling the evolution of $d\mathcal{N}$(NLA)/dz and $d\mathcal{N}$(BLA)/dz at $z \gtrsim 1.6$ must be about the same, further strengthening that NLAs and BLAs must follow a similar evolution dictated by the expansion of the universe. We note that $\mathcal{R}(z > 2.5)$ is slightly larger than $\mathcal{R}(z \sim 2)$, possibly indicating some spurious increase of BLAs, possibly due to line blending and blanketing effects that are more serious at $z > 2.5$ than at $z \sim 2$. However, in view of the large scatter in the various samples, this result does not appear statistically significant. The gray crosses in the bottom panels show the average $\mathcal{R}$ over the redshift range depicted by the horizontal gray bar (the vertical gray bar assumes Poissonian errors). At $z \lesssim 1.6$, $\mathcal{R}$ is larger than at $z > 1.6$, as both the individual $\mathcal{R}$ and average $\mathcal{R}$ show; $\mathcal{R}$ is a factor 3.2 higher at $z \lesssim 0.4$ than at $z \gtrsim 1.6$.

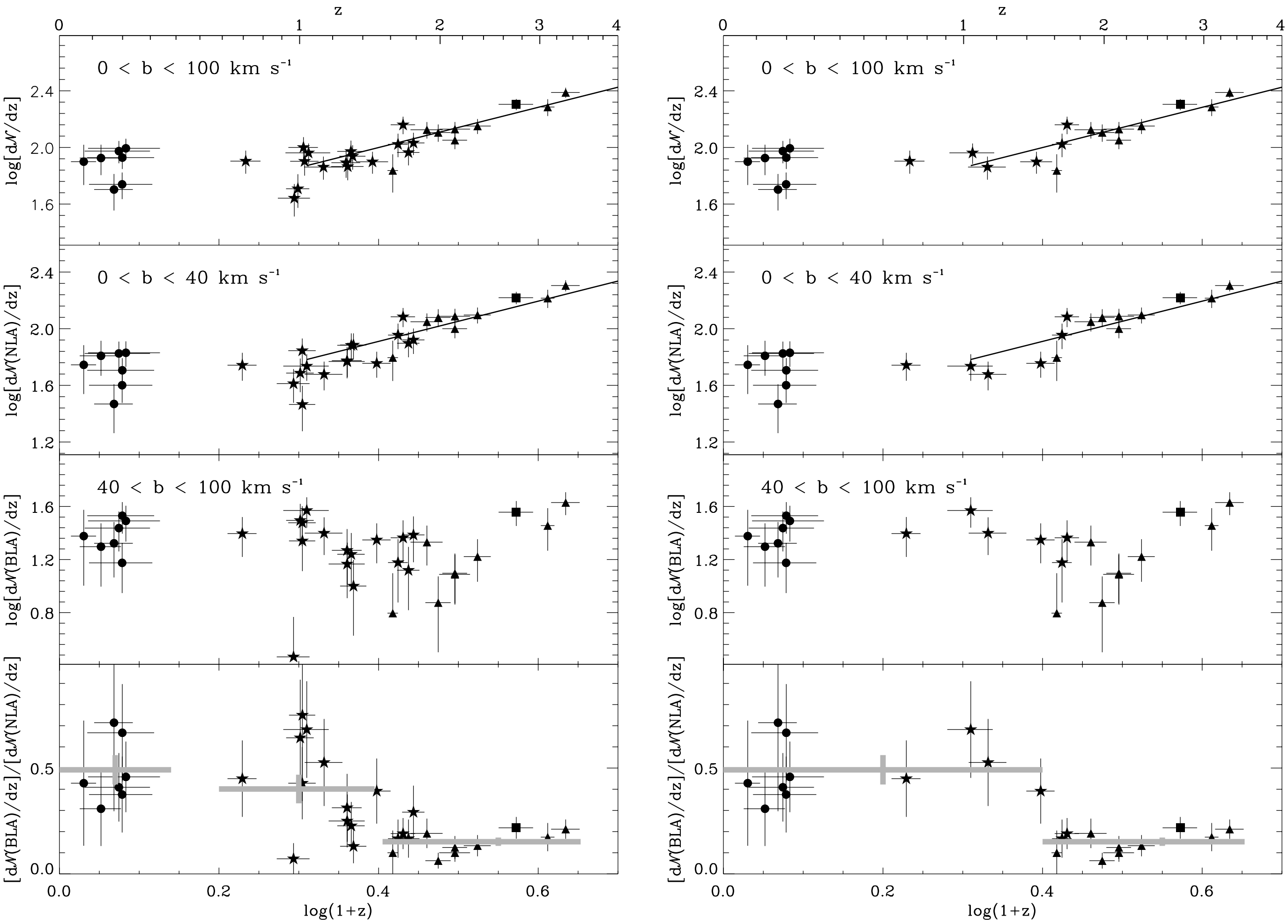

Fig. 13.—Lyα redshift density of the entire sample ($0 < b \leq 100$ km s^{-1}), the NLAs ($b < 40$ km s^{-1}), the BLAs ($40 \leq b \leq 100$ km s^{-1}), and the ratio of the Lyα redshift density fraction of the BLAs to the NLAs (*bottom panel*). We only consider absorbers with $13.2 \leq \log N_{\rm H\,I} \leq 14.0$ and with errors less than 40% in b and $N_{\rm H\,I}$. In the top two panels, the solid line shows $d\mathcal{N}/dz \propto (1+z)^{1.42}$, adopted from Kim et al. (2002a). The solid gray crosses in the bottom panels are the mean of $[d\mathcal{N}({\rm BLA})/dz]/[d\mathcal{N}({\rm NLA})/dz]$, where the horizontal bars indicate the redshift range over which the mean is estimated. The vertical bars are Poissonian errors. The symbols have the following meaning: circles are estimated from the low-redshift sample (see Table 1 for the references), stars are estimated from the sample of Janknecht et al. (2006), triangles are estimated from the sample of Kim et al. (2002a), and square are estimated from the sample of Kirkman & Tytler (1997). The left panel considers all the data with the conditions listed above from these various samples, while in the right panel we remove the lowest quality measurements of Janknecht et al. (2006; see § 4.2).

When only the best data of Janknecht et al. (2006) are considered, $\mathcal{R}$ at mid-redshift ($0.6 \lesssim z \lesssim 1.5$) appears similar to the value observed at low redshift.

If we had considered systems with $b \leq 80$ km s^{-1}, the same conclusions would be drawn. If we had considered a cutoff for the NLAs of $b = 50$ or 60 km s^{-1} instead of 40 km s^{-1}, similar conclusions would also be drawn. If absorbers with $13.2 \leq \log N_{\rm H\,I} \leq 16.5$ are considered, we find that $\mathcal{R}(z < 0.5) \sim 3\mathcal{R}(z > 1.6)$, despite the fact many BLAs at high z may actually be blends of narrower lines (see § 4.2).

4.5. *Implications*

We find that (1) the distribution of b for the BLAs has a distinctly more prominent high-velocity tail at low and middle z than at high z; (2) the median and mean b-values at low and mid z are systematically higher than at high z; and (3) the ratio $[d\mathcal{N}({\rm BLA})/dz]/[d\mathcal{N}({\rm NLA})/dz]$ at low and middle z is a factor $\sim$3 higher than at high z. These conclusions hold for a division $b = 40$, 50, or 60 km s^{-1} between NLAs and BLAs. For the reasons discussed in § 4.2, we believe that these are intrinsic properties of the evolution of the physical state of the gas that are not caused by comparing data with different S/N and line blending and blanketing effects. However, simulated spectra probing various redshifts, with realistic inputs would certainly help to unravel how exactly some of these issues (e.g., continuum placement, line blending effect, different S/N ratios) balance each other. Our results strongly suggest that if the broadening is mostly thermal, a larger fraction of the low-z universe is hotter than the high-z universe, and if the broadening is mostly nonthermal, the low-z universe is more kinematically disturbed than the high-z universe. It is likely that both possibilities are true.

5. THE DIFFERENTIAL COLUMN DENSITY DISTRIBUTION FUNCTION

The differential column density distribution $f(N_{\rm H\,I})$ is defined such that $f(N_{\rm H\,I}, X)\, dX dN_{\rm H\,I}$ is the number of absorption systems with column density between $N_{\rm H\,I}$ and $N_{\rm H\,I} + dN_{\rm H\,I}$ and redshift path between X and $X + dX$ (e.g., Tytler 1987),

$$f(N_{\rm H\,I})\, dN_{\rm H\,I} dX = \frac{m}{\Delta N_{\rm H\,I} \Sigma \Delta X}\, dN_{\rm H\,I} dX, \qquad (5)$$

where m is the observed number of absorption systems in a column density range $\Delta N_{\rm H\,I}$ centered on $N_{\rm H\,I}$ obtained from our

TABLE 7
The Power-Law Fit to the Distribution Function $f(N_{\rm H\,I}) = C_{\rm H\,I} N_{\rm H\,I}^{-\beta}$

[$\log N_{\rm min}$, $\log N_{\rm max}$]	β	$\log C_{\rm H\,I}$
$b \le 40$ km s^{-1}		
[13.2, 16.5]	1.76 ± 0.06	12.1
[13.2, 14.4]	1.83 ± 0.06	13.0
[14.4, 16.5]	1.52 ± 0.10	8.4
$b \le 150$ km s^{-1}		
[13.2, 16.5]	1.84 ± 0.06	13.3
[13.2, 14.4]	1.92 ± 0.05	14.4
[14.4, 16.5]	1.61 ± 0.11	9.9

Notes.—Only data with σ_b/b, $\sigma_N/N \le 0.4$ are included in the various samples (for more details, see § 5).

sample of seven QSOs with a total absorption distance coverage $\Sigma\Delta X = 2.404$ (see § 2). Empirically, it has been shown that at low and high redshift, $f(N_{\rm H\,I})$ is well fitted by a single power law (e.g., Tytler 1987; Petitjean et al. 1993; Hu et al. 1995; Lu et al. 1996; Kim et al. 2002a; Penton et al. 2000, 2004; Davé & Tripp 2001):

$$f(N_{\rm H\,I})\, dN_{\rm H\,I} dX = C_{\rm H\,I} N_{\rm H\,I}^{-\beta}\, dN_{\rm H\,I} dX. \quad (6)$$

In Table 7, we show the results from the maximum likelihood estimate of the parameters for the slope β and the normalization constant where

$$C_{\rm H\,I} \equiv m_{\rm tot}(1-\beta)/\{N_{\rm max}^{1-\beta}[1-(N_{\rm min}/N_{\rm max})1-\beta]\},$$

where $m_{\rm tot}$ is the total number of absorbers in the column density range $[N_{\rm min}, N_{\rm max}]$. We separate our sample into absorbers with $b \le 40$ km s^{-1} and $b \le 150$ km s^{-1}. For both b-samples we also choose three different column density ranges: (a) [13.2, 16.5] dex, (b) [13.2, 14.4] dex, and (c) [14.4, 16.5] dex. The lower limit of samples (a) and (b) corresponds to our threshold of completeness. The largest observed column density in our sample is $\sim 10^{16.5}$ cm^{-2}. Hence, sample (a) corresponds to the whole sample with $W \gtrsim 90$ mÅ, while sample (b) only covers the weak Lyα systems, and (c) covers the strong Lyα systems. The cut at 14.4 was chosen because the sample analyzed by Penton et al. (2004) suggested a change of slope near this value (see below). Note that for each sample, we only consider absorbers with $\sigma_b/b \le 0.4$ and $\sigma_N/N \le 0.4$.

In Figure 14, we show the column density differential distribution of the identified absorbers for the combined sample with $b \le 40$ km s^{-1} and the maximum likelihood fits to the data. The fit to the sample with $b \le 150$ km s^{-1} implies a general increase of β (see Table 7) for the various column density intervals. For sample (a), if we vary $\log N_{\rm min}$ from 13.2 to 13.4, the results from the maximum likelihood fit essentially do not change. If $\log N_{\rm min} < 13.1$, β decreases rapidly since our sample is not complete anymore. If $N_{\rm max}$ is reduced, β will increase, as sample (b) shows. For sample (b) with either $b \le 40$ or $b < 150$ km s^{-1}, if $\log N_{\rm min}$ increases by up to 0.4 and/or $\log N_{\rm max}$ varies by $\pm^{1.0}_{0.5}$ dex, the results do not statistically change. However, for sample (c), the results are more uncertain. While β appears to flatten at larger column densities, there are too few absorbers

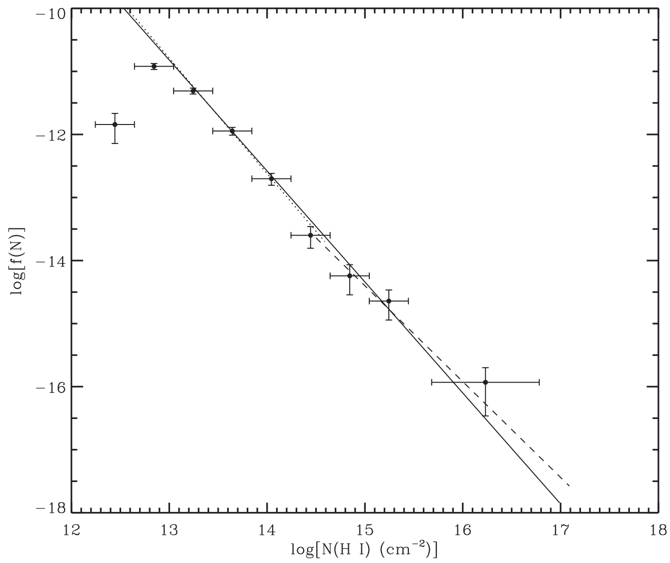

Fig. 14.—Differential density distribution [$f(N_{\rm H\,I})$] without an incompleteness correction plotted against $\log N_{\rm H\,I}$. Only H I absorbers with b(H I) ≤ 40 km s^{-1} and errors less than 40% in b and $N_{\rm H\,I}$ are considered. The data are binned only for purpose of presentation. The solid line is a maximum likelihood fit to the data [$f(N_{\rm H\,I}) = C_{\rm H\,I} N_{\rm H\,I}^{-\beta}$] with the slope $\beta = 1.76$ for H I column density systems between 13.2 and 16.5 dex. The dotted and dashed lines are maximum likelihood fit to the data for $13.2 \le \log N_{\rm H\,I} \le 14.4$ and $14.4 \le \log N_{\rm H\,I} \le 16.5$, respectively (see Table 7 and § 5 for more details).

with large H I column density to have a full understanding of the possible change in the slope. In particular, it is not clear from our sample where the break in the slope occurs, since for $\log N_{\rm min} \approx 14.4 \pm 0.5$ dex, β is $\sim$1.5. At the 2 σ level, β from sample (c) is essentially the same as for samples (a) and (b).

With GHRS and STIS grating moderate spectral resolution observations, Penton et al. (2004) found at $z \lesssim 0.1$, $\beta = 1.65 \pm 0.07$ for $12.3 \le \log N_{\rm H\,I} \le 14.5$ and $\beta = 1.30 \pm 0.30$ at $\log N_{\rm H\,I} > 14.5$ with few data points. In their work, $N_{\rm H\,I}$ was obtained from the equivalent width, assuming $b = 25$ km s^{-1}. Their results are consistent with the Key Project data presented by Weymann et al. (1998) and our results. Davé & Tripp (2001) derived $\beta = 2.04 \pm 0.23$ for $13 \lesssim \log N_{\rm H\,I} \lesssim 14$. They used STIS E140M spectra of two QSOs and were able to derive b and N independently using an automated Voigt profile-fitting software but not allowing for BLAs. Within 1 σ, our results are the same.

At $z \gtrsim 1.5$, several studies using high-resolution spectra obtained with the Keck and the VLT have shown that $\beta \approx 1.5$ for H I column density ranging from a few times 10^{12} cm^{-2} up to a few times 10^{20} cm^{-2} (e.g., Tytler 1987; Hu et al. 1995; Lu et al. 1996), although there may be some deviation from a single power law at $\log N_{\rm H\,I} > 14$ (Petitjean et al. 1993; Kim et al. 1997, 2002a). There is also some suggestion that for a given H I interval, β increases as z decreases, but this is statistically uncertain at $z > 2$ (Kim et al. 2002a). If we compare our results to Kim et al. (2002a), we find an increase of β as z decreases in the column density interval 13.2–14.4 dex or 13.2–16.5 dex, but not in the column density interval 14.4–16.5 dex, although in this range the number of data points is too small to draw any firm conclusion. Finally, the analysis of Janknecht et al. (2006) at $0.5 < z < 2.0$ shows that β is intermediate between β at $z < 0.5$ and β at $z > 2$. Therefore, it appears that the column density distribution steepens with decreasing z in the column density range 13.2–16.5 dex. A redshift dependence was found in the numerical results presented by Theuns et al. (1998), but the observed rate of evolution of β appears to be smaller than their models suggest.

6. THE BARYON DENSITY OF THE IGM

6.1. *Narrow Lyα Absorption Lines*

To estimate the baryon content of the photoionized Lyα forest at low z, we follow the method presented by Schaye (2001). The mean gas density relative to the critical density can be obtained from the H I density distribution function,

$$\Omega(\mathrm{NLA}) = \frac{\mu_{\mathrm{H}} m_{\mathrm{H}} H_0}{\rho_c c} \int N_{\mathrm{H\,I}} \frac{n_{\mathrm{H}}}{n_{\mathrm{H\,I}}} f(N_{\mathrm{H\,I}})\, dN_{\mathrm{H\,I}}, \qquad (7)$$

where $m_{\mathrm{H}} = 1.673 \times 10^{-24}$ g is the atomic mass of hydrogen, $\mu_{\mathrm{H}} = 1.3$ corrects for the presence of helium, $H_0 = 100$ km s^{-1} Mpc^{-1}, $\rho_c = 3H_0^2/(8\pi G) = 1.06 \times 10^{-29}$ g cm^{-3} is the current critical density, n_{H} and $n_{\mathrm{H\,I}}$ are the density of the total hydrogen and neutral hydrogen, respectively, $N_{\mathrm{H\,I}}$ is the neutral hydrogen column density, and $f(N_{\mathrm{H\,I}})$ is the differential density distribution function discussed in § 5. Assuming that the gas is isothermal and photoionized, the previous equation can be simplified to

$$\Omega(\mathrm{NLA}) \approx 2.2 \times 10^{-9} h^{-1} \Gamma_{12}^{1/3} T_4^{0.59} \left(\frac{f_g}{0.16}\right)^{1/3} \times \int_{N_{\min}}^{N_{\max}} N_{\mathrm{H\,I}}^{1/3} f(N_{\mathrm{H\,I}})\, dN_{\mathrm{H\,I}}, \qquad (8)$$

where $h \equiv H_0/(100$ km s^{-1} Mpc$^{-1})$, Γ_{12} is the H I photoionization rate in units of 10^{-12} s^{-1}, T_4 is the IGM temperature in units of 10^4 K, and f_g is the fraction of mass in gas in which stars and molecules do not contribute. Schaye (2001) states that in cold, collapsed clumps, $f_g \approx 1$, but on the scales of interest here f_g is close to the ratio of the total baryon density to the matter density, which according to Spergel et al. (2003) is 0.16. We therefore set $f_g = 0.16$. We use $\Gamma_{12} = 0.05$ from Haardt & Madau (1996) for our average redshift $\bar{z} = 0.19$. This value of Γ_{12} is consistent with the value derived by Davé & Tripp (2001) at $\bar{z} = 0.17$. The typical temperature of the IGM is not well defined in the current simulations of the low-redshift universe. Schaye (2001) noted a good agreement between his estimate of T_4 and the Davé et al. (1999) estimate, and we therefore use equation (3) for estimating T_4. But as these authors noted, there is a very large scatter in the T-$\rho/\bar{\rho}$ relation at $z \sim 0$ producing uncertainty in the baryon determination from equation (8) because of temperature variations. Note that for our calculation, we set $z = \bar{z}$. Because $\Omega(\mathrm{NLA}) \propto N_{\mathrm{H\,I}}^{4/3-\beta}$ with $\beta > 4/3$, the low column density systems dominate $\Omega(\mathrm{NLA})$; therefore, $N_{\min}$ sets the temperature in equation (8). Furthermore, since $N_{\min}$ dominates the solution of equation (8), using this equation is dependent on the data quality of the current sample. We therefore emphasize that we only derive the contributions of the denser parts of the photoionized Lyα forest.

To estimate the baryon content of the photoionized regions, we only use H I absorbers with $b \leq 40$ km s^{-1}. Broader systems are here assumed to be principally collisionally ionized. For the interval of H I column density $10^{13.2}$–$10^{16.5}$ cm^{-2}, using the best fit parameters of $f(N_{\mathrm{H\,I}})$ listed in Table 7 for this range of column densities and with $(\Gamma_{12}, T_4, f_g, h) = (0.05, 1.2, 0.16, 0.7)$, we find $\Omega(\mathrm{NLA})/\Omega_{\mathrm{b}} \simeq 0.19$ for absorbers with $\log N_{\mathrm{H\,I}} \geq 13.2$, where $\Omega_{\mathrm{b}} = 0.044$ is the ratio of the total baryon density to the critical density (Spergel et al. 2003; Burles et al. 2001; O'Meara et al. 2001). If we assume that the power law described in § 5 fits the data extending to the lower observed column density (12.42 dex), we find $\Omega(\mathrm{NLA})/\Omega_{\mathrm{b}} = 0.29$ for the column density range [12.4, 16.5] with $(\Gamma_{12}, T_4, f_g, h) = (0.05, 0.6, 0.16, 0.7)$. Such an assumption is not unrealistic, since, in high-redshift spectra, Lu et al. (1996) and Kirkman & Tytler (1997) show using their simulation results that weak absorbers (down to 12.1–12.5 dex) follow the same column density distribution as the stronger absorbers. Assuming $\beta = 1.76$ (see Table 7) and equation (3), the dependence between $\Omega(\mathrm{NLA})/\Omega_{\mathrm{b}}$ and $N_{\min}$ can be approximated by $\Omega(\mathrm{NLA})/\Omega_{\mathrm{b}} \simeq 0.2[N_{\min}/(10^{13.2}\ \mathrm{cm}^{-2})]^{-0.18}$.

With the available data, there is no indication of subcomponent structure in the broad Lyα absorption lines. However, broadening mechanisms other than thermal may also be important. If this is the case, the thermal broadening could decrease significantly for the broad Lyα absorption lines, implying that many of those lines would arise in the photoionized IGM, not the WHIM. If the complete sample with $\log N_{\mathrm{H\,I}} = [13.2, 16.5]$ and $b \leq 150$ km s^{-1} is considered, $\Omega(b < 150\ \mathrm{km\ s^{-1}})/\Omega_{\mathrm{b}} \gtrsim 0.23$ for $(\Gamma_{12}, T_4, f_g, h) = (0.05, 1.2, 0.16, 0.7)$. If the sample with $\log N_{\mathrm{H\,I}} = [12.4, 16.5]$ and $b \leq 150$ km s^{-1} is considered, $\Omega(b < 150\ \mathrm{km\ s^{-1}})/\Omega_{\mathrm{b}} = 0.40$ for $(\Gamma_{12}, T_4, f_g, h) = (0.05, 0.6, 0.16, 0.7)$. Therefore, if the BLAs are tracing photoionized gas, the estimate of Ω would increase by a factor of $\sim$1.3. These BLAs would not then contribute to the baryon budget in the BLAs determined in § 6.2.

Estimating a reliable error on $\Omega(\mathrm{NLA})$ remains a difficult task with our current knowledge. The estimate of $\Omega(\mathrm{NLA})$ is model-dependent, since the representative temperature of the IGM is not well known. More numerical simulations of the low-redshift IGM spanning a wider range of parameters and using the results from the current sample may tighten Γ and T. If T changes by 20%, $\Omega(\mathrm{NLA})/\Omega_{\mathrm{b}}$ can change by about 10%–15%; if Γ changes by 20%, $\Omega(\mathrm{NLA})/\Omega_{\mathrm{b}}$ can change by about 10%. The Ω estimate is also very sensitive to the slope β; a change of β by ± 0.005 can introduce a change in $\Omega(\mathrm{NLA})/\Omega_{\mathrm{b}}$ by about $\mp$4%. Furthermore, the low column density absorbers dominate the baryon fraction and the low column density cutoff, $N_{\min}$, is unknown. Therefore, while the exact baryon content is uncertain in the photoionized IGM, it is clear that the photoionized Lyα forest is a large reservoir of baryons. The baryon fraction in the diffuse photoionized phase traced by (narrow) Lyα absorbers predicted by cosmological models in the low-redshift universe varies by a factor of 2 ($\sim$20%–40%) among the various simulations (Davé et al. 2001), in general agreement with our results. We note that Penton et al. (2004) derived $\Omega(\mathrm{Ly}\alpha)/\Omega_{\mathrm{b}} = 0.29 \pm 0.04$ for the photoionized phase in the column density range [12.5, 17.5] dex.[7] In view of our discussion on the various uncertainties, we believe that their error estimate appears optimistic.

6.2. *Broad Lyα Absorption Lines*

Baryons also reside in the WHIM, a shock-heated intergalactic gas with temperatures in the range 10^5–10^7 K. Cosmological hydrodynamical simulations predict that the WHIM may contain 30%–50% of the baryons at low redshift (Cen & Ostriker 1999; Davé et al. 1999). BLAs may trace the 10^5–10^6 K WHIM if the broadening is purely thermal, following $T[\mathrm{K}] = (b\ [\mathrm{km\ s^{-1}}]/0.129)^2$. The cosmological mass density of the broad Lyα absorbers in terms of today critical density can be written as (Richter et al. 2004; Sembach et al. 2004)

$$\Omega(\mathrm{BLA}) = \frac{\mu_{\mathrm{H}} m_{\mathrm{H}} H_0}{\rho_c c} \frac{\Sigma f_{\mathrm{H}}(T_i) N_{\mathrm{H\,I}}(i)}{\Sigma \Delta X} \approx 1.667 \times 10^{-23} \frac{\Sigma f_{\mathrm{H}}(T_i) N_{\mathrm{H\,I}}(i)}{\Sigma \Delta X}, \qquad (9)$$

[7] It is unclear which parameters Penton et al. (2004) used with the Schaye (2001) method [if we set the parameters to those given by Penton et al., i.e., $(\Gamma_{12}, T_4, f_g, h) = (0.03, 0.5, 0.16, 0.7)$, we found that the values in their Table 4 (Schaye column) are a factor $\sim$3 too high].

where $f_H(T)$ is the conversion factor between H I and total H, and the other symbols have the same meaning as in equation (7). For our sample, $\Sigma\Delta X = 2.404$. In equation (9) the sum of $f_H(T_i)N_{H\,I}(i)$ over index i is a measure of the total hydrogen column density in the BLAs. When collisional ionization equilibrium (CIE) is assumed, the conversion factor between H I and total H was approximated by Richter et al. (2004) from the values given in Sutherland & Dopita (1993) for temperatures 10^5–10^6 K:

$$\log f_H(T) \approx -13.9 + 5.4\log T - 0.33(\log T)^2. \quad (10)$$

For low-density absorbers, the CIE hypothesis is, however, probably a poor approximation, because the photoionization from the UV background is important (Richter et al. 2006b). Recently, Richter et al. (2006a) used the output of the numerical simulation carried out by Fang & Bryan (2001) to investigate the intervening O VI absorption in the WHIM, to study the BLAs in the low-redshift IGM. They found that a significant number of BLAs could be photoionized in particular systems that have relatively low b-values in the range 40–65 km s^{-1}. Their simulation that includes collisional ionization and photoionization suggests that the hydrogen ionization fraction can be approximated as

$$\log f_H(T) \approx -0.75 + 1.25\log T. \quad (11)$$

According to Figure 5 in Richter et al. (2006a), the CIE hypothesis (eq. [10]) provides a firm lower limit to $f_H(T)$. Equations (10) and (11) converge as b increases, but never intersect.

In Table 5 and § 3.3, we saw that the S/N has little effect on the estimate for $d\mathcal{N}(\mathrm{BLA})/dz$ for the highest S/N spectra, but can reduce $d\mathcal{N}(\mathrm{BLA})/dz$ for the lowest S/N data in our sample. To reduce the uncertainty from the broadening of the H I absorbers found in low-S/N spectra, we restricted our sample to absorbers with $\sigma_b/b, \sigma_N/N \le 0.3$. To estimate $\Omega(\mathrm{BLA})$, we consider b-value intervals [40, 150], [40, 65], and [65, 150] km s^{-1}. In the [40, 65] km s^{-1} interval, Richter et al. (2006a) found that about 1/3 of the BLAs traces cool photoionized gas ($T < 2\times10^4$ K), i.e., $b_{nt} \gg b_{th}$ for these systems. If all the BLAs are assumed to be thermally broadened, we would overestimate $\Omega(\mathrm{BLA})$. We therefore randomly pick 2/3 of the BLAs in the [40, 65] km s^{-1} b-range to estimate f_H. (We note that the baryon content of the photoionized BLAs with $T \lesssim 10^4$ K is less than 1%–2%, according to Richter et al. 2006a.) In the [65, 150] km s^{-1} b-range, the number of BLAs tracing cool photoionized systems is small (less than ~5%), and we assume that all the BLAs in this range of b-values are mostly thermally broadened. With the conditions listed above, there are 12 systems in the [65, 150] km s^{-1} interval and 31 in the [40, 65] km s^{-1} b-range. In Table 8, we summarize our estimates of $\Omega(\mathrm{BLA})/\Omega_b$ using equations (9), (10), and (11), where T was derived assuming $b_{th} \approx 0.9b_{obs}$, following the simulation of Richter et al. (2006a). The largest difference in the estimates of the baryon budget from CIE and Richter et al.'s model is for low b-values, where photoionization plays a more important role. We note that if we restricted our sample to systems with $\sigma_b/b, \sigma_N/N \le 0.2$, $\Omega(\mathrm{BLA})/\Omega_b$ would decrease by a factor ~1.2, but would increase by a factor ~1.2–2.4 if $\sigma_b/b, \sigma_N/N \le 0.4$.

As for the estimate of the baryon budget of the NLAs, with our current knowledge it appears to be a very difficult task to estimate an error on the baryon budget in BLAs. It is model-dependent. Richter et al. (2006a) provided estimates of the amount of the BLAs that probe cool photoionized gas and the amount of thermal broadening in BLAs. These estimates may change with refined cosmological models. If we assume that the broadening for *all* the BLAs is purely thermal ($b_{th} = b_{obs}$), the estimates of $\Omega(\mathrm{BLA})/\Omega_b$ in the [40, 150] km s^{-1} b-range would increase by a factor 1.6, i.e., in the CIE model, $\Omega(\mathrm{BLA})/\Omega_b \simeq 0.13$, and in the collisional ionization plus photoionization model of Richter et al. (2006a), $\Omega(\mathrm{BLA})/\Omega_b \simeq 0.32$. The broadening could be due to several unresolved components in some cases, or the nonthermal broadening could be important. This is partly accounted for since we remove a 1/3 of the BLAs in the [40, 65] km s^{-1} b-range. Since we discarded systems with large errors in b and N, for the current data set, a single Gaussian fit provides a good representation of the observed profiles. However, as we discussed in § 3.2, the formal errors given by the fit may not be sufficient, especially for the weaker and broader systems. Richter et al. (2006b) and the other papers mentioned in Table 1 present several examples of BLAs that are well fitted with a single Gaussian, sometimes with the presence of several H I Lyman series transitions that further constrain the fit parameters (see also the discussion in § 4.2). To further explore the quality of the profile fitting, the Cosmic Origin Spectrograph (COS) could really improve the situation by increasing the number of sight lines and increasing the S/N in the spectra. Additional theoretical simulations of the low-z IGM with higher resolution and refined physics combined with the analysis of simulated spectra should improve our understanding of the BLAs.

In summary, the CIE estimate provides a firm and conservative limit for the baryon budget in collisionally ionized BLAs, $\Omega(\mathrm{BLA})/\Omega_b \gtrsim 0.1$ for systems with $40 < b \lesssim 150$ km s^{-1}, $\log N_{H\,I} \ge 13.2$, and $\sigma_b/b, \sigma_N/N \le 0.3$. The BLA simulations show that the ionization fraction in BLAs is governed by collisional ionization and photoionization. Therefore, $\Omega(\mathrm{BLA})/\Omega_b \gtrsim 0.2$ (with the same constraints that those listed above) should better reflect the baryon budget of the BLAs in the low-z IGM. This is likely a lower estimate as well since the existing observations do not have the S/N to detect the broader systems (where most of the baryons are believed to exist) and the numerous weaker BLAs (see Fig. 6) and are not complete at $b \gtrsim 80$ km s^{-1}.

TABLE 8

ESTIMATES OF THE BARYON DENSITY IN BLAs

b (km s^{-1})	$\Omega_{CIE}(\mathrm{BLA})/\Omega_b$ [a]	$\Omega_{C+P}(\mathrm{BLA})/\Omega_b$ [b]
[40, 65]	0.03	0.11
[65, 150]	0.05	0.09
[40, 150]	0.08	0.20

NOTES.—Only data with $\sigma_b/b, \sigma_N/N \le 0.3$ and $\log N_{H\,I} \ge 13.2$ are included in the various samples. In the [40, 65] km s^{-1} interval, only 2/3 of the BLAs are considered. We derive the temperature of the absorbers assuming $b_{th} = 0.9b_{obs}$. The baryon density in the interval [40, 150] km s^{-1} is the sum of $\Omega(\mathrm{BLA})$ in the two other intervals. $\Omega_b = 0.044$ (Spergel et al. 2003).

[a] Obtained from eqs. (9) and (10); baryonic density for the BLAs assuming that they are collisionally ionized and CIE applies.

[b] Obtained from eqs. (9) and (11); baryonic density for BLAs assuming that they are collisionally ionized and photoionized using the results from the hydrodynamical simulations of Richter et al. (2006a; see § 6.2 for more details).

6.3. *Baryon Budget of the Low-Redshift Universe*

At redshift 2–4, observations of the Lyα forest show that about 80%–90% of the total baryon budget is found in the cool photoionized phase of IGM (Rauch et al. 1997; Weinberg et al. 1997; Kim et al. 2001). In the low-redshift universe, Fukugita et al. (1998) show that 9%–10% of the total baryons are found in galaxies (stars, neutral gas, molecular gas) and ~6% of the baryons are associated with the hot plasma in clusters of galaxies.

Our analysis of the low-redshift Lyα forest shows the presence of NLAs and BLAs. The NLAs trace the cool photoionized IGM, while the BLAs are likely to probe the cool photoionized IGM and the hot highly ionized gas in the WHIM. There are still many uncertainties that are not controlled in the determination of the baryon content in the low-redshift Lyα forest. But at least 20% of the baryons are found in the denser parts of the photoionized phase (NLAs, $b \leq 40$ km s^{-1}, $\log N_{\rm H\,I} \geq 13.2$, and $\sigma_b/b, \sigma_N/N \leq 0.4$) and at least ~10% are found in the WHIM (BLAs, $40 < b \leq 150$ km s^{-1}, $\log N_{\rm H\,I} \geq 13.2$, and $\sigma_b/b, \sigma_N/N \leq 0.3$), corresponding to at least 30% of the total baryon budget. We believe that these limits are very conservative, since they do not take into account the low column density photoionized absorbers and the broadest BLAs. Furthermore, recent simulations of the BLAs in low-redshift universe show that the BLAs may trace both photoionized and collisionally ionized gas. Using the simulations of Richter et al. (2006a), we find that the BLAs include at least 20% of the baryons. We have also seen that Ω in the cool photoionized IGM is dominated by the low column density H I absorbers (i.e., absorbing gas with overdensity $\rho/\bar{\rho} \lesssim 2$). If the weak systems follow the same differential column density distribution function as the stronger absorbers, the cool photoionized gas traced by the NLAs with $\log N_{\rm H\,I} \geq 12.4$ can contain ~30% of the total baryons. Combining these NLA and BLA budgets, the low-redshift IGM contains at least ~50% of the baryons. This is much larger than the known amount of baryons in galaxies and clusters of galaxies in the low-redshift universe. High-S/N data will allow us to search for the weakest Lyα absorbers ($\lesssim 10^{12.5}$ cm^{-2}) and estimate their column density distribution, search for the very broad absorbers and the weak BLAs, and provide a better understanding of their physical nature. It is, however, already apparent from this study that the IGM traced by the narrow and broad Lyα absorption lines in the low-redshift universe is a major reservoir of baryons.

7. SUMMARY

We analyze the physical properties of the low-z IGM traced by H I absorbers from a sample of seven QSOs observed with the E140M mode of STIS ($R \sim 44{,}000$) and with *FUSE* ($R \sim 15{,}000$). These seven lines of sight were fully analyzed and have been or will be presented in recent and future papers (see references in Table 1 and the Appendix of this paper). Our sample has a total unblocked redshift path of 2.064 corresponding to a total absorption distance of 2.404 and is complete for $\log N_{\rm H\,I} \gtrsim 13.2$, provided $b \lesssim 80$ km s^{-1}. With high spectral resolution, the column density ($N_{\rm H\,I}$) and the Doppler parameter (b) were independently estimated, providing the opportunity to directly study the distribution and evolution of b. The spectral resolution of the STIS E140M H I observations in our sample is similar to that of the high-redshift ($z \gtrsim 1.5$) observations obtained with Keck HIRES and VLT UVES. This similarity allows a relatively simple study of the evolution of the b-parameter of the neutral hydrogen gas in the intergalactic medium. Because the nominal lower temperature of the WHIM is $T \sim 10^5$ K, we consider two different populations of H I absorbers throughout this work: narrow Lyα absorbers (NLAs), with $b \leq 40$ km s^{-1}; and broad Lyα absorbers (BLAs), with $b > 40$ km s^{-1}. Our main findings, applicable at redshifts $z \lesssim 0.4$, are

1. The H I Doppler width distribution has a high-velocity tail that develops at $b \approx 40$–60 km s^{-1}. The b-$N_{\rm H\,I}$ distribution reveals, for the NLAs, an increase of b with increasing $N_{\rm H\,I}$ with a very large scatter. We find that most of the BLAs are found in the H I column density range [13.2, 14.0] dex, and the broader systems are found for $13.1 \lesssim \log N_{\rm H\,I} \lesssim 13.5$. Recent cosmological simulations of BLAs show a good agreement with the observations, but clearly indicate that broader absorbers and many weak BLAs ($\log N_{\rm H\,I} \lesssim 13.1$) remain to be discovered.

2. We find $d\mathcal{N}(\text{BLA})/dz = 30 \pm 4$ for absorbers with $40 < b \lesssim 150$ km s^{-1}, $\log N_{\rm H\,I} \geq 13.2$, and $\sigma_b/b, \sigma_N/N \leq 0.4$. The narrow H I absorbers are more frequent, with $d\mathcal{N}(\text{NLA})/dz = 66 \pm 6$ for absorbers with $b \leq 40$ km s^{-1}, $\log N_{\rm H\,I} \geq 13.2$, and $\sigma_b/b, \sigma_N/N \leq 0.4$. Very narrow absorbers ($b \lesssim 15$ km s^{-1}) with $\log N_{\rm H\,I} \geq 13.2$ are scarce. The number of weak NLAs and BLAs ($\log N_{\rm H\,I} \leq 14$) is far larger than the number of strong NLAs and BLAs, respectively.

3. For the narrow absorbers with $13.2 \leq \log N_{\rm H\,I} \leq 16.5$ and $\sigma_b/b, \sigma_N/N \leq 0.4$, we find that the column density distribution, $f(N_{\rm H\,I}) \propto N_{\rm H\,I}^{-\beta}$, can be fitted with $\beta = 1.76 \pm 0.06$. For the entire sample (i.e., including NLAs and BLAs), the slope changes to 1.84 for the same column density range. We confirm an increase of β with decreasing z when our results are compared to higher redshift analyses. There is some weak evidence for a break at $\log N_{\rm H\,I} \sim 14.4$, but the location of this break is uncertain because of the small-number statistics for the higher column density lines.

4. We argue that various samples probing different redshift ranges can be directly compared when the conditions $0 < b \leq 100$ km s^{-1}, $13.2 \leq \log N_{\rm H\,I} \leq 14.0$, and $\sigma_b/b, \sigma_N/N \leq 0.4$ are set. The distribution of b for the broad absorbers has a distinctly more prominent high-velocity tail at low z than at high z ($1.5 \lesssim z \lesssim 3.6$). The median and mean b-values are systematically larger by ~15%–30% at $z \lesssim 0.5$ than at $1.5 \lesssim z \lesssim 3.6$. The ratio of the number density of BLAs to NLAs at low z is larger than at high z by a factor ~3. This suggests that a larger fraction of the low-z universe is hotter than at $1.5 \lesssim z \lesssim 3.6$ and/or the low-z universe is more kinematically disturbed than the high-z universe.

5. The NLAs trace the cool photoionized IGM at $T \lesssim 10^4$ K, and we find that $\Omega(\text{NLA})/\Omega_{\rm b} \simeq 0.2[N_{\rm min}/(10^{13.2}\ \text{cm}^{-2})]^{-0.18}$ [when $f(N_{\rm H\,I}) \propto N_{\rm H\,I}^{-1.76}$ and assuming $N_{\rm H\,I} \propto T^{-0.42}$], where $N_{\rm min}$ is the lowest H I column density in the sample considered to estimate $\Omega(\text{NLA})$. The contribution to the baryon budget of the denser parts of the photoionized Lyα forest with $\log N_{\rm H\,I} \gtrsim 13.2$ is ~20%. If the weakest H I absorber with $\log N_{\rm H\,I} = 12.4$ follows the same $f(N_{\rm H\,I})$, the cool photoionized gas with $\log N_{\rm H\,I} \gtrsim 12.4$ contains about 30% of the total baryons.

6. The BLAs trace mostly the highly ionized gas in the WHIM at $T \simeq 10^5$–10^6 K if the width of the BLAs is dominated by thermal motions. The assumption of collisional ionization equilibrium provides a firm lower limit to the amount of the baryons in the WHIM traced by the BLAs ($40 < b \lesssim 150$ km s^{-1}, $\log N_{\rm H\,I} \geq 13.2$, and $\sigma_b/b, \sigma_N/N \leq 0.3$): $\Omega(\text{BLA})/\Omega_{\rm b} \gtrsim 10\%$. If a hydrodynamical simulation including the effects of collisional ionization and photoionization is used to estimate the ionization correction for the BLAs, we find that at least 20% of the baryons are in the BLAs.

7. Our most conservative estimate of the baryon budget in absorbers with $\log N_{\rm H\,I} \gtrsim 13.2$ shows that the Lyα forest has at least about 30% of the baryons (NLAs+BLAs), far larger than the baryon budget in galaxies. We suggest that the low-redshift IGM with $T \lesssim 10^6$ K traced by the NLAs with $\log N_{\rm H\,I} \gtrsim 12.4$ and the BLAs with $\log N_{\rm H\,I} \gtrsim 13.2$ could contain at least 50% of the baryons (this is a lower limit since the broader BLAs where most baryons reside remain to be discovered). The estimates of the amount of baryons still rely, however, on critical assumptions (e.g., pure thermal broadening versus other broadening mechanisms, temperature of the IGM, behavior of the weak narrow systems) that produce uncertainties that are currently not well controlled. Observationally, if COS is deployed, our understanding of the BLAs, in particular, will improve, given the high-S/N spectra that COS should obtain (but with approximately 2 times lower resolution than for the STIS observations presented here). The present paper and future observations of the low-z IGM should motivate more precise cosmological simulations of the low- and high-z IGM that are needed for our understanding of the intrinsic properties of the BLAs and NLAs.

We thank the *HST* and *FUSE* mission operation teams for their continuous efforts to provide excellent UV and Far-UV spectroscopic data to the astronomical community. Support for this research was provided by NASA through grant HST-AR-10682.01-A. N. L. appreciates support from the University of Notre Dame for part of this work. P. R. acknowledges financial support by the German Deutsche Forschungsgemeinschaft (DFG) through Emmy-Noether grant Ri 1124/3-1. T. M. T. appreciates support from NASA grants NNG04GG73G and HST-GO-9184.08-A. B. P. W. acknowledges grants HST-GO-00754.01-A and NASA NNG04GD856. This research has made use of the NASA Astrophysics Data System Abstract Service and the Centre de Données de Strasbourg (CDS).

APPENDIX

We have revisited the H I measurements presented by Williger et al. (2006) toward PKS 0405−123. We were first motivated to produce a new analysis of the PKS 0405−123 *FUSE* and STIS E140M spectra because Williger et al. (2006) noted that several of their BLAs may be noise features. For our work, we needed to clearly differentiate a real detection from a noise feature. While reanalyzing the BLAs, we noted that some narrow H I lines were either not present in the spectra at the 3 σ level (although Williger et al. claimed to report only 4 σ features) or were misidentified. We have not identified the ultimate origin of the problem, but we suspect that the difference with Williger et al. can ultimately be traced to a difference in the manner in which the continuum placement was done. Williger et al. fitted a single global continuum, while we determine continua separately placed within $\pm$1000–3000 km s^{-1} of each absorption line. We therefore produce here a new line list and new measurements for H I toward PKS 0405−0123 in Table 9. This reanalysis also provides an overall coherent data sample, since the other sight lines were analyzed following the same methodology. In Table 9, we report our measurements for H I toward PKS 0405−123. These H I absorbers are detected at least at the 3 σ level. We list in this table the observed wavelengths and the rest-frame equivalent widths of the Lyα transition. The listed column densities and Doppler parameters were measured in the rest frame by N. Lehner (NL) following the method described in Lehner et al. (2006). The weak absorbers ($\log N_{\rm H\,I} < 14$) were also independently measured by P. Richter (PR) using the method described in Richter et al. (2004). In particular, different profile-fitting software was used by NL and PR. In Figure 15, we compare the column densities and b-values (for the weak absorbers) presented by Williger et al. (2006) to those listed in Table 9 (*left panels*). On the right-hand side, we present the measurements obtained by PR against those listed in Table 9. For both b and $N_{\rm H\,I}$, there is an excellent agreement between PR and NL measurements at the 1 σ level. In contrast, Williger et al. (GW) found generally larger column densities and Doppler parameters. The main difference between our analysis (NL and PR) and GW's analysis is that we systematically and *independently* chose the continua within $\pm$1000–3000 km s^{-1} of the H I absorption line, while GW fitted the continuum using a semiautomatic procedure (AUTOVP) combined with custom fitting in the vicinity of the QSO emission lines. Since these weak absorbers are generally detected solely in Lyα, the continuum placement is critical. Our method for the continuum placement was followed for all the other sight lines presented in this work. For the absorbers where Lyα and Lyβ are detected, our measurements and those made by GW agree within 1 σ.

Absorbers with $\log N_{\rm H\,I} > 14$ are detected in several Lyman series lines. For the absorbers that were fitted with a single component ($z = 0.03000$, 0.35099, 0.40571, and 0.40886), GW and our measurements are in agreement within 1 σ. GW fitted the systems listed in Table 9 at $z = (0.09657, 0.09659)$ and $(0.18262, 0.18287)$ with a single component. We found that a two-component fit provides a statistically better fit. The total column densities for those absorbers are in agreement within 1 σ with those measured by GW. For the partial Lyman limit system at $z = 0.167$, we found that five components provide a better fit to this complicated absorber (see Fig. 16 and note [6] in Table 9). We note that our fit is not yet as good as it should be despite our best effort (see Fig. 16). In particular, the broad component at $z = 0.16678$ may actually be narrower, since metal ions such as C III are detected at this redshift (this directly affects the measurements of the absorber at $z = 0.16661$, where C III is also detected). Finally, we fitted the system at $z = 0.36808$ with four components. This is not statistically different from the two-component fit presented by GW, but the four-component fit appears to be a better model when the kinematics of the metal ions are taken into account (see note [12] in Table 9 for more details).

In Table 10, we report the list of features that were identified as Lyα and claimed to be detected at least at the 4 σ level by GW. These features are actually either nondetections at the 3 σ level (according to our measurements) or were misidentified. The 181 Lyα absorbers toward PKS 0405−123 reported by GW now reduce to 74 absorbers (and in a few cases, those are multicomponent absorbers).

TABLE 9

IGM H I Revised Measurements toward PKS 0405−123

λ (Å)	z	$W_{Ly\alpha}$ (mÅ)	$\log N_{H\,I}$ (dex)	b(H I) (km s^{-1})	Note
1230.1364............	0.01190	53.5 ± 11.5	13.09 ± 0.09	7.2 ± 3.0	
1233.8078............	0.01492	35.1 ± 10.9	13.09 ± 0.11	11.5 ± 5.9	
1236.1053............	0.01681	45.3 ± 14.1	13.08 ± 0.10	25.0 ± 11.0	
1240.3360............	0.02029	48.7 ± 14.1	13.12 ± 0.12	32.2 ± 15.5	
1251.9578............	0.02985	65.4 ± 9.6	13.36 ± 0.13	12.4:	
1252.1401............	0.03000	255.4 ± 16.6	14.37 ± 0.04	20.3 ± 0.9	
1254.5228............	0.03196	90.5 ± 19.2	13.33 ± 0.08	54.0 ± 16.1:	
1272.3689............	0.04664	51.4 ± 12.1	13.09 ± 0.09	27.7 ± 9.2	
1287.3459............	0.05896	41.0 ± 10.2:	13.34 ± 0.10	76.5 ± 26.8	1
1287.6984............	0.05925	48.3 ± 9.3	12.76 ± 0.18	10.8:	1
1303.4171............	0.07218	49.5 ± 10.8	13.09 ± 0.08	44.8 ± 14.4	
1303.8182............	0.07251	44.6 ± 9.6	13.06 ± 0.07	19.0 ± 5.1	
1306.2252............	0.07449	31.8 ± 8.7	12.85 ± 0.11	17.5 ± 9.0	
1307.1249............	0.07523	42.1 ± 11.6	13.05 ± 0.11	47.7 ± 20.3	
1314.6134............	0.08139	236.0 ± 18.7	13.79 ± 0.02	54.3 ± 3.5	
1327.3172............	0.09184	472.2 ± 24.4	14.60 ± 0.02	39.1 ± 0.9	2
1333.0673............	0.09657	487.2 ± 27.9	14.57 ± 0.04	30.3 ± 2.3	3
1333.0916............	0.09659	...	13.90 ± 0.18	69.8 ± 19.8	3
1333.7845............	0.09716	50.9 ± 6.7	13.02 ± 0.05:	29.0 ± 3.2	
1340.8597............	0.10298	96.3 ± 19.2	13.40 ± 0.07	86.6 ± 19.4	
1374.9470............	0.13102	108.9 ± 15.1	13.46 ± 0.05	51.9 ± 7.9	
1376.5395............	0.13233	142.5 ± 13.5	13.64 ± 0.03	22.3 ± 1.7	
1377.4270............	0.13306	72.9 ± 11.5	13.29 ± 0.06	31.7 ± 6.3	
1378.2902............	0.13377	90.3 ± 16.2	13.34 ± 0.06	42.8 ± 8.1	
1381.5604............	0.13646	76.8 ± 13.2	13.34 ± 0.06	53.8 ± 10.8	4
1399.6739............	0.15136	49.2 ± 10.4	13.20 ± 0.07	37.0 ± 8.8	
1400.7436............	0.15224	114.8 ± 13.2	13.54 ± 0.04	22.4 ± 2.1	
1401.7162............	0.15304	223.3 ± 16.8	13.80 ± 0.03	46.3 ± 3.4	
1411.6482............	0.16121	157.5: ± 16.1	13.71 ± 0.04	54.1 ± 7.7	5
1412.0007............	0.16150	120.7: ± 13.1	13.27 ± 0.09	18.2 ± 4.4	5
1413.8485............	0.16302	110.7 ± 16.5	13.42 ± 0.05	34.0 ± 5.2	
1418.2128............	0.16661	...	13.29 ± 0.08:	7.9 ± 2.1:	6
1418.4194............	0.16678	...	13.91 ± 0.04:	74.9 ± 7.2:	6
1418.6139............	0.16694	...	15.33 ± 0.20	13.5 ± 3.7	6
1418.8327............	0.16712	...	16.30 ± 0.09	12.5 ± 5.6	6
1418.8571............	0.16714	844.0 ± 41.6	16.27 ± 0.13	29.9 ± 1.2	6
1432.9832............	0.17876	155.2 ± 19.6	13.61 ± 0.04	55.3 ± 7.3	4
1437.6757............	0.18262	684.3 ± 31.2	14.83 ± 0.03	32.6 ± 1.4	7
1437.9796............	0.18287	...	14.17 ± 0.04	25.4 ± 2.3	7
1447.6928............	0.19086	51.6 ± 13.3	13.17 ± 0.09	44.3 ± 15.7	
1471.8239............	0.21071	69.8 ± 15.4	13.27 ± 0.08	30.8 ± 8.8	
1472.4073............	0.21119	39.1 ± 10.1	13.09 ± 0.08	21.1 ± 7.1	
1478.2426............	0.21599	85.6 ± 11.9	13.36 ± 0.04	17.6 ± 2.4	
1493.1224............	0.22823	51.3 ± 11.5	13.19 ± 0.07	18.9 ± 4.5	
1508.1237............	0.24057	68.4 ± 14.8	13.27 ± 0.09	56.5 ± 19.1	
1513.6673............	0.24513	50.7 ± 12.8	13.23 ± 0.11	54.3 ± 24.3	8
1514.1656............	0.24554	154.4 ± 15.3	13.69 ± 0.03	22.8 ± 2.1	8
1521.4717............	0.25155	52.9 ± 12.3	13.20 ± 0.09	27.2 ± 8.6	
1523.5992............	0.25330	38.7 ± 11.8	13.05 ± 0.09	18.1 ± 7.1	
1530.0544............	0.25861	84.4 ± 15.5	13.37 ± 0.07	39.8 ± 8.8	
1532.2791............	0.26044	107.1 ± 15.3	13.45 ± 0.05	32.0 ± 5.7	
1540.9347............	0.26756	36.7 ± 10.9	12.96 ± 0.11	15.9 ± 7.7	
1566.2449............	0.28838	62.2 ± 17.1	13.32 ± 0.10	51.9 ± 18.9	
1574.5723............	0.29523	81.6 ± 19.8	13.33 ± 0.08	47.2 ± 13.1	
1577.5263............	0.29766	236.5 ± 20.3	13.97 ± 0.03	32.2 ± 2.4	9
1579.2039............	0.29904	75.6 ± 21.5	13.26 ± 0.12	48.9 ± 23.4	
1604.7208............	0.32003	105.2 ± 18.2	13.49 ± 0.05	19.0 ± 3.1	
1610.7628............	0.32500	115.6 ± 22.4	13.55 ± 0.06	65.9 ± 12.8	
1613.5831............	0.32732	79.5 ± 19.1	13.30:	30.9:	
1621.7281............	0.33402	194.3 ± 20.4	13.82 ± 0.03	30.4 ± 2.4	10
1631.2590............	0.34186	126.5 ± 19.6	13.51 ± 0.06	38.3 ± 7.8	11
1631.8425............	0.34234	85.5 ± 18.1	13.39 ± 0.08	42.4 ± 12.5	11
1642.3581............	0.35099	369.8 ± 30.4	14.25 ± 0.03	37.5 ± 2.1	
1642.9902............	0.35151	118.9 ± 19.2	13.53 ± 0.05	25.1 ± 4.5	
1643.7318............	0.35212	121.5 ± 21.5	13.57 ± 0.05	30.5 ± 4.9	

TABLE 9—*Continued*

λ (Å)	z	$W_{Ly\alpha}$ (mÅ)	$\log N_{\rm H\,I}$ (dex)	b(H I) (km s^{-1})	Note
1654.2716...................	0.36079	. . .	14.66 ± 0.14	37.7 ± 4.0	12
1654.2838...................	0.36080	767.0 ± 48.9	15.10 ± 0.06	18.2 ± 1.5	12
1654.7093...................	0.36115	. . .	13.63 ± 0.17	22.7 ± 7.6	12
1655.1347...................	0.36150	. . .	13.71 ± 0.10	44.3 ± 10.1	12
1657.3847...................	0.36335	103.3 ± 26.9	(<)13.55 ± 0.09	26.4 ± 4.5	13
1685.7938...................	0.38672	37.5 ± 10.9	13.21 ± 0.09	15.3 ± 5.9	
1708.8795...................	0.40571	460.5 ± 37.0	14.98 ± 0.02	33.0 ± 1.5	14
1712.7088...................	0.40886	341.6 ± 37.8	14.38 ± 0.03	39.9 ± 2.2	15
1713.5598...................	0.40956	95.6 ± 26.2	13.58 ± 0.07	26.4 ± 6.1	

NOTES.—The wavelength, λ, is the observed redshifted wavelength of Lyα. The equivalent width, $W_{Ly\alpha}$, is the rest-frame equivalent width of Lyα. A colon means that the result is uncertain.

(1) The Lyα for the systems at $z = 0.05925$ and 0.05896 were fitted simultaneously.

(2) We fitted simultaneously detected H I $\lambda\lambda$1215, 1025, 972, and 937 (H I λ949 is blended).

(3) We fitted simultaneously detected H I $\lambda\lambda$1215, 1025, and 937 (H I $\lambda\lambda$972 and 949 are blended). We found that a two-component fit improves the modeling of Lyα, yielding a narrow and broad component. If the BLA is mostly thermally broadened, it yields a temperature of $T \sim 3 \times 10^5$ K. O VI is found in this absorber (Prochaska et al. 2004). The temperature found from the H I broadening is consistent with O VI being mainly collisionally ionized.

(4) This profile appears asymmetric, but within the S/N a single-component fit is suitable. This system is, however, not accounted for in the BLAs in this paper because of the asymmetry.

(5) The Lyα for the systems at $z = 0.16121$ and 0.16150 were fitted simultaneously.

(6) The systems at $z = 0.16661$, 0.16678, 0.16694, 0.16712, and 0.16714 were fitted simultaneously. The equivalent width reported at $z = 0.16714$ is the total equivalent width for these absorbers. The systems at $z = 0.1671$ are detected from Lyα down to the Lyman Limit. Prochaska et al. (2004) derived the total column density of the system at $z \simeq 0.1671$, using the flux decrement at the Lyman limit. Williger et al. (2006) fixed the column density found by Prochaska et al. (2004) for the systems at $z = 0.16714$ and used H I $\lambda\lambda$1215 and 1025 to derive b. They fitted a very broad absorber at $z = 0.16692$ and a very narrow absorber at $z = 0.16628$. This fit appears satisfactory for H I $\lambda\lambda$1215 and 1025, but not for the other transitions (see Fig. 16). In particular, the core of the higher H I Lyman series is not reproduced. To reproduce the core of the line, we find that a two-component fit is necessary: a very narrow component with $b = 12$ km s^{-1} and a broader (but still relatively narrow) component with $b = 30$ km s^{-1}. Furthermore, the C II and C III kinematics (see Figs. 9 and 10 in Prochaska et al. 2004) indicate four distinct components at -136, -93, -40, and 0 km s^{-1}. We, therefore, fitted five components set initially at -136, -93, -40, -5, and 5 km s^{-1}. The velocity of the component at -40 km s^{-1} was not allowed to vary; all the other parameters for the various components were allowed to vary. For the fit, we used simultaneously detected H I $\lambda\lambda$1215, 1025, 937, 930, 926, 923, 919, 918, and 917 lines. H I $\lambda\lambda$972 and 949 are contaminated, while H I λ920 suffers from fixed-pattern noise. We did not use higher Lyman series transitions because the continuum placement becomes uncertain due to the flux decrement. The resulting fit is shown in Fig. 16. We note that Prochaska et al. (2004) used a curve-of-growth analysis with two components separated by 40 km s^{-1} based on the C II and Si II profiles and found 16.35 and 15.5 dex, which is roughly consistent with our results for the systems $z = 0.16694$, 0.16712, and 0.16714. While our fit appears more satisfactory than the one presented by Williger et al. (2006), who did not take into account the velocity structure of the metal ion profiles, the solution may actually be more complicated. The errors do not reflect that there may be more than five components. In particular, the broad component at $z = 0.16678$ may actually be narrower since metal ions such as C III are detected at this redshift; this directly affects the measurements of the absorber at $z = 0.16661$, where C III is also detected. Therefore, we mark the measurements at $z = 0.16661$ and 0.16678 as uncertain.

(7) The systems at $z = 0.18261$ and 0.18287 were fitted simultaneously. We used detected H I $\lambda\lambda$1215, 972, and 949 (H I $\lambda\lambda$1025 and 937 are contaminated). We note that Williger et al. (2006) fitted a single component at $z = 0.18271$; a two-component fit improves the fit. The equivalent width is the total equivalent width including both systems.

(8) The systems at $z = 0.24513$ and 0.24554 were fitted simultaneously. We used detected H I $\lambda\lambda$1215 and 1025 in the profile fitting.

(9) We fitted simultaneously detected H I $\lambda\lambda$1215 and 1025. We note that H I λ972 is also detected and possibly contaminated by a weak Lyα system.

(10) We fitted simultaneously detected H I $\lambda\lambda$1215 and 1025.

(11) The Lyα for the systems at $z = 0.34186$ and 0.34234 were fitted simultaneously.

(12) The equivalent width is the total equivalent width including the systems at $z = 0.36079$, 0.36080, 0.36115, and 0.36150. The system at $z = 0.36080$ is detected in H I $\lambda\lambda$1215, 1025, 972, 949, 937, 930, and 923 (H I λ926 is contaminated). We undertook to fit these lines with two, three, and four components. Statistically, these fits are comparably good because Lyα is so noisy. The three- and four-component fits appear, however, to be better models than the two-component fit, especially when one takes into account that O VI $\lambda\lambda$1031 and 1037 appear to be present in the weakest component. The three-component fit does not fit the blue edge of the Lyα profile as well as the four-component fit, but otherwise the three- or four-component fits are quite similar. We note that our two-component fit yields similar results to those found by the two-component fit of Williger et al. (2006).

(13) Partially blended with interstellar C I* λ1657.379.

(14) We fitted simultaneously detected H I $\lambda\lambda$1215, 1025, 972, 949, 937, 930, 926, and 923.

(15) We fitted simultaneously detected H I $\lambda\lambda$1215, 1025, 972, and 949.

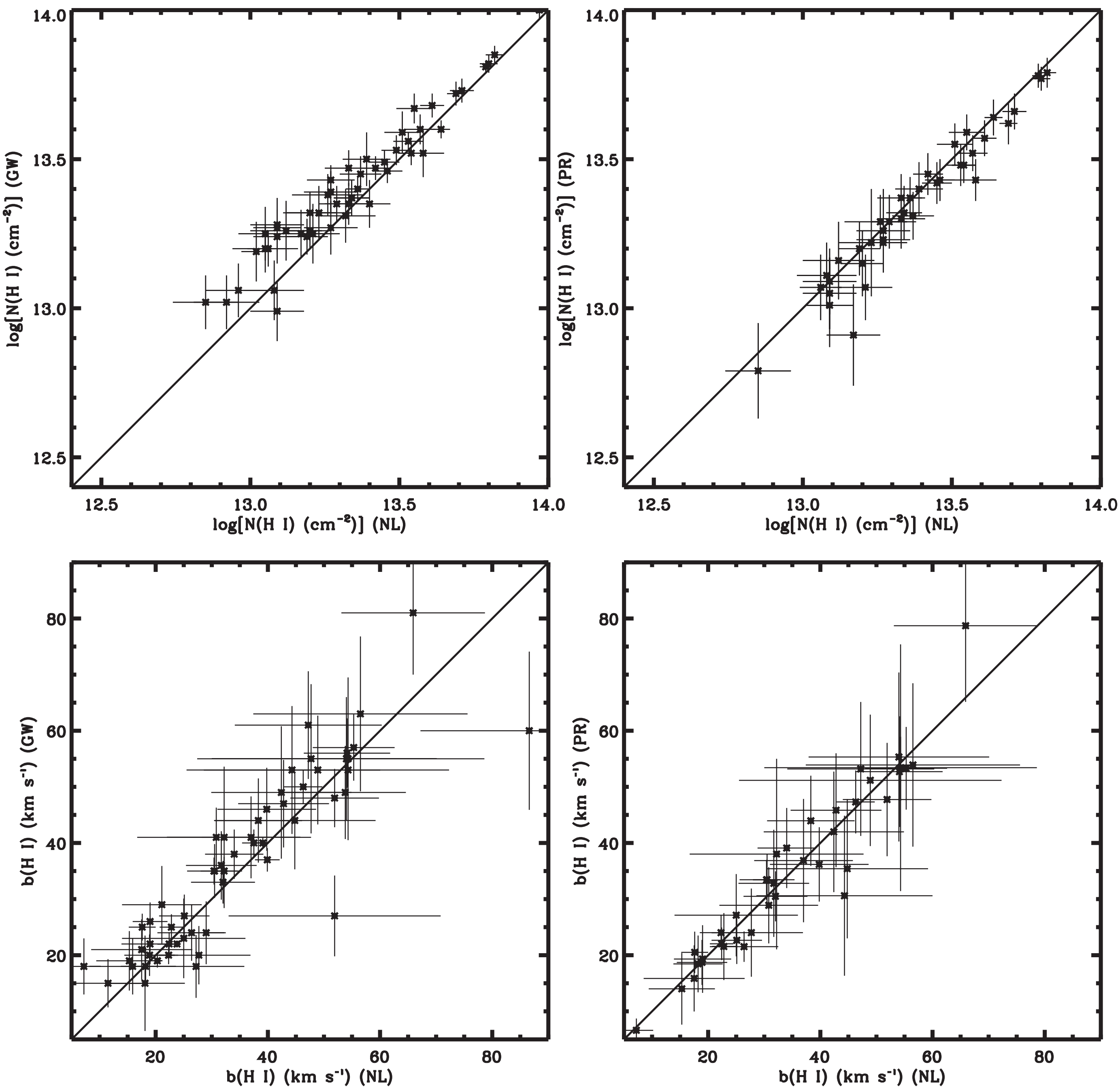

Fig. 15.—Comparison of H I column densities and Doppler parameters for the weak absorbers (log $N_{\rm H\,I} \leq 14$). The left-hand side compares the fit results from Williger et al. (2006; GW) and N. Lehner (NL). The right-hand side compares the independent measurements produced by P. Richter (PR) and N. Lehner (NL). Identical results would lie along the solid line.

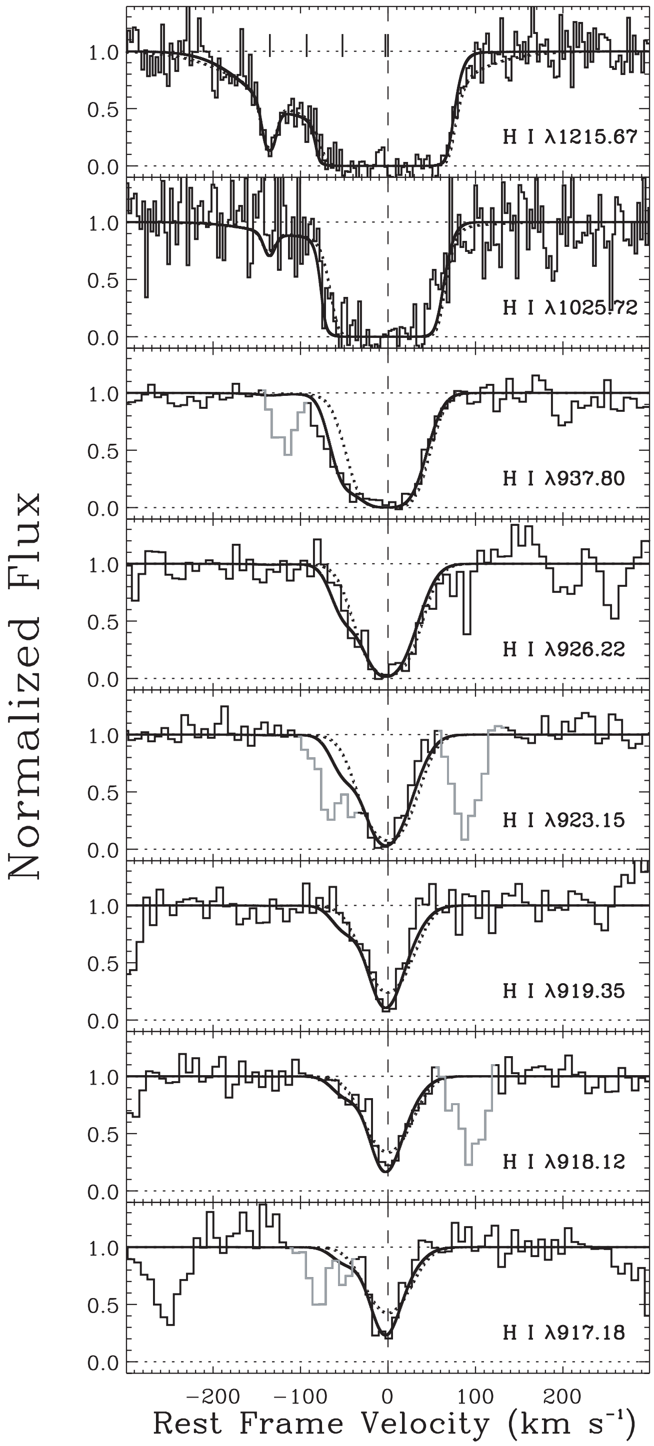

FIG. 16.—Profile fitting to the system at $z = 0.167$. The solid thick line shows the fit adopted in Table 9. The dotted thick line shows the fit adopted by Williger et al. (2006). The light parts of the spectra denote blends with other features. The tick marks in the H I λ1215 panel are the centroids of the five components found in our profile fitting. From left to right, the tick marks correspond to $z = 0.16661$, 0.16678, 0.16694, 0.16712, and 0.16714. Discrepancies of the fits to the data are discussed in the text and note (6) of Table 9.

TABLE 10

NONDETECTION AND CONFUSION WITH OTHER ISM/IGM LINES LISTED AS Lyα DETECTION IN WILLIGER ET AL. (2006) TOWARD PKS 0405−123

λ (Å)	z	$W_{\rm H\,I}$ (mÅ)	log $N_{\rm H\,I}$ (dex)	Note
1218.8185	0.00259	<137.9	<13.40	
1220.3381	0.00384	<52.9	<13.00	
1226.8541	0.00920	<43.4	<12.90	
1232.5921	0.01392	<42.1	<12.90	
1234.2820	0.01531	<44.3	<12.91	
1237.1509	0.01767	<35.9	<12.82	
1238.7434	0.01898	<39.2	<12.86	
1240.5912	0.02050	<35.0	<12.81	
1246.0617	0.02500	<39.9	<12.87	
1293.0596	0.06366	<37.2	<12.82	
1295.3086	0.06551	<32.7	<12.78	
1297.2415	0.06710	<16.4	<12.48	
1298.5180	0.06815	<32.6	<12.78	
1299.5634	0.06901	<32.6	<12.78	
1303.1132	0.07193	<31.9	<12.77	
1305.5080	0.07390	<36.5	<12.83	
1306.5413	0.07475	<34.7	<12.81	
1315.6954	0.08228	<31.7	<12.77	
1318.8195	0.08485	<31.9	<12.77	
1319.7921	0.08565	<32.1	<12.77	
1329.2014	0.09339	...	...	1
1338.9997	0.10145	<32.4	<12.77	
1346.9259	0.10797	<32.8	<12.78	
1358.1951	0.11724	<32.5	<12.78	
1359.6053	0.11840	<33.5	<12.79	
1360.6994	0.11930	<31.8	<12.77	
1361.0399	0.11958	<32.4	<12.78	
1384.8912	0.13920	<32.0	<12.77	
1422.4069	0.17006	<31.3	<12.76	
1422.7230	0.17032	<31.9	<12.77	
1422.9660	0.17052	<32.0	<12.77	
1424.1210	0.17147	<31.9	<12.77	
1424.7166	0.17196	<31.9	<12.77	
1425.0570	0.17224	<31.8	<12.77	
1427.1357	0.17395	<32.2	<12.77	
1435.7428	0.18103	<31.9	<12.77	
1439.6572	0.18425	<37.7	<12.84	
1440.2530	0.18474	<37.2	<12.82	
1440.6663	0.18508	<37.4	<12.83	
1449.0909	0.19201	<39.5	<12.86	
1449.7472	0.19255	...	...	2
1452.2637	0.19462	...	...	2
1453.4673	0.19561	<39.2	<12.86	
1454.8895	0.19678	<36.6	<12.83	
1463.6910	0.20402	<35.5	<12.82	
1464.4933	0.20468	<35.0	<12.81	
1465.3808	0.20541	<36.6	<12.83	
1467.3259	0.20701	<32.6	<12.77	
1467.8486	0.20744	<33.4	<12.79	
1474.5713	0.21297	<42.4	<12.89	
1474.9602	0.21329	<42.3	<12.89	
1476.2732	0.21437	<42.6	<12.89	
1477.0876	0.21504	<34.6	<12.80	
1478.8383	0.21648	<37.5	<12.84	
1479.5311	0.21705	<36.2	<12.82	
1480.0175	0.21745	<35.7	<12.82	
1480.6374	0.21796	<34.4	<12.80	
1481.2574	0.21847	<35.6	<12.82	
1482.9472	0.21986	<35.8	<12.82	
1484.4182	0.22107	<38.7	<12.85	
1487.4573	0.22357	<39.6	<12.86	
1488.6122	0.22452	<39.4	<12.86	
1489.4268	0.22519	<39.6	<12.86	
1490.0102	0.22567	<39.3	<12.86	

TABLE 10—*Continued*

λ (Å)	z	$W_{\rm H\,I}$ (mÅ)	log $N_{\rm H\,I}$ (dex)	Note
1493.5965	0.22862	<38.7	<12.85	
1494.5447	0.22940	<38.7	<12.85	
1495.1282	0.22988	<39.1	<12.86	
1499.8450	0.23376	<39.6	<12.86	
1501.5835	0.23519	<39.2	<12.86	
1506.5190	0.23925	<40.1	<12.87	
1507.1147	0.23974	<40.9	<12.88	
1510.3605	0.24241	<39.6	<12.86	
1510.7740	0.24275	<39.4	<12.86	
1517.8612	0.24858	<52.5	<12.99	
1538.0050	0.26515	<43.7	<12.91	
1541.2264	0.26780	<45.6	<12.92	
1543.0499	0.26930	...	...	3
1544.3142	0.27034	<45.1	<12.92	
1544.9585	0.27087	<45.1	<12.92	
1545.5785	0.27138	<42.7	<12.90	
1561.5525	0.28452	<47.0	<12.94	
1568.7249	0.29042	<49.7	<12.96	
1569.4422	0.29101	<49.1	<12.96	
1573.3566	0.29423	<42.5	<12.89	
1580.3102	0.29995	<57.4	<13.02	
1586.4007	0.30496	<57.4	<13.02	
1588.5768	0.30675	<47.5	<12.94	
1589.1116	0.30719	<45.5	<12.92	
1592.3453	0.30985	<48.9	<12.95	
1594.6187	0.31172	<48.9	<12.95	
1595.1779	0.31218	<50.1	<12.96	
1596.1139	0.31295	...	...	4
1596.5880	0.31334	...	...	4
1597.1716	0.31382	...	...	4
1606.0945	0.32116	<48.5	<12.95	
1614.9324	0.32843	<62.0	<13.06	
1615.6011	0.32898	<59.9	<13.04	
1623.9163	0.33582	<44.5	<12.91	
1624.9982	0.33671	<45.7	<12.92	
1625.6182	0.33722	<44.9	<12.92	
1628.5358	0.33962	<46.2	<12.93	
1636.8388	0.34645	<52.5	<12.99	
1639.2459	0.34843	<73.5	<13.13	
1668.3856	0.37240	<61.3	<13.05	
1673.1509	0.37632	<83.0	<13.18	
1678.6093	0.38081	<51.8	<12.99	
1684.1528	0.38537	<49.3	<12.96	
1685.4779	0.38646	<50.4	<12.97	
1696.8565	0.39582	<64.2	<13.07	
1700.7588	0.39903	<62.2	<13.06	
1702.0596	0.40010	<62.0	<13.06	

Notes.—The upper limits are 3 σ and were estimated over a velocity range $[-40, 40]$ km s^{-1}. (1) Misidentification: interstellar C I* λ1329. (2) The spectrum is erratic near this wavelength. (3) Misidentification: O VI λ1031 at $z = 0.4951$. (4) There is undulation in the spectrum, making any identification with a BLA very uncertain.

REFERENCES

Aracil, B., Tripp, T. M., Bowen, D. V., Prochaska, J. X., Chen, H.-W., & Frye, B. L. 2006a, MNRAS, 367, 139
———. 2006b, MNRAS, 372, 959
Bahcall, J. N., Jannuzi, B. T., Schneider, D. P., Hartig, G. F., Bohlin, R., & Junkkarinen, V. 1991, ApJ, 377, L5
Bowen, D. V., Pettini, M., & Blades, J. C. 2002, ApJ, 580, 169
Burles, S., Nollett, K. M., & Turner, M. S. 2001, ApJ, 552, L1
Cen, R., & Fang, T. 2006, ApJ, 650, 573
Cen, R., & Ostriker, J. P. 1999, ApJ, 514, 1
———. 2006, ApJ, 650, 560
Cristiani, S., & D'Odorico, V. 2000, AJ, 120, 1648
Danforth, C. W., & Shull, J. M. 2005, ApJ, 624, 555
Davé, R., Hernquist, L., Katz, N., & Weinberg, D. H. 1999, ApJ, 511, 521
Davé, R., & Tripp, T. M. 2001, ApJ, 553, 528
Davé, R., et al. 2001, ApJ, 552, 473
D'Odorico, V., & Petitjean, P. 2001, A&A, 370, 729
Fang, T., & Bryan, G. L. 2001, ApJ, 561, L31
Fang, T., Mckee, C. F., Canizares, C. R., & Wolfire, M. 2006, ApJ, 644, 174
Fukugita, M., Hogan, C. J., & Peebles, P. J. E. 1998, ApJ, 503, 518
Ganguly, R., Masiero, J., Charlton, J. C., & Sembach, K. R. 2003, ApJ, 598, 922
Haardt, F., & Madau, P. 1996, ApJ, 461, 20
Hu, E. M., Kim, T., Cowie, L. L., Songaila, A., & Rauch, M. 1995, AJ, 110, 1526
Impey, C. D., Petry, C. E., & Flint, K. P. 1999, ApJ, 524, 536
Janknecht, E., Reimers, D., Lopez, S., & Tytler, D. 2006, A&A, 458, 427

Kaastra, J. S., Werner, N., den Herder, J. W. A., Paerels, F. B. S., de Plaa, J., Rasmussen, A. P., & de Vries, C. P. 2006, ApJ, 652, 189
Kim, T.-S., Carswell, R. F., Cristiani, S., D'Odorico, S., & Giallongo, E. 2002a, MNRAS, 335, 555
Kim, T.-S., Cristiani, S., & D'Odorico, S. 2001, A&A, 373, 757
———. 2002b, A&A, 383, 747
Kim, T.-S., Hu, E. M., Cowie, L. L., & Songaila, A. 1997, AJ, 114, 1
Kirkman, D., & Tytler, D. 1997, ApJ, 484, 672
Lehner, N., Savage, B. D., Wakker, B. P., Sembach, K. R., & Tripp, T. M. 2006, ApJS, 164, 1
Lu, L., Sargent, W. L. W., Womble, D. S., & Takada-Hidai, M. 1996, ApJ, 472, 509
Morris, S. L., Weymann, R. J., Savage, B. D., & Gilliland, R. L. 1991, ApJ, 377, L21
Nicastro, F., et al. 2005, Nature, 433, 495
Oegerle, W. R., et al. 2000, ApJ, 538, L23
O'Meara, J. M., Tytler, D., Kirkman, D., Suzuki, N., Prochaska, J. X., Lubin, D., & Wolfe, A. M. 2001, ApJ, 552, 718
Penton, S. V., Shull, J. M., & Stocke, J. T. 2000, ApJ, 544, 150
Penton, S. V., Stocke, J. T., & Shull, J. M. 2004, ApJS, 152, 29
Petitjean, P., Webb, J. K., Rauch, M., Carswell, R. F., & Lanzetta, K. 1993, MNRAS, 262, 499
Prochaska, J. X., Chen, H.-W., Howk, J. C., Weiner, B. J., & Mulchaey, J. 2004, ApJ, 617, 718
Rasmussen, A. P., Kahn, S. M., Paerels, F., Willem den Herder, J., Kaastra, J., & de Vries, C. 2007, ApJ, 656, 129
Rauch, M., et al. 1997, ApJ, 489, 7
Richter, P., Fang, T., & Bryan, G. L. 2006a, A&A, 451, 767
Richter, P., Savage, B. D., Sembach, K. R., & Tripp, T. M. 2006b, A&A, 445, 827
Richter, P., Savage, B. D., Tripp, T. M., & Sembach, K. R. 2004, ApJS, 153, 165
Savage, B. D., Lehner, N., Wakker, B. P., Sembach, K. R., & Tripp, T. M. 2005, ApJ, 626, 776
Savage, B. D., Sembach, K. R., Tripp, T. M., & Richter, P. 2002, ApJ, 564, 631
Schaye, J. 2001, ApJ, 559, 507
Schaye, J., Theuns, T., Leonard, A., & Efstathiou, G. 1999, MNRAS, 310, 57
Sembach, K. R., Tripp, T. M., Savage, B. D., & Richter, P. 2004, ApJS, 155, 351
Shull, J.-M., et al. 2000, ApJ, 538, L13
Spergel, D. N., et al. 2003, ApJS, 148, 175
Sutherland, R. S., & Dopita, M. A. 1993, ApJS, 88, 253
Theuns, T., Leonard, A., & Efstathiou, G. 1998, MNRAS, 297, L49
Tripp, T. M., Bowen, D. V., Sembach, K. R., Jenkins, E. B., Savage, B. D., & Richter, P. 2006, in ASP Conf. Ser. 348, Astrophysics in the Far Ultraviolet, ed. G. Sonneborn, H. Moos, & B.-G. Andersson (San Francisco: ASP), 341
Tripp, T. M., Giroux, M. L., Stocke, J. T., Tumlinson, J., & Oegerle, W. R. 2001, ApJ, 563, 724
Tripp, T. M., Savage, B. D., & Jenkins, E. B. 2000, ApJ, 534, L1
Tytler, D. 1987, ApJ, 321, 49
Weinberg, D. H., Miralda-Escude, J., Hernquist, L., & Katz, N. 1997, ApJ, 490, 564
Weymann, R. J., et al. 1998, ApJ, 506, 1
Williger, G. M., Heap, S. R., Weymann, R. J., Davé, R., Ellingson, E., Carswell, R. F., Tripp, T. M., & Jenkins, E. B. 2006, ApJ, 636, 631
Yuan, Q., Green, R. F., Brotherton, M., Tripp, T. M., Kaiser, M. E., & Kriss, G. A. 2002, ApJ, 575, 687